Adsorption geometry of π-conjugated organic molecules on metal surfaces studied with the X-ray standing wave technique

Dissertation
der Mathematisch-Naturwissenschaftlichen Fakultät
der Eberhard Karls Universität Tübingen
zur Erlangung des Grades eines
Doktors der Naturwissenschaften
(Dr. rer. nat.)

vorgelegt von
Christoph Bürker
aus Filderstadt

Tübingen
2014

Tag der mündlichen Qualifikation:	04.07.2014
Dekan:	Prof. Dr. Wolfgang Rosenstiel
1. Berichterstatter	Prof. Dr. Frank Schreiber
2. Berichterstatter	Prof. Dr. Reinhold Fink

Contents

Chapter 1

Introduction and Motivation

The promising properties of organic semiconductors employed in applications such as organic light emitting diodes (OLEDs) [1–3], organic field effect transistors (OFET) [3, 4], organic photovoltaic cells (OPV) [5, 6], and organic memory cells (OMC) [7] have opened a new field in thin-film and surface science. Compared to their inorganic counterparts, devices made of π-conjugated organic compounds are potentially cheap in production, and fabrication can be done on mechanically flexible materials. There are already some applications available [8]; however, engineers and scientists still face challenges to improve the device performance and fight degradation under ambient conditions [9], for instance due to oxygen or ultra violet light.

To obtain a functional electric device, the organic active layer needs an electrode, which is often made of metals like copper, silver, or gold. In such a case, the interface between the metal and the conjugated organic molecule (COM) is created. Here, a scientific field has attracted interest in the 1990s to study the interaction of the first layer of organic molecules with the metal surface and the consequences of the interface properties for the device performance. Various surface analysis techniques are applied to study COMs on different surfaces, such as X-ray photoelectron spectroscopy (XPS), ultra violet (UV) photoelectron spectroscopy (UPS), X-ray standing wave technique (XSW), scanning tunneling microscopy (STM), low-energy electron diffraction (LEED), near edge X-ray absorption fine structure spectroscopy (NEXAFS), atomic force microscopy (AFM), and temperature desorption spectroscopy (TDS). Each technique is specialized to extract one or more properties of the COM–metal interface.

This work focuses on the XSW method, which, until today, is the most precise technique to study bonding distances. In the following, the term *bonding distance* refers to the average distance between the molecule and the topmost atomic layer of the metal substrate measured along the surface normal, as depicted in Figure 1.1(b). The technical requirements for XSW experiments are challenging. Photon energies must be very finely tunable and must have a resolution of $\frac{\Delta E}{E} \leq 10^{-4}$, in typical cases. Therefore, XSW experiments are carried out at selected synchrotron facilities.

Typically, the error of the bonding distance determined with the XSW technique is only ± 0.05 Å or even less. In addition to its high precision, the XSW technique makes use of the XPS technique, which is an element-specific tool. Both techniques will be described

in detail in Chapter 2. As a consequence, the bonding distance of each chemical species can be determined separately. Here, the term *chemical species* does not only refer to different elements, but to different chemical environments in general. For instance, if a molecule contains carbon and fluorine atoms, the carbon core-level signal C 1*s* can be resolved in a peak emerging from a C–C bond and one from the C–F bond [10]. The element specificity has been exploited to detect molecular distortions, which are induced upon adsorption on metal surfaces [11–13]. It turned out that, by combination of these findings with other experimental techniques, the geometry of COMs, which are adsorbed on metal surfaces, impacts electronic properties of the molecules, e.g. the charge injection into the metal [14, 15]. The charge injection, however, affects the performance of organic devices. Hence, the geometry of the adsorbed molecule is of great importance for the design of optimized organic electronics.

Interaction between molecule and metal

When a COM approaches a surface it is attracted by the long-range van der Waals (vdW) forces. Figure 1.1(a) displays the potential slope of London dispersion forces [1] as a function of the distance between a COM and a surface (solid line). At very low distances

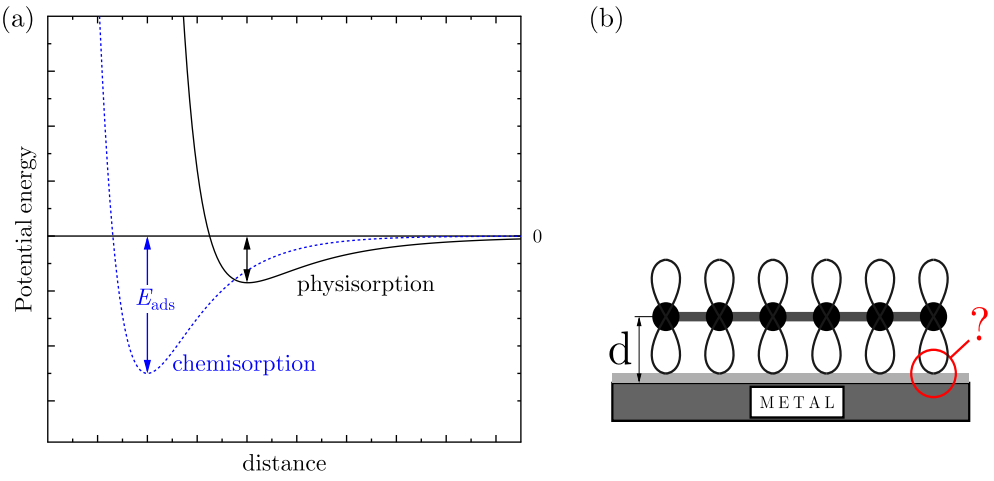

Figure 1.1: (a) Schematic slopes of interaction potentials for a molecule interacting with a surface. The solid line shows a Lennard-Jones potential [16], which represents the interaction by vdW forces (physisorption). The dotted line displays a slope of the Morse potential that is often used to describe a covalent bond (chemisorption) [17]. (b) Schematic and simplified picture of a molecule (with π-orbitals) adsorbed on a surface. The interaction strength between molecular and metal orbitals impacts the properties of the COM. One way to assess the interaction strength is the bonding distance.

Pauli-repulsion between molecular and substrate density of states (DOS) is responsible for the steep potential increase. If vdW forces are the only interaction mechanisms, the

[1] In this work vdW is interchangeably used with London dispersion forces.

COM will reach the minimum of the potential at a distance, where the vdW interaction equals the Pauli-repulsion. This is the limit of weak interaction and called *physisorption*. The distance of two atoms, where interaction is due solely to London dispersion forces, is equal to the sum of the vdW radii of the atoms [18]. This definition of the vdW radius is often used to correlate the bonding distance with interaction strength [19]. To do so, one considers the vdW radius of an atom within the molecule, often carbon, and the vdW radius of a substrate atom. In the case that the bonding distance is smaller than the sum of the vdW radii, the interaction is assumed to consist of vdW plus additional forces. For instance, hybridization of molecular and surface DOS can occur, creating a covalent bond between atoms of the molecule and the surface. The case of covalent interaction is called *chemisorption*. In that case, the distance between two atoms is close to the sum of their covalent radii. Figure 1.1(a) also shows the schematic slope of a potential with chemisorptive character as a dotted line. These are just the two limiting cases. In most cases, the observed interaction strength lies in between. A relation between interaction strength (physisorption vs. chemisorption) and bonding distance was found for the COM 3,4,9,10-perylene-tetracarboxylic-dianhydride (PTCDA) on the coinage metal surfaces Cu(111), Ag(111), and Au(111) [15]. This example is visualized in Figure 1.4.

Comparing the bonding distance and the vdW radii renders the possibility to qualitatively describe the interaction strength between molecule and metal. The next section describes other interface effects, which are related to the bonding distance.

Energy level alignment at the metal–organic interface

Fundamentally, if two different materials come into contact, their energy levels align. This also occurs for COM in contact with metals. Importantly, the energy level alignment (ELA) strongly impacts the device performance, as it determines the charge injection (electrons, holes) into the organic material.

Due to this key factor great efforts were put into researching the ELA. It turned out that the ELA is not determined simply by the work function of the metal and properties of the COM like the electron affinity (EA) and the ionization energy (IE), as one might initially think. Instead, a realistic picture of the ELA and its complexity is won only after several effects are considered, which will be described in the following.

At a clean metal surface orbitals spill out into the vacuum, leading to a surface dipole. A schematic of this phenomenon is provided in Figure 1.2(a), where negative charge resides outside the metal at the vicinity of the surface and positive charge within. As a molecule approaches toward the metal surface due to long-range attractive vdW dispersion forces, the molecular orbitals start to “feel” the metal orbitals, which spill out into the vacuum. Upon adsorption of the molecule, the electron density is “pushed back” into the metal, thereby reducing the surface dipole of the metal. If the clean metal surface is referenced to zero interface dipole (ID), the adsorption of molecules creates an ID, which changes the effective work function for the molecule-metal system. This effect is also called the *push-back effect* [20]. Its influence on the ELA is depicted in Figure 1.3(b).

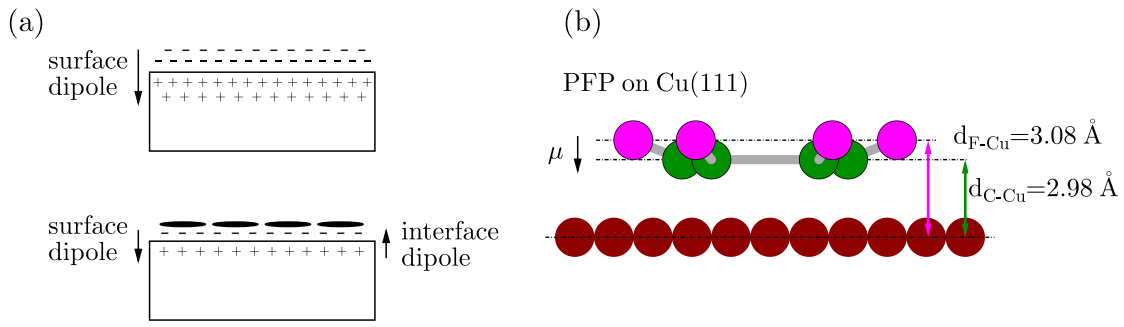

Figure 1.2: (a) Principle of the push-back effect. Upon adsorption of molecules the surface dipole is reduced compared to a clean metal substrate, while an interface dipole (ID) is created. (b) Side view of PFP adsorbed on Cu(111). Different adsorption distances of fluorine (pink) and carbon (green) atoms lead to a distorted molecule. Due to the different partial charge of the atoms, an additional dipole μ is created. Picture in panel (b) adapted from Ref. [14].

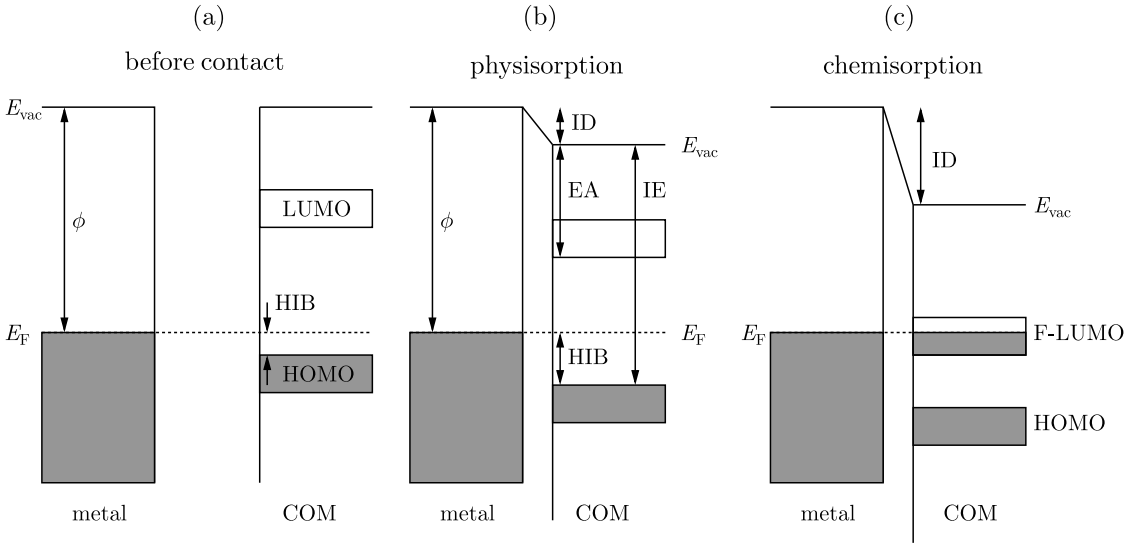

Figure 1.3: Energy level alignment at the COM–metal interface. (a) DOS of a metal and molecule before contact, showing the highest occupied molecular orbital (HOMO), lowest unoccupied molecular orbital (LUMO), and the hole injection barrier (HIB). (b) For physisorbed molecules, the push-back effect creates an interface dipole (ID), which lowers the vacuum level E_{vac} and thereby the effective work function. The HIB is increased. Different electronic quantities are introduced, which can be influenced possibly by the ELA, namely ionization energy (IE) and electron affinity (EA). (c) Hybridization of molecular and metal orbitals can change the electronic structure of the molecule significantly. For the displayed example, a charge transfer from the metal to the molecule fills partially the former (F-) LUMO, and the molecule thus becomes conducting.

If COMs are composed of different atoms and a polar bond between two atoms is present, another important effect can occur, which influences the ELA. Depending on the interaction between COM and metal, the molecule can adsorb on the surface with a distorted geometry, which results in a vertical dipole along the molecule, modifying the vacuum level. Figure 1.2(b) displays this scenario for perfluoropentacene (PFP) on Cu(111) [14]. In any case, an interface dipole due to the adsorption of organic molecules impacts the charge transport between COM and metal.

These adsorption-induced molecular distortions as a consequence of strong interaction can often be related to hybridization of molecular and metal orbitals. For the COM PTCDA adsorbed on Cu(111) and Ag(111), the formation of a charge transfer complex (CTC) involves a distorted molecule [15]. If these newly occupied electronic states are at the Fermi edge, as is the case for PTCDA on Ag(111) (see Figure 1.4), the molecule becomes conducting. Figure 1.4 displays the relationship between the formation of a CTC and the bonding distance for PTCDA on Cu(111), Ag(111), and Au(111).

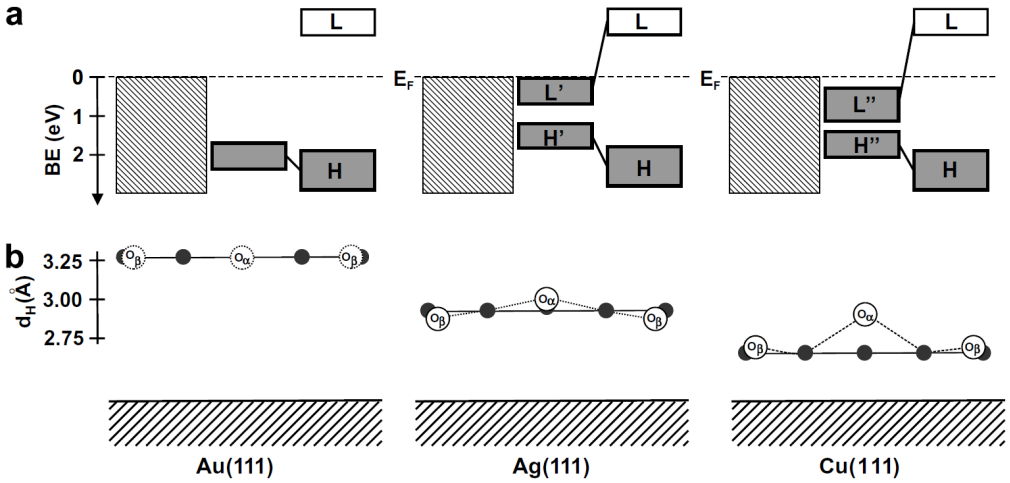

Figure 1.4: Correlation between interaction strength and bonding distance for the example PTCDA on Cu(111), Ag(111), and Au(111). (a) Schematic energy level diagrams. In each panel the dashed areas represent the metal electron density, L and H denote the LUMO and HOMO, respectively, for the isolated molecule. The primed letters stand for the aligned orbitals of PTCDA adsorbed on the metal surface. (b) Schematic side view of adsorbed PTCDA. The black circles correspond to carbon atoms, O_α and O_β denote the two types of oxygen (anhydride and carboxylic, respectively). The position of the energy levels can be correlated to the adsorption geometry of PTCDA. Reprinted from Ref. [15]. Copyright (2008), with permission from Elsevier.

The above mentioned phenomena that affect the ELA, can, in principle, arise at the same time. The precise knowledge of the molecular conformation is, therefore, a key factor to disentangle these overlapping effects and a fundamental requirement to understand thoroughly the COM–metal interface.

Computational modeling of the metal–organic interface

In addition to the gain of information due to XSW measurements, the bonding distances, determined using the XSW technique, have become a valuable source of information for computational studies of the COM–metal interface. In judging whether calculations yield realistic results, precisely measured bonding distances are used as benchmarks. This is because the calculated bonding distance is very sensitive on the theoretical approach. A congruence of theory and experiment with respect to the bonding distance is a sign of a suitable computational model. Furthermore, corresponding calculations can unveil other properties of the COM–metal interface, such as the DOS and adsorption energy.

Theoretical methods aim at modelling the COM–metal interface as exactly as possible, while, at the same time, the computational cost should remain reasonable. In the following we will sketch the density functional theory (DFT) by Kohn-Sham [21]. This method, when describing a molecule on a metal surface, is more popular than Hartree-Fock approaches based on wave function calculations because it is computationally more efficient.

DFT is based on the theorem that the electron density determines the ground state. This theorem was proved by Hohenburg and Kohn in 1964 [22]. It means that instead of describing a system with N particles by $3N$ coordinates it is sufficient to know the density $\rho(\boldsymbol{r})$, which only depends on 3 coordinates. Although DFT is, in principle, exact, one must, in practice, approximate the exchange correlation (XC) functionals that are required in DFT. Many different functionals have been developed with varying shortcomings and advantages. An overview of various XC functionals is given in Ref. [23]. Most of them do not account for the dispersion interaction, despite the importance of these long-range interactions for the formation and function of COMs. Therefore, to obtain reliable results, vdW interactions have to be included in the calculations. Different proposals came up to address this issue in DFT [24–26]. The established functionals were further improved. One method extended the approach from Grimme [26] rather recently. It obtains accurate dispersion coefficients (C_6 coefficients, which describe the vdW interaction between two atoms or molecules) directly from the electron density of the ground state (DFT+vdW method) [27]. The advantage of this method is that it can be coupled easily to XC functionals. The use of this approach with the Perdew-Burke-Ernzerhof (PBE) XC functional, a non-empirical functional, led to promising results for the prototypical compound PTCDA adsorbed on Cu(111), Ag(111), and Au(111) [28].

Outline

This thesis is organized as follows: Chapter 2 provides a description of the experimental methods used in this work. The investigated materials are specified in Chapter 3. There, the chemical structure of the molecular compounds is displayed as well as the properties of the used substrates. Furthermore, a description of the sample preparation is given. Chapter 4 specifies the three experimental setups, on which the XSW experiments took place. In addition, the principle of data acquisition and analysis is explained in that chapter. The

XSW results are presented and discussed in Chapter 5. The studied samples were selected to gain insight into how the molecular geometry and interaction strength depends on different variables like the substrate, the coverage, the temperature and chemical variations of the molecule. The end of Chapter 5 supplies an overview of XSW results of COMs on Cu(111), Ag(111), and Au(111) that are found in literature or presented in this work. The final Chapter 6 summarizes this work and gives an outlook for future work.

In addition to the XSW experiments, the author of this thesis assembled an in-house surface science ultra-high vacuum (UHV) chamber for XPS and TDS experiments. Its design and features are described in the Appendix A.1 along with first results of measurements performed in this setup.

Chapter 2

Experimental Methods

The aim of this chapter is to introduce and explain the different analysis techniques, which have been used for this work. First, the XPS technique will be explained. Then, the XSW technique will be illustrated, which, in the way we apply it, makes use of XPS.

2.1 Photoelectron spectroscopy

2.1.1 Introduction

Photoelectron spectroscopy (PES) is a widely used technique in surface science for decades. Siegbahn laid the foundation by building the first instrument for the so-called electron spectroscopy for chemical analysis (ESCA) [10]. The principle of PES is based on the photoelectric effect [29, 30], which explains the emission of electrons from solids due to light irradiation. The basic equation for the kinetic energy E_{kin} of the released electrons due to the interaction of a photon with energy $\hbar\omega$ and a sample with work function ϕ_{s} is

$$E_{\mathrm{kin}} = \hbar\omega - E_{\mathrm{B}} - \phi_{\mathrm{s}}. \tag{2.1}$$

E_{B} is the binding energy of the initial state of the electron, defined relative to the Fermi level E_{F}. Depending on the energy of the photons, PES is divided into UPS ($\hbar\omega < 100$ eV) and XPS ($\hbar\omega > 100$ eV). It is the small mean free path λ of the photoelectrons (a few Å for UPS and a few tens of Å in the case of XPS), which makes PES a suitable tool for surface and interface studies. The information depth of PES is small enough to detect effects in monolayer and multilayer regime of adsorbates.

2.1.2 Theoretical description of the photoemission process

A very detailed description of the photoemission process can be found in Ref. [31]. Unless otherwise noted, the equations in this section are taken from this reference. In the following, only an overview of the topic shall be given.

The common theoretical description of the interaction of light with atoms resulting in a photoemission process is done using first-order perturbation theory. This approach

comprises the photon induced excitation of an N-electron system in the initial (ground) state with wavefunction $|\psi_\mathrm{i}\rangle$ into the final state $|\psi_\mathrm{f}\rangle$, which describes the ejected electron and the remaining $(N-1)$-electron system. The probability w, also called differential cross section, of such a transition is according to Fermi's Golden Rule:

$$w \propto \left|\left\langle \psi_\mathrm{f} \middle| \hat{H}' \middle| \psi_\mathrm{i} \right\rangle\right|^2 \delta(E_\mathrm{f} - E_\mathrm{i} - \hbar\omega), \tag{2.2}$$

with ν the frequency of the light, E_i (E_f) is the energy of the initial (final) state. The perturbation Hamiltonian $\hat{H}'$ describes the interaction of an electron (neglecting its spin) with the vector potential of an electromagnetic wave field $\boldsymbol{A}$, and the momentum operator $\hat{p} = -\mathrm{i}\hbar\boldsymbol{\nabla}$:

$$\hat{H}' = \frac{e}{2m_\mathrm{e}c}(\boldsymbol{A}\cdot\hat{p} + \hat{p}\cdot\boldsymbol{A}) + \frac{e^2}{2m_\mathrm{e}c^2}A^2. \tag{2.3}$$

In order to solve the transition matrix element from Equation 2.2, a few assumption are made, which are mentioned now:

- Typically, the intensity of the electromagnetic wave field is not extremely high, and the last term in Equation 2.3 can be ignored.
- Assuming that the electromagnetic wave travels in a uniform medium (and therefore neglecting particular surface effects, which were found in UPS studies of solids [32]), the term $\hat{p}\cdot\boldsymbol{A}$ can be neglected [33].

These two assumptions simplify the Hamiltonian to the following form:

$$\hat{H}' = \frac{e}{2m_\mathrm{e}c}\boldsymbol{A}\cdot\hat{p}. \tag{2.4}$$

Further assumptions are:

- Koopman's theorem ignores any influence of the ionization process on the wavefunction of the remaining system. In other words, as soon as the ionization takes place, the photoelectron has no Coulomb interaction with the hole left behind or with other electrons (also called "sudden approximation"). As a result of Koopman's theorem, the measured kinetic energy of the photoelectron enables the determination of its binding energy.
- The Born–Oppenheimer approximation [34] allows to separate the total wavefunction of the initial/final state into a product of an electronic part and a nuclear part. For the description of the photoemission process it is sufficient to consider only the electronic part, as the motion of the nucleus due to geometrical relaxation happens at larger time scales than the photoemission process [35]. This is particularly important for the XSW experiments, which determines the position of the center of atoms (i.e. de facto the position of their nucleus) by making use of the photoemission process, see Section 2.2.

Now we are in a position to solve the transition matrix element from Equation 2.2. However, there are effects, which can be traced back to a violation of Koopman's theorem and shall be mentioned here:

- The screening of the photo-hole by the surrounding depends on the polarizability of the material. Highly polarizable matter such as metals screen the photo-hole effectively, also photo-holes of thin – in the range of monolayer (ML) – adsorbates on metal substrates, and Koopman's theorem is valid. For thick molecular coverages in the range of several molecular layers, only incomplete screening occurs. As a result, the escaping photoelectron is still attracted by the corresponding hole and will be detected with a lower kinetic energy (a few 10^{-1} eV).
- The escaping electron can excite other electrons in two different ways, as shown in Figure 2.1: In a *shake-up* process the excitation of an additional electron from the valence band to an unbound state takes place. The required, discrete energy for this transition is subtracted from the kinetic energy of the photoelectron. In molecules, the lowest excitation of that kind is a HOMO–LUMO transition, in the order of a few eV. A *shake-off* process is a transition into an unbound continuum state.

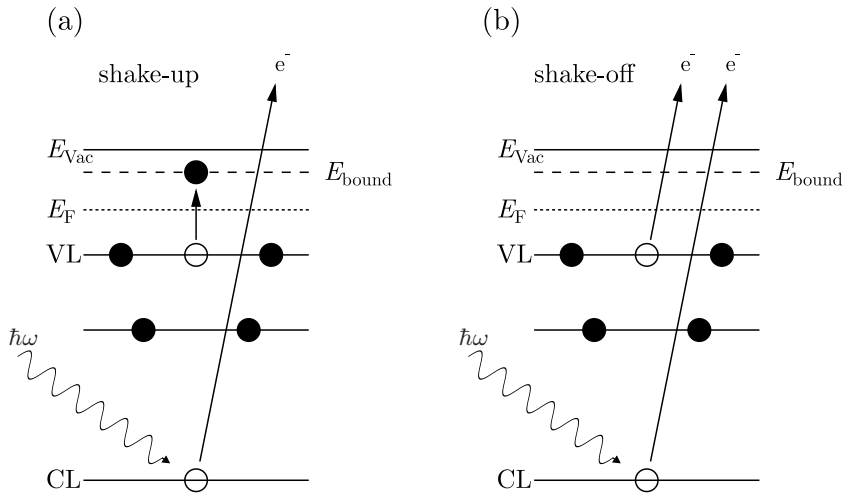

Figure 2.1: Two-electron processes, which can occur in a photoexcitation from a core-level (CL): (a) shake-up and (b) shake-off. For details see main text.

2.1.3 XPS analysis

The aim of this section is to explain common features of a typical PE spectrum and what to learn from these. Figure 2.2 shows a schematic PE spectrum with the photoelectron intensity as a function of the kinetic energy of the photoelectrons. The PES technique reveals the density of states (DOS) of the sample. As mentioned before, it is commonly divided in XPS and UPS, depending on the energy of the exciting photons. The narrow

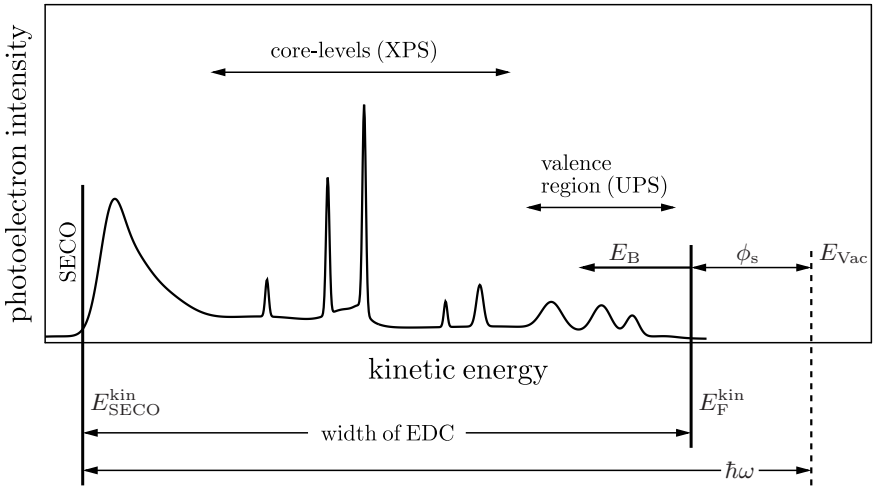

Figure 2.2: Schematic picture of PE spectrum of an organic semiconductor. It depicts the photoelectron intensity as a function of the kinetic energy. The spectrum can be divided in three sections: The SECO region at low kinetic energy, the core-level region, which can be accessed with XPS and the valence band region, measured with UPS. The binding energy is measured from the Fermi edge ($E^{F}_{B} = 0$).

peaks in the spectrum emerge from core-levels such as $1s$, $2s$, $2p_{1/2}$, $2p_{3/2}$, etc. Their binding energy is typically > 50 eV and hence accessible with XPS. The valence region contains the outermost orbitals and, in the case of organic semiconductors, the highest occupied molecular orbital (HOMO). This region is studied with UPS. The broad feature at low kinetic energies are secondary electrons, which originally were released from core-levels or the valence region and lost most of their kinetic energy and their information about the initial state in one or more inelastic scattering processes. The left onset of that peak is called secondary electron cut-off (SECO). At kinetic energies below the SECO, the photoelectrons have insufficient kinetic energy to overcome the sample work function. The overall spectrum between the SECO and the Fermi edge is called the energy distribution curve (EDC). It can be used to determine the sample work function via

$$\phi_s = \hbar\omega - (E^{kin}_F - E^{kin}_{SECO}). \tag{2.5}$$

In PES experiments one has to consider also the work function of the analyzer ϕ_A. The energy levels of the system sample–vacuum–analyzer are shown schematically in Figure 2.3. After leaving the sample, the electron has the kinetic energy E_{kin}. In order to reach the analyzer it has to overcome an additional barrier due to the analyzer work function ϕ_A if, as it is the case in this picture, ϕ_A is larger than ϕ_s. Therefore, only electrons will be detected, whose kinetic energies after leaving the sample are $E_{kin} > \phi_A - \phi_s$. This is not the case for electrons with energies close to the SECO. To measure the SECO, a negative voltage of a few volts is applied to the sample, which shifts the whole EDC rigidly toward higher kinetic energy, and the electrons close to the SECO are detected by the analyzer.

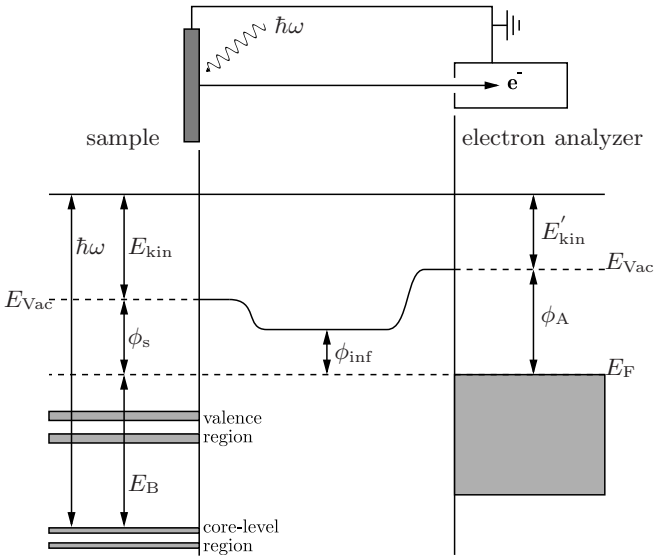

Figure 2.3: Working principle of PES experiments. A (monochromatic) photon source with energy $\hbar\omega$ illuminating the sample produces photoelectrons from orbitals with a binding energy E_{B}, which are detected and analyzed regarding their kinetic energy in the electron analyzer. E_{kin} is the kinetic energy of the electron after leaving the sample, E'_{kin} the kinetic energy seen by the analyzer. The connection between sample and analyzer aligns their Fermi levels E_{F}. As a consequence of the Fermi level alignment, the vacuum energy E_{Vac} changes while moving from the sample to the analyzer (between sample and analyzer the work function is ϕ_{inf} as the electrons are "infinitely" far away from any solid).

The kinetic energy of the photoelectrons measured by the analyzer is given in analogy to Equation 2.1 by

$$E'_{\mathrm{kin}} = h\nu - E_{\mathrm{B}} - \phi_{\mathrm{A}}. \tag{2.6}$$

This equation can be used to determine the binding energy E_{B} by measuring the kinetic energy E'_{kin}, since the sample work function remains constant for a given analyzer.

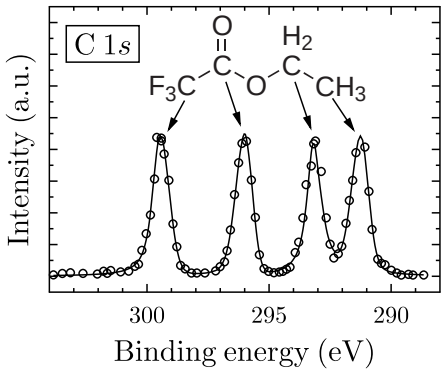

Figure 2.4: Chemical shift of the C 1*s* core-level of ethyl-trifluoroacetate. The arrows connect the carbon atoms in different chemical environments with the corresponding peaks in the XP spectrum. The graph is adapted from [10].

The power of the XPS technique is nicely pointed out in Figure 2.4. There, a C 1*s* spectrum is shown for the molecule ethyl-trifluoroacetate. The four carbon atoms of the molecule have different chemical environments due to bonds to different atoms. Depending on the bonded atom, their electronegativity, and the type of the bond, the electrons involved in the bonds are either drawn from or attracted to the carbon atom, resulting in positive or negative partial charge of the carbon atom. This property is reflected in the XP spectrum, where the particular partial charge leads to specific binding energies of the C 1*s* peaks. This is referred to as the "chemical shift".

2.2 The X-ray standing wave technique

The XSW technique can be used to measure element specific bonding distances of organic molecules on single crystal substrates with very high precision (typically ±0.05 Å). It is based on a combination of the theory of dynamical diffraction (TDD) and X-ray photoelectron spectroscopy (XPS). The description of the TDD in this paragraph follows Ref. [36] and [37]. The XSW technique will be explained on the basis of Refs. [38–41]. We will restrict to the circumstances, which were existent at the experimental setups of the XSW experiments (for details of the experimental setups see Chapter 4):

- The angle of incidence of the X-rays is close to 90° relative to the surface plane. These so called normal incidence XSW (NIXSW) experiments have the advantage that a certain imperfection of the substrate crystallinity can be tolerated [38].

- σ-polarized X-rays: Vectors of the Electric field ($\boldsymbol{E}$) of the incident and Bragg-reflected beams are collinear and perpendicular to the vector associated with the Bragg reflection $\boldsymbol{H}$.
- The use of centrosymmetric crystals. In that case, one can write for the structure factor the following relation: $F_{\bar{H}} = F_H^*$).

2.2.1 Theory of dynamical diffraction

The TDD describes the propagation of X-rays in crystals. In contrast to the kinematic theory of diffraction, TDD takes, among other things, extinction and interference effects into account.

Starting with Maxwell's equations,

$$\begin{aligned} \boldsymbol{\nabla} \times \boldsymbol{\mathcal{E}} &= -\mu_0 \frac{\partial \boldsymbol{\mathcal{H}}}{\partial t} \\ \boldsymbol{\nabla} \times \boldsymbol{\mathcal{H}} &= -\epsilon_0 \frac{\partial (\epsilon_\mathrm{r} \boldsymbol{\mathcal{E}})}{\partial t} \end{aligned} \tag{2.7}$$

with $\boldsymbol{\mathcal{E}}$ and $\boldsymbol{\mathcal{H}}$ being the electric and magnetic field, respectively, ϵ_0 and μ_0 the electric and magnetic constant. These Maxwell equations hold for a medium with

- no conductivity at X-ray frequencies, $\sigma_\mathrm{c} = 0$,
- a magnetic behaviour of the vacuum, $\mu_\mathrm{r} = 1$, and
- a periodic dielectric constant $\epsilon_\mathrm{r}(\boldsymbol{r}) = 1 - \Gamma \sum_{\boldsymbol{H}} F_H \mathrm{e}^{-2\pi\mathrm{i}\boldsymbol{H}\cdot\boldsymbol{r}}$.

Here, Γ is defined as $\Gamma = \frac{r_\mathrm{e}\lambda^2}{\pi V}$, with the classical radius of the electron r_e, the volume of the unit cell V and the wavelength of the X-rays λ. F_H, the complex structure factor of the reciprocal lattice vector $\boldsymbol{H}$, is the Fourier transform of the electron density $\rho(\boldsymbol{r})$,

$$F_H = \int_V \rho(\boldsymbol{r}) \mathrm{e}^{2\pi\mathrm{i}\boldsymbol{H}\cdot\boldsymbol{r}}, \tag{2.8}$$

and contains all properties connected to the scattering and absorption of the medium. In order to solve the Maxwell equations in the crystal, one assumes that $\boldsymbol{\mathcal{E}}$ and $\boldsymbol{\mathcal{H}}$ can be expressed as sums of plane waves with wave vector $\boldsymbol{k}$, which fulfil the Bragg condition, $\boldsymbol{k}_H = \boldsymbol{k}_0 + \boldsymbol{H}$ (in the following $\boldsymbol{\mathcal{A}}$ stands for $\boldsymbol{\mathcal{E}}$ and $\boldsymbol{\mathcal{H}}$),

$$\mathcal{A} = \mathrm{e}^{2\pi\mathrm{i}\nu t} \sum_{\boldsymbol{H}} \mathcal{A}_H \mathrm{e}^{-2\pi\mathrm{i}\boldsymbol{k}_H\cdot\boldsymbol{r}} = \left[\sum_{\boldsymbol{H}} \mathcal{A}_H \mathrm{e}^{-2\pi\mathrm{i}\boldsymbol{H}\cdot\boldsymbol{r}} \right] \mathrm{e}^{-2\pi\mathrm{i}\boldsymbol{k}_0\cdot\boldsymbol{r}} \mathrm{e}^{2\pi\mathrm{i}\nu t}, \tag{2.9}$$

in analogy to Bloch waves, which describe in solid state physics the properties of the electrons in a periodic potential. Now we restrict to only one reciprocal lattice point $\boldsymbol{H}$ dominating the diffraction. In this case only two equations remain:

$$\begin{aligned} \left[k^2(1-\Gamma F_0) - (\boldsymbol{k}_0 \cdot \boldsymbol{k}_0)\right] E_0 - k^2 \Gamma F_{\bar{H}} E_H &= 0 \\ -k^2 \Gamma F_H E_H + \left[k^2(1-\Gamma F_0) - (\boldsymbol{k}_H \cdot \boldsymbol{k}_H)\right] E_H &= 0 \end{aligned} \tag{2.10}$$

Note that in the following only σ-polarized X-rays are considered and centrosymmetric crystals. k denotes the vacuum value of the wave vector. Regarding the incident and one Bragg-reflected wave, a pair of linear, homogeneous equations remain. For a non-trivial solution, their determinant must be zero:

$$\begin{vmatrix} k^2(1-\Gamma F_0) - \boldsymbol{k}_0 \cdot \boldsymbol{k}_0 & -k^2 \Gamma F_{\bar{H}} \\ -k^2 \Gamma F_H k^2 (1-\Gamma F_0) & -\boldsymbol{k}_H \cdot \boldsymbol{k}_H \end{vmatrix} = 0 \tag{2.11}$$

The result for $\boldsymbol{k}_0$ and $\boldsymbol{k}_H$ leads to the following expressions for the electric field of X-ray plane waves, which are involved in the diffraction process:

$$\mathcal{E}_0 = E_0 \exp\left[2\pi \mathrm{i}\left(\omega t - \boldsymbol{k}_0 \cdot \boldsymbol{r}\right)\right] \tag{2.12}$$

$$\mathcal{E}_H = E_H \exp\left[2\pi \mathrm{i}\left(\omega t - \boldsymbol{k}_H \cdot \boldsymbol{r}\right)\right] \tag{2.13}$$

The diffracted complex field amplitude E_H is related to the incoming one E_0 – due to the assumption of $\mathcal{E}_0$ and $\mathcal{E}_H$ being coherent – by $E_H = \sqrt{R} E_0 = \exp(\mathrm{i}\nu)$, with the phase ν between the two amplitudes, and the reflectivity R

$$\sqrt{R} = \frac{E_H}{E_0} = -\sqrt{\frac{F_H}{F_0}}\left(\eta \pm \sqrt{\eta^2 - 1}\right), \tag{2.14}$$

a function depending of the normalized angle parameter η:

$$\eta = \frac{2^{(E_{\mathrm{Bragg}} - E)}/_{E_{\mathrm{Bragg}}} \sin^2(\Theta_{\mathrm{Bragg}}) - \Gamma F_0}{\Gamma \left|F_H\right|}. \tag{2.15}$$

Equation 2.14 describes the intensity of the reflected beam as a function of the generalized angle parameter η, which is linear in the beam energy. Therefore, by varying either the angle Θ or the energy $E = hc/\lambda$ via the Bragg condition $\lambda = 2d_0 \sin(\Theta_{\mathrm{Bragg}})$ (d_0: spacing of diffraction planes) the so called rocking or Darwin curve is obtained. Figure 2.5 shows the reflectivity (dashed line) as a function of the photon energy (around E_{Bragg}).

2.2.2 The X-ray standing wave field

The overlapping incoming and Bragg-reflected waves form a standing wave, with a normalized intensity at position $\boldsymbol{r}$ being:

$$\begin{aligned} I_{\mathrm{XSW}}(\nu, \boldsymbol{r}) &= \frac{\left|E_0 + E_H\right|^2}{\left|E_0\right|^2} \\ &= 1 + R + 2\sqrt{R}\cos(\nu - 2\pi \boldsymbol{H} \cdot \boldsymbol{r}). \end{aligned}$$

The nodal planes of the standing wave are parallel to the atomic planes, which are responsible for the diffraction. For a fixed ν, the intensity I_{XSW} is spatially modulated. Depending on the value of ν, a scatterer at a certain position $\boldsymbol{r}$ experiences a high or low field intensity. We have seen in Figure 2.5 that ν shifts by π during a Bragg scan. As a result, the XSW

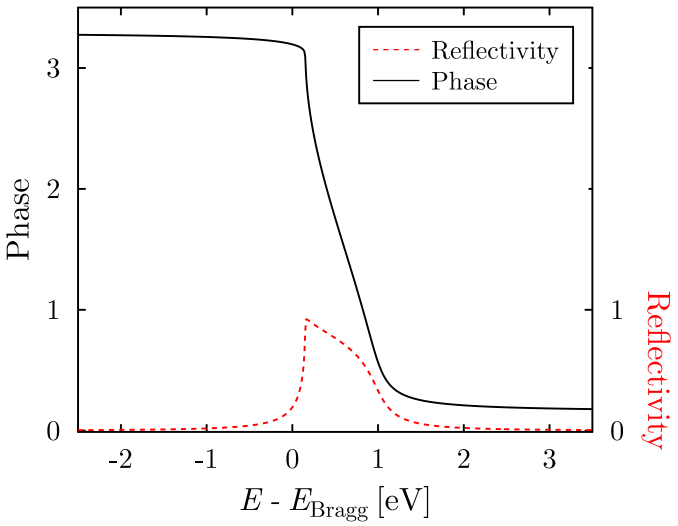

Figure 2.5: Reflectivity or Darwin curve (dashed line) and the phase between the incident and Bragg-reflected X-ray beam (solid line), calculated for the ideal (111) reflection of a copper single crystal.

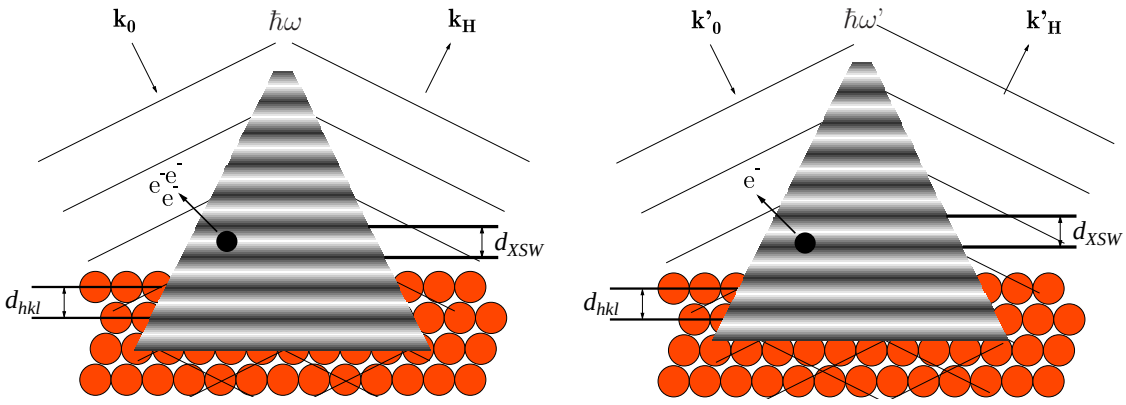

Figure 2.6: The incoming and Bragg-reflected wave, denoted here with $\boldsymbol{k_0}$ and $\boldsymbol{k_H}$, respectively, form the XSW field with the nodes (black) and the antinodes (white) being parallel to the diffraction plane *hkl*. In the right image the photon energy has changed. According to Figure 2.5, the phase between the incident and reflected wave has changed, and the XSW field has moved upwards. The adsorbate in the left picture is at the place of an antinode of the XSW field. Thus, more photoelectrons are released than in the right picture, in which the adsorbate is close to the node.

field moves during a Bragg scan in the direction of $\boldsymbol{H}$ by half a lattice spacing, $d_0/2$. This means that, for a given value of $\boldsymbol{H}\cdot\boldsymbol{r}$, i.e. at a fixed position, the intensity of the XSW field varies, while scanning the photon energy through the Bragg condition. This scenario is modelled in Figure 2.7 for different values of $\boldsymbol{H}\cdot\boldsymbol{r}$, each of them showing a particular curve of the XSW intensity. The maximal (minimal) normalized intensity is 4 (0) and occurs for constructive (destructive) interference of the incoming and Bragg-reflected wave, neglecting absorption. Atoms that are at a position $\boldsymbol{r}$ experience this variation of the intensity and scatter X-rays accordingly. The particularity of the slope of the XSW intensity with respect to $\boldsymbol{H}\cdot\boldsymbol{r}$ is responsible for the high precision of the XSW measurements.

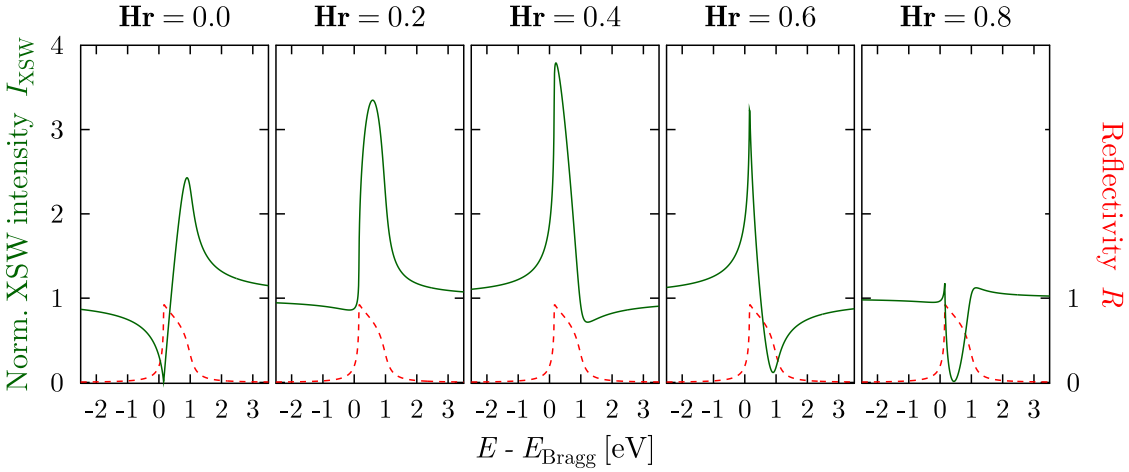

Figure 2.7: Each graph shows the intensity of the XSW field (solid line) for a certain distance to the surface (value of $\boldsymbol{H}\cdot\boldsymbol{r}$), and the reflectivity (dashed line). The intensity is normalized to the intensity of the incident beam (Equation 2.16). Here, due to destructive and constructive interference of incident and reflected beam, the normalized intensity can take extremal values between 0 (destructive interference) and 4 (constructive interference).

2.2.3 X-ray absorption from the XSW field

For the XSW analysis, a signal has to be recorded, which can be related to the intensity of the XSW field from the previous section. The process commonly exploited is the emission of electrons due to absorption of X-rays by atoms. These photoelectrons will be analyzed using a photoelectron analyzer. For completeness it should be mentioned that there are two more possibilities to detect the absorption of a photon. After the absorption of a photon and emission of a photoelectron, this excited state can decay through the creation of an Auger electron or emit fluorescence, as illustrated in Figure 2.8. Therefore, Auger-electron spectroscopy and fluorescence spectroscopy are two alternative methods to perform XSW experiments.

In the following the description is focused on the creation of photoelectrons, as in this work the XSW measurements were performed using the XPS technique.

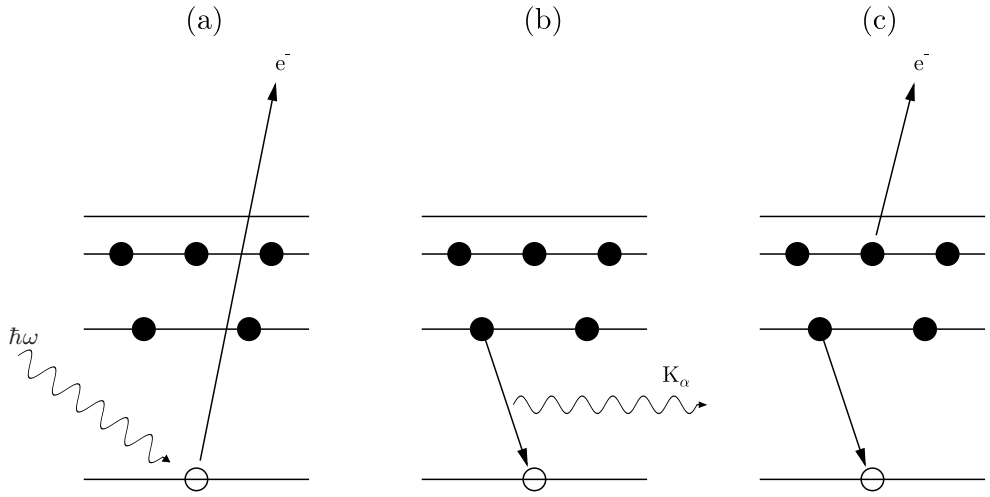

Figure 2.8: (a) Schematic of the photoeffect: A photon with sufficient energy (see Equation 2.1) removes an electron from the atom. This excitation can decay via (b) creating a photon (fluorescence) or (c) removing another electron (Auger electron) from the atom.

The interaction of light with atoms can be described by first-order perturbation theory, where the perturbation Hamilton operator $\hat{H}'$ due to radiation can be approximated as (see Section 2.1):

$$\hat{H}' = -\frac{e}{2m_\mathrm{e}c}\boldsymbol{A}\hat{p}. \tag{2.16}$$

$\hat{p} = -\mathrm{i}\hbar\boldsymbol{\nabla}$ is the momentum operator and $\boldsymbol{A}$ the vector potential of the electric field. The vector potential $\boldsymbol{A}$ of the XSW field is [39]

$$\boldsymbol{A} = \boldsymbol{A}_0 \mathrm{e}^{-2\pi\mathrm{i}\boldsymbol{k}_0\boldsymbol{R}} \left(\hat{\boldsymbol{e}}_0 + \hat{\boldsymbol{e}}_H\sqrt{R}\mathrm{e}^{\mathrm{i}\nu}\mathrm{e}^{2\pi\mathrm{i}\boldsymbol{H}\cdot\boldsymbol{R}}\right), \tag{2.17}$$

where $\hat{\boldsymbol{e}}_{0,H}$ are the polarization vectors of the incident and diffracted waves, respectively. As can be seen in Figure 2.9, the position of the center of the atom, $\boldsymbol{r}$ is related to the position of the absorbing electron $\boldsymbol{R}$ via $\boldsymbol{R} = \boldsymbol{r} + \boldsymbol{r}_\mathrm{e}$, where $\boldsymbol{r}_\mathrm{e}$ is the radial component of the wavefunction of the bound electron. This vector potential has to be inserted in

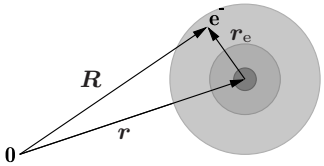

Figure 2.9: Schematic of the relation between the position of an atom $\boldsymbol{R}$, the position of the affected electron $\boldsymbol{r}_\mathrm{e}$, and the radial component of the electronic wavefunction $\boldsymbol{r}$.

Equation 2.2, and the transition matrix element M_fi for an electron being exited from the

ground state with wavefunction $\psi_\mathrm{i}(\boldsymbol{r})$ to a final state with wavefunction $\psi_\mathrm{f}(\boldsymbol{r})$ can be used to determine the differential cross section of the photoionization process:

$$\frac{\mathrm{d}\sigma}{\mathrm{d}\Omega} \propto |M_\mathrm{fi}|^2 \tag{2.18}$$

Dipole approximation

The vector potential $\boldsymbol{A}$ from Equation. 2.17 is proportional to exponential functions of the type $\mathrm{e}^{-\mathrm{i}\boldsymbol{kr}}$, which can be expressed in a Taylor expansion (multipole expansion):

$$\begin{aligned} \mathrm{e}^{-2\pi\mathrm{i}\boldsymbol{k}_0\boldsymbol{r}_\mathrm{e}} &= 1 - 2\pi\mathrm{i}\boldsymbol{k}_0\boldsymbol{r}_\mathrm{e} + 2\pi^2(\boldsymbol{k}_0\boldsymbol{r}_\mathrm{e})^2 - \ldots \\ \mathrm{e}^{-2\pi\mathrm{i}\boldsymbol{H}_0\boldsymbol{r}_\mathrm{e}} &= 1 - 2\pi\mathrm{i}\boldsymbol{H}\boldsymbol{r}_\mathrm{e} + 2\pi^2(\boldsymbol{H}\boldsymbol{r}_\mathrm{e})^2 - \ldots \end{aligned} \tag{2.19}$$

The so called dipole approximation considers only the zeroth order term and hence simplifies Equation 2.17 to

$$\boldsymbol{A} = \boldsymbol{A}_0\mathrm{e}^{-2\pi\mathrm{i}\boldsymbol{k}_0\boldsymbol{r}}(\hat{\boldsymbol{e}}_0 + \hat{\boldsymbol{e}}_H\sqrt{R}\mathrm{e}^{\mathrm{i}\nu}\mathrm{e}^{2\pi\mathrm{i}\boldsymbol{H}\cdot\boldsymbol{r}}) \tag{2.20}$$

The benefit of the dipole approximation is that now the vector potential $\boldsymbol{A}$ no longer depends on $\boldsymbol{r}_\mathrm{e}$. Therefore, the transition matrix element is proportional to $\boldsymbol{A}$:

$$M_\mathrm{fi} \propto \boldsymbol{A}\int \mathrm{d}^3\boldsymbol{r}_\mathrm{e}\psi_\mathrm{f}^*\hat{p}\psi_\mathrm{i} \tag{2.21}$$

In this case the differential cross section of the photoemission process caused by the XSW field is proportional to the intensity of the XSW field, via

$$\frac{\mathrm{d}\sigma}{\mathrm{d}\Omega} \propto |M_\mathrm{fi}|^2 \propto \boldsymbol{A}^2 \propto |1 + \sqrt{R}\mathrm{e}^{\mathrm{i}(\nu - 2\pi\boldsymbol{H}\cdot\boldsymbol{r})}|^2 = I_\mathrm{XSW} \tag{2.22}$$

This equation means that, within the dipole approximation, the number of measured photoelectrons is proportional to the intensity of the XSW field. Equation 2.22 holds for linearly polarized light, where $\hat{\boldsymbol{e}}_0 = \hat{\boldsymbol{e}}_H = \hat{1}$.

The dipole approximation is valid if $\boldsymbol{k}_0\boldsymbol{r}_\mathrm{e} \ll 1$. In other words, the wavelength of the radiation has to be large compared to the radial wavefunction of the absorbing electron. Especially for hard X-rays and for orbitals with an extended radial wavefunction the dipole approximation leads to significant deviations in the XSW results, and higher-order terms in the Taylor expansion 2.19 have to be considered to get reasonable results. The XSW analysis beyond the dipole approximation is explained in Section 2.2.5.

2.2.4 XSW technique within the dipole approximation

In the last section it was pointed out that – in the dipole approximation – the cross section for the photoemission process is proportional to the intensity of the XSW field. Recalling Section 2.2.2, the XSW intensity varies at a fixed position $\boldsymbol{r}$ while scanning the

photon energy through the Bragg condition. Therefore, the y-axis in Figure 2.7 can be named with the intensity of photoelectrons, or photoelectron yield. I_{XSW} in Equation 2.16 can be replaced by the the photoelectron yield Y_{P}:

$$Y_{\mathrm{P}}(\nu, \boldsymbol{r}) = 1 + R + 2\sqrt{R}\,\cos(\nu - 2\pi.\boldsymbol{H}\cdot\boldsymbol{r}) \tag{2.23}$$

This quantity can be measured experimentally by the XPS technique. In Figure 2.7 different values of $\boldsymbol{H}\cdot\boldsymbol{r}$ are displayed, showing a very particular shape of the intensity variation for each $\boldsymbol{H}\cdot\boldsymbol{r}$.

Instead of the position of a atom $\boldsymbol{r}$ we consider only distances z, measured from a diffraction plane in the direction of $\boldsymbol{H}$. The scalar product $\boldsymbol{H}\cdot\boldsymbol{r}$ is then just

$$|\boldsymbol{H}|\cdot|\boldsymbol{r}| = \frac{1}{d_0}\cdot z \tag{2.24}$$

where d_0 is the lattice spacing of the corresponding Bragg reflection. Until now only one atom is considered, which is emitting a photoelectron due to the XSW field. In experiments, the number of analyzed atoms from a particular chemical species (e.g. element) is many orders of magnitude higher, and the positions of the atoms typically vary due to static disorder or thermal vibrations. This spread of atomic positions can be taken into account with a distribution function $G(z)$, which is integrated over the possible distances z within a wavelength of the XSW field and normalized such that $\int_0^{d_0} G(z)\mathrm{d}z = 1$. Equation 2.23 is then

$$Y_{\mathrm{P}} = 1 + R + 2\sqrt{R}\int_0^{d_0} G(z)\cos(\nu - 2\pi\,{}^{z}\!/_{d_0})\mathrm{d}z \tag{2.25}$$

For the analysis of the XSW data, one introduces in Equation 2.25 two fitting parameters, the coherent fraction f_H and coherent position P_H, which contain the structural information of the analyzed sample:

$$Y_{\mathrm{P}} = 1 + R + 2\sqrt{R}\,f_H\cos(\nu - 2\pi P_H) \tag{2.26}$$

The coherent position takes values between 0 and 1. It is related to the bonding distance d_H being measured in the direction of $\boldsymbol{H}$ relative to the lattice planes of the $\boldsymbol{H}$-Bragg reflection:

$$d_H = (n + P_H)d_0 \quad n = 0, 1, 2, \ldots \tag{2.27}$$

The n-ambiguity of the coherent position originates from the XSW field, which has the periodicity d_0. The coherent fraction also takes values between 0 and 1 and describes the degree of order of the analyzed atoms. Further interpretation of f_H can be achieved using the equivalence of Equations 2.25 and 2.26:

$$f_H\cos(\nu - 2\pi P_H) = \int_0^{d_0} G(z)\cos(\nu - 2\pi\,{}^{z}\!/_{d_0})\mathrm{d}z \tag{2.28}$$

The cosine on both sides can be expanded by

$$\begin{aligned}\cos\nu f_H\cos(2\pi P_H)+\sin\nu f_H\sin(2\pi P_H)=\cos\nu\int_0^{d_0}G(z)\cos(2\pi\,{}^{z}\!/_{d_0})\mathrm{d}z\\ +\sin\nu\int_0^{d_0}G(z)\sin(2\pi\,{}^{z}\!/_{d_0})\mathrm{d}z\end{aligned}\tag{2.29}$$

This equation must be valid for all phases ν. Additionally, the sine and cosine are linear independent functions. This leads to the consequence that the coefficients of $\cos\nu$ and $\sin\nu$ on both sides of the equation must be equal:

$$f_H\cos(2\pi P_H)=\int_0^{d_0}G(z)\cos(2\pi\,{}^{z}\!/_{d_0})\mathrm{d}z \tag{2.30a}$$

$$f_H\sin(2\pi P_H)=\int_0^{d_0}G(z)\sin(2\pi\,{}^{z}\!/_{d_0})\mathrm{d}z \tag{2.30b}$$

Multiplying Equation 2.30b with $\mathrm{i}=\sqrt{-1}$ and summing up both equations, a different way of displaying f_H and P_H is achieved:

$$f_H\mathrm{e}^{2\pi\mathrm{i}P_H}=\int_0^{d_0}G(z)\mathrm{e}^{2\pi\mathrm{i}\,{}^{z}\!/_{d_0}}\mathrm{d}z \tag{2.31}$$

From this formula one can deduce that f_H is the first Fourier component of the distribution function $G(z)$, multiplied with a phase factor, which contains P_H. By measuring the coherent fraction and coherent position for different $\boldsymbol{H}$ reflections one obtains sufficient Fourier components to reconstruct the distribution function $G(\boldsymbol{r})$ of the analyzed atoms [42]. This technique enables the determination of relatively complicated crystal structures, e.g. the structure of the high-temperature superconductor $YBa_2Cu_3O_{7-\delta}$ [43, 44].

The coherent fraction is a measure for the distribution of the atoms along the $\boldsymbol{H}$-axis. This spread of positions can have different origins. First, the thermal vibrations of the atoms, which are considered in the Debye-Waller factor D_H. Second, the static disorder of the atoms, which can be described by a geometric factor a_H. A third factor C describes the fraction of atoms, which are not randomly disordered along the $\boldsymbol{H}$-axis. f_H now has the form

$$f_H=Ca_HD_H. \tag{2.32}$$

All three parameters take values between 0 and 1, and only a_H can influence the coherent position of the atoms. Usually the ordered fraction C can be split up into N groups of atoms, each of which is at an ordered position with an occupation fraction $c_1, c_2, c_3, \ldots$ such that

$$C=\sum_{j=1}^{N}c_j \tag{2.33}$$

For these ordered atoms one can introduce a geometrical structure factor S_H, which is connected to the geometrical factor a_H:

$$S_H=\frac{1}{C}\sum_{j=1}^{N}\left[c_j\mathrm{e}^{2\pi\mathrm{i}P_H^j}\right]\qquad a_H=|S_H| \tag{2.34}$$

To get a coherent fraction $f_H = 1$, all three parameters must be 1, which means that all atoms are perfectly aligned at one position z relative to the diffracting plane and not vibrating. The other extremal case, $f_H = 0$, can be achieved by different situations. Either if all atoms are randomly disordered along the $\boldsymbol{H}$-axis ($C = 0$) or if the static distribution of different positions cancels their contribution to the photoelectron yield out ($a_H = 0$). These scenarios can be illustrated by displaying the result of Equation 2.31 in the Argand diagram, in which f_H is the length of the vector and $2\pi P_H$ the angle relative to the positive x-axis. The previously described scenarios are shown in Figure 2.10. Note that $P_H = 1$ is equivalent to $P_H = 0$. The physical reason for this property is rooted in the periodicity of the XSW field.

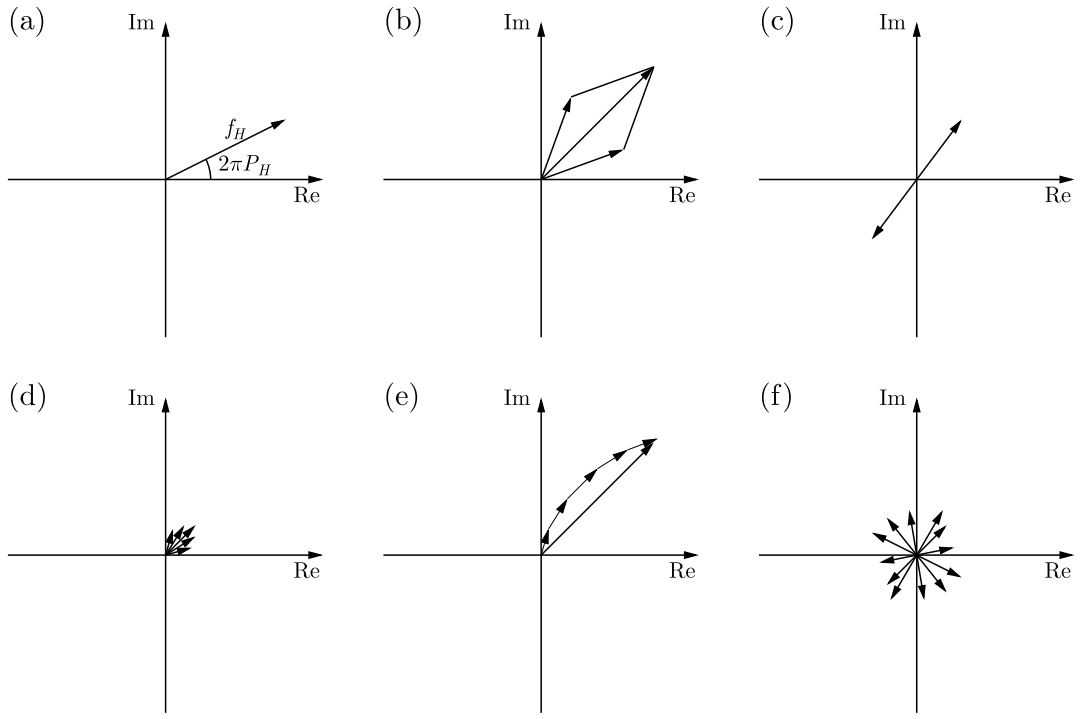

Figure 2.10: (a) The Argand diagram can be used to display XSW results, where f_H is the length of the vector and $2\pi P_H$ the angle relative to the positive x-axis. (b) Two equally occupied positions lead to a resultant f_H and P_H. (c) Special case of (b): Two equally occupied atomic positions are spaced by $d_0/2$, i.e. by an angle of π in the Argand diagram, and their contribution to the normalized photoelectron yield cancel each other out ($a_H = 0$). (d) Gaussian distribution of atomic positions due to thermal vibrations around a certain position, (e) resulting in a decrease of f_H, while P_H remains unaffected. (f) A random distribution of atomic positions ($C = 0$) causes $f_H = 0$.

2.2.5 XSW analysis beyond the dipole approximation

In Section 2.2.3, the XSW technique was described within the dipole approximation. This approximation breaks down if the wavelength of the X-rays is in the order of the

radial component of the wavefunction of the electrons, and the assumption $\boldsymbol{k}_0\boldsymbol{r}_\mathrm{e} \ll 1$ is not valid any more. The general transition matrix element for the photoeffect caused by the XSW field has the form [45]

$$M_\mathrm{fi} = E_0 \mathrm{e}^{\mathrm{i}\boldsymbol{k}_0\boldsymbol{r}} \left[M_\mathrm{fi}\left(\boldsymbol{s}_0\right) + \left(\frac{E_H}{E_0}\right) \mathrm{e}^{\mathrm{i}\boldsymbol{H}\boldsymbol{r}} M_\mathrm{fi}\left(\boldsymbol{s}_H\right), \right] \tag{2.35}$$

where $\boldsymbol{r}$ points to the center of the atom, $\boldsymbol{s}_{0,H}$ denotes the propagation vector and $M_\mathrm{fi}\left(\boldsymbol{s}_0\right)$ and $M_\mathrm{fi}\left(\boldsymbol{s}_H\right)$ the transition matrix elements corresponding to the incident and diffracted wave, respectively:

$$\begin{aligned} M_\mathrm{fi}\left(\boldsymbol{s}_0\right) &= \left\langle \psi_\mathrm{f} \middle| \mathrm{e}^{2\pi\boldsymbol{k}_0\boldsymbol{r}_\mathrm{e}} (\hat{\boldsymbol{e}}_0\hat{p}) \middle| \psi_\mathrm{i} \right\rangle \\ M_\mathrm{fi}\left(\boldsymbol{s}_H\right) &= \left\langle \psi_\mathrm{f} \middle| \mathrm{e}^{2\pi\boldsymbol{k}_H\boldsymbol{r}_\mathrm{e}} (\hat{\boldsymbol{e}}_0\hat{p}) \middle| \psi_\mathrm{i} \right\rangle \end{aligned} \tag{2.36}$$

Using the multipole expansion to the exponential function in Equation 2.36,

$$\mathrm{e}^{-\mathrm{i}\boldsymbol{k}_{0,H}\boldsymbol{r}_\mathrm{e}} = 1 - 2\pi\mathrm{i}\boldsymbol{k}_{0,H}\boldsymbol{r}_\mathrm{e} + 2\pi^2(\boldsymbol{k}_{0,H}\boldsymbol{r}_\mathrm{e})^2 - \ldots \tag{2.37}$$

and considering the first-order term, the transition matrix elements for both photon propagation directions can be split up in a component for electric dipole transitions and one for electric quadrupole transitions[1]:

$$\begin{aligned} M_\mathrm{fi}\left(\boldsymbol{s}_0\right) &= M_\mathrm{fi}^\mathrm{D} + M_\mathrm{fi}^\mathrm{Q}\left(\boldsymbol{s}_0\right) \\ M_\mathrm{fi}\left(\boldsymbol{s}_H\right) &= M_\mathrm{fi}^\mathrm{D} + M_\mathrm{fi}^\mathrm{Q}\left(\boldsymbol{s}_H\right) \end{aligned} \tag{2.38}$$

If the initial state is an s-orbital, the dipole transition corresponds to the s→p transition, the quadrupole transition to the s→d transition.

The photoelectron yield Y_P is linked by the differential cross section $\mathrm{d}\sigma/\mathrm{d}\Omega$ to the transition matrix element M_fi via

$$\begin{aligned} Y_\mathrm{P}(\Omega) \propto \frac{\mathrm{d}\sigma}{\mathrm{d}\Omega} &\propto \left\langle \left| M_\mathrm{fi} \right|^2 \right\rangle \\ &= |E_0|^2 \left[S_{00} + S_{HH}R + 2\sqrt{R}\, Re\left\{ S_{0H} \mathrm{e}^{\mathrm{i}(\nu + 2\pi\boldsymbol{H}\cdot\boldsymbol{r})} \right\} \right] \end{aligned} \tag{2.39}$$

As before, $R = {|E_H|^2}/{|E_0|^2}$ is the reflectivity of the crystal. Three new parameters are introduced:

$$\begin{aligned} S_{00} &= \left\langle \left| M_\mathrm{fi}\left(\boldsymbol{s}_0\right) \right|^2 \right\rangle \\ S_{HH} &= \left\langle \left| M_\mathrm{fi}\left(\boldsymbol{s}_H\right) \right|^2 \right\rangle \\ S_{0H} &= \left\langle M_\mathrm{fi}\left(\boldsymbol{s}_0\right)^* M_\mathrm{fi}\left(\boldsymbol{s}_H\right) \right\rangle \end{aligned} \tag{2.40}$$

[1] The second term in the multipole expansion gives additionally *magnetic* dipole transitions. Yet, for our circumstances, they are negligible [46].

These parameters are proportional to the cross section of the direct scattered beams (S_{00} and S_{HH}) and the interfering beam (S_{0H}). The latter parameter may even be complex and therefore lead to an additional phase shift $\Psi = \arg(S_{0H}/S_{00})$ for the interference term.

The photoelectron yield in Equation 2.26 can now be written in a more general way,

$$Y_{\mathrm{P}}(\Omega) = 1 + S_R R + 2|S_I|\sqrt{R} f_H \cos(\nu - 2\pi P_H + \Psi) \tag{2.41}$$

containing new non-dipole parameters S_R, S_I, and Ψ:

$$S_R = \frac{S_{HH}}{S_{00}}, \quad S_I = |S_I| \mathrm{e}^{\mathrm{i}\Psi} = \frac{S_{0H}}{S_{00}} \tag{2.42}$$

In case the experiments are performed in backscattering geometry, i.e. for NIXSW experiments, the three non-dipole parameters are not independent:

$$|S_I| = \frac{1}{2}(S_R + 1)\sqrt{1 + \tan^2 \Psi} \tag{2.43}$$

The quantum mechanical origin of the phase shift Ψ lies in the partial phase shifts δ_p and δ_d of the final electron p- and d-states, respectively:

$$\Psi = \tan^{-1}\left(\frac{S_R - 1}{S_R + 1}\tan \Delta\right) \qquad \text{with } \Delta = \delta_d - \delta_p \tag{2.44}$$

One additional consequence of the non-dipole correction in the normal incidence geometry is a difference of the photoemission cross section for the incoming and the diffracted beam, as now the transition matrix element depends on the direction of the propagating wave ($\boldsymbol{s}_{0,H}$). The differential cross section of the photoemission process in the non-dipole approximation can be parametrized for linearly polarized light as [47]:

$$\frac{d\sigma}{d\Omega} = \frac{\sigma}{4\pi}\left[1 + \frac{\beta}{2}\left(\frac{3\cos^2\Theta - 1}{2}\right) + \left(\delta + \gamma\cos^2\Theta\right)\sin\Theta\cos\phi\right], \tag{2.45}$$

where β is the dipole asymmetry parameter ($\beta = 0$ would mean isotropic emission of photoelectrons in the dipole approximation), δ and γ are the quadrupole asymmetry parameters. Θ is the angle of photoelectron detection measured relative to the polarization vector in the y-z- plane. ϕ, the angle between the direction of the travelling wave and the projection of the photoelectron detection in the x-z-plane, changes from 0° to 180° if the beam is diffracted, and the non-dipole corrections in Equation 2.45 are added or subtracted, respectively. Both cases are illustrated in Figure 2.11.

An alternative way to describe this asymmetry is to introduce a forward/backward asymmetry parameter $Q = \gamma/3 \ \sin\Theta$. The deviation from the dipole case in the forward [Figure 2.11(a)] and backward [Figure 2.11(b)] photoemission is $(1+Q)$ and $(1-Q)$, respectively. Now, the non-dipole parameter S_R can be written as

$$S_R = \frac{(1+Q)}{(1-Q)} \tag{2.46}$$

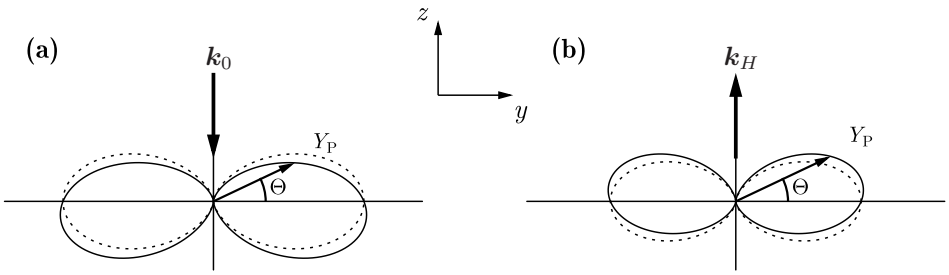

Figure 2.11: Schematic picture of the angular dependence of the photoemission cross section in a NIXSW experiment, if non-dipole effects are taken into account (solid line). The shape of the solid lines emerges from asymmetry parameters $\beta = 2$, $\delta = 0$, and $\gamma = 1$ (see Equation 2.45). The surface normal is parallel to the z-axis. The dashed line expresses the shape for the dipole approximation with $\delta = 0$ and $\gamma = 0$. The photoemission yield $Y_P \propto \sigma$ differs in general for the incident (a) and reflected (b) wave. A reflectivity of $R = 0.85$ was used in this figure. Note that at photoelectron detection angle $\Theta = 0°$ non-dipole effects do not exist. At this angle, the position of the dashed curve coincidences with the solid curve, and the dipole approximation describes the photoemission process exactly.

Incoherent layers

The non-dipole parameter S_R from the previous section can be determined experimentally. For relatively thick molecular coverages the distances of the atoms can be considered to be randomly distributed with respect to the diffraction plane. Figure 2.10 (f) illustrates this case, in which $C = 0$. Therefore, the coherent fraction is $f_H = 0$, and Equation 2.41 simplifies to

$$Y_P = 1 + S_R R. \tag{2.47}$$

By measuring the photoelectron yield Y_P and the reflectivity R, the determination of the non-dipole parameter S_R is possible.

2.3 Determination of the molecular coverage

In surface science, the properties of the analyzed system often depend on the molecular film coverage. The first molecular layer on top of the substrate often interacts more strongly with the substrate than the above located molecules, which can lead to significantly different properties compared to the bulk or multilayer film. Especially the XSW technique yields sensible results as long as the molecular coverage is below or equal to one ML. If thicker films are prepared, the XSW result will be an average over molecules which adsorb in the first and higher layers, and one cannot speak any more of determined bonding distances between metal and molecule. To present reasonable and valuable XSW results, it is important to verify that the coverage of the molecular film is (below) one ML. Additionally, the knowledge of the molecular coverage can be used to investigate the dependence

of a certain property on the coverage. In that case, the coverage can be considered as the molecular density within the first layer.

The method of calculating molecular coverages on metal substrates is based on the ratio of photoelectron peak intensities of core-levels from an adsorbate atom and from a substrate atom. It was developed in 1976 [48, 49] for impurity atoms and later extended to molecules on surfaces [50]. The peak intensity is defined as the integrated area of a peak after background subtraction and depends on the cross section σ of an atom. The differential photoionization cross section takes into account the non-isotropic emission of photoelectrons from the sample. It is defined within the dipole approximation for *circularly and unpolarized* X-rays [51]:

$$\frac{\mathrm{d}\sigma}{\mathrm{d}\Omega} = \frac{\sigma}{4\pi}\left[1 - \frac{\beta}{4}\left(3\cos^2\vartheta - 1\right)\right] \tag{2.48}$$

and for *linearly polarized* X-rays [52]

$$\frac{d\sigma}{d\Omega} = \frac{\sigma}{4\pi}\left[1 + \frac{\beta}{2}\left(3\cos^2\vartheta - 1\right)\right] \tag{2.49}$$

with β being the asymmetry parameter of the photoelectron angular distribution. In the case of linearly polarized X-rays, ϑ is the angle between the polarization vector and the direction of the photoelectron analyzer. For circular and unpolarized X-rays, ϑ is the angle between incoming photons and detected electrons. An example for unpolarized X-rays is the Mg/Al K_α radiation; linearly polarized X-rays are commonly supplied by synchrotron facilities.

Going beyond the dipole approximation one has to use the two quadrupole parameters γ and δ [51]. Calculations of the three angular distribution parameters (β, γ, and δ) for elements from $Z = 1$ to $Z = 100$ can be found in Ref. [51, 53]. Now the differential photoionisation cross section for *unpolarized/circularly polarized* photons can be written as

$$\frac{d\sigma}{d\Omega} = \frac{\sigma}{4\pi}\left[1 - \frac{\beta}{2}\left(\frac{3\cos^2\vartheta - 1}{2}\right) + \left(\frac{\gamma}{2}\sin^2\vartheta + \delta\right)\cos\vartheta\right] \tag{2.50}$$

and for *linearly polarized* photons we have

$$\frac{d\sigma}{d\Omega} = \frac{\sigma}{4\pi}\left[1 + \frac{\beta}{2}\left(\frac{3\cos^2\vartheta - 1}{2}\right) + \left(\delta + \gamma\cos^2\vartheta\right)\sin\vartheta\cos\phi\right] \tag{2.51}$$

Now we want to calculate the amount of photoelectrons coming from the substrate surface, which is limited by inelastic scattering within the substrate. For that purpose it is necessary to know the inelastic mean free path λ_S, which is the maximal depth from where photoelectrons from a given subshell can escape from the substrate without being involved in an inelastic scattering process:

$$\lambda_\mathrm{S} = \frac{E^\mathrm{S}_\mathrm{kin}}{a(\ln E^\mathrm{S}_\mathrm{kin} + b)} \tag{2.52}$$

Here, $E_{\mathrm{kin}}^{\mathrm{S}}$ is the kinetic energy of the photoelectrons of the substrate. a and b are element specific constants taken from [54]. Therefore the area A of the substrate can be described as

$$A_{\mathrm{S}} = \frac{M_{\mathrm{S}}}{\rho_{\mathrm{S}} \lambda_{\mathrm{S}} N} \tag{2.53}$$

where M_{S} is the molar mass of the substrate, ρ_{S} its density, and N Avogadro's number. Now we can calculate the number of adsorbate atoms n_{A} per area of the substrate surface

$$n_{\mathrm{A}} = \frac{E_{\mathrm{kin}}^{\mathrm{A}}}{E_{\mathrm{kin}}^{\mathrm{S}}} \times \frac{I_{\mathrm{A}}}{I_{\mathrm{S}}} \times \frac{\sigma'_{\mathrm{S}}}{\sigma'_{\mathrm{A}}} \times \frac{\cos\phi}{A_{\mathrm{S}}} \tag{2.54}$$

ϕ stands for the angle between surface normal and detected photoelectrons. The final coverage can be calculated considering the amount of adsorbate atoms per molecule, n_{M}, and the size of the 2D unit cell, A_{uc}, of the molecule adsorbed on that metal. The molecular coverage Θ is then

$$\Theta = \frac{n_{\mathrm{A}} \cdot A_{\mathrm{uc}}}{n_{\mathrm{M}}}, \tag{2.55}$$

given in ML.

In this calculation the attenuation of the XPS peak intensity of the substrate due to inelastic scattering of the photoelectrons with the molecules is neglected. Therefore, this analysis is only valid for small coverages of molecules. Above one ML less photoelectrons of the substrate will reach the surface unscattered, and this approach will overestimate the molecular coverage.

Additional uncertainty emerges from the dependence of the intensity ratio of the growth mode. For thicker films beyond one ML nominal coverage, a molecular film showing island-growth will exhibit areas of the uncovered substrate, leading to a relatively high substrate signal in XPS. Therefore, the intensity ratio will be lower for that case compared to a perfect layer-by-layer-growth, although the same number of molecules is deposited. However, for coverages below one ML the island-growth can be neglected.

Chapter 3

Materials

At the beginning of this chapter, all compounds used in this work are listed. Then, the crystal and XPS properties of the Cu(111), Ag(111), and Au(111) single crystals are reported. At the end, the preparation procedure of the samples and the data analysis will be described.

3.1 Compounds

This section provides an overview of organic semiconducting molecules, which were studied in this thesis. The term *molecular backbone* or *skeleton* appears frequently there. It is related to the part of a molecule, in which all or the majority of the carbon atoms are located. It is also the place of π-conjugation. Some molecules contain additionally side groups and heteroatoms, which are in most cases bound to the backbone.

The list of the molecules is built up in the following way: At the left hand side the chemical structure is shown, while at the right hand side the name of the molecule (acronym in parenthesis), the molecular formula, and the molecular weight are noted.

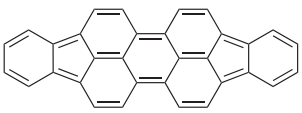

Diindenoperylene (DIP)
Chemical formula: $C_{32}H_{16}$
Molecular weight: 400 g/mol

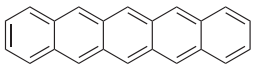

Pentacene (PEN)
Chemical formula: $C_{22}H_{14}$
Molecular weight: 278 g/mol

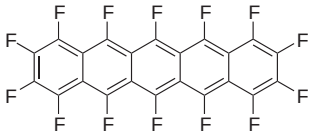

Perfluoropentacene (PFP)
Chemical formula: $C_{22}F_{14}$
Molecular weight: 530 g/mol

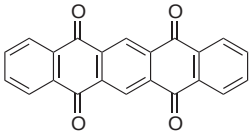

Pentacene-5,7,12,14-tetraone (P4O)
Chemical formula: $C_{22}H_{10}O_4$
Molecular weight: 338 g/mol

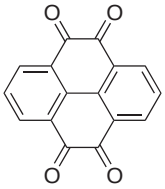

Pyrene-4,5,9,10-tetraone (PYT)
Chemical formula: $C_{16}H_6O_4$
Molecular weight: 262 g/mol

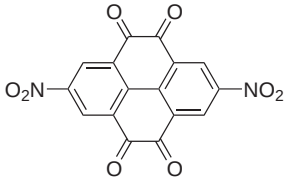

2,7-Dinitropyrene-4,5,9,10-tetraone (NO2PYT)
Chemical formula: $C_{16}H_4N_2O_8$
Molecular weight: 352 g/mol

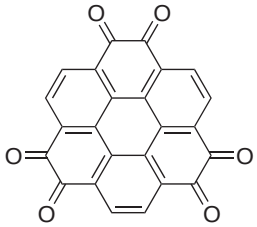

Coronene-hexaone (COHON)
Chemical formula: $C_{24}H_6O_6$
Molecular weight: 390 g/mol

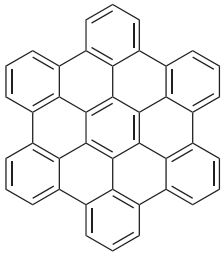

Hexa-*peri*-hexabenzocoronene (HBC)
Chemical formula: $C_{42}H_{18}$
Molecular weight: 522 g/mol

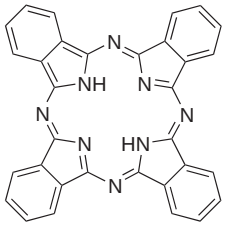

29*H*, 31*H*-**Phthalocyanine** (H2Pc)
Chemical formula: $C_{32}H_{18}N_8$
Molecular weight: 514 g/mol

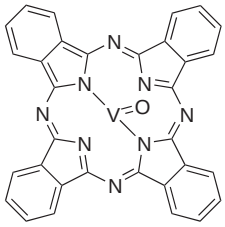

Vanadium(IV) oxide phthalocyanine (VOPc)
Chemical formula: $C_{32}H_{16}VON_8$
Molecular weight: 579 g/mol

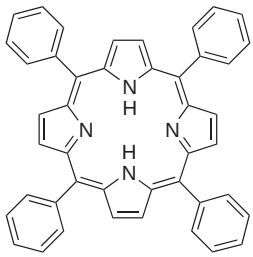

Tetraphenylporphyrin (2HTPP)
Chemical formula: $C_{44}H_{30}N_4$
Molecular weight: 614 g/mol

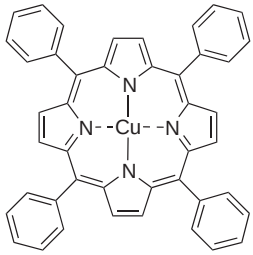

Copper(II)-tetraphenylporphyrin (CuTPP)
Chemical formula: $C_{44}H_{28}CuN_4$
Molecular weight: 675 g/mol

3.2 Substrates

Three coinage metal substrates were used in this work: Cu(111), Ag(111), and Au(111). The Cu(111) and Ag(111) single crystal were purchased from MaTecK GmbH, the Au(111) crystal from Escete Single Crystal Technology B.V. The metals form a face-centered cubic (fcc) lattice structure. The atoms of their (111) surfaces are arranged in hexagonal pattern with a threefold symmetry. The Au(111) crystal undergoes surface reconstruction [55], thereby increasing the distance between the first and second atomic layer by 3% [56]. For the correct interpretation of XSW data this property has to be considered.

Prior to each use of the crystals, repeated cycles of Ar^+ sputtering and annealing to ∼500 °C were applied to the metal substrates. The surface cleanliness was checked with XPS. Figure 3.1 shows XPS surveys of the clean Cu(111), Ag(111), and Au(111) substrates. For the XP spectra, the x-axis (binding energy) was calibrated such that the Fermi edge was set to $E_B = 0$ eV. Figure 3.2 shows XSW scans of the crystals. All XSW scans displayed in this thesis are organized in the way shown here. The lowest curve displays

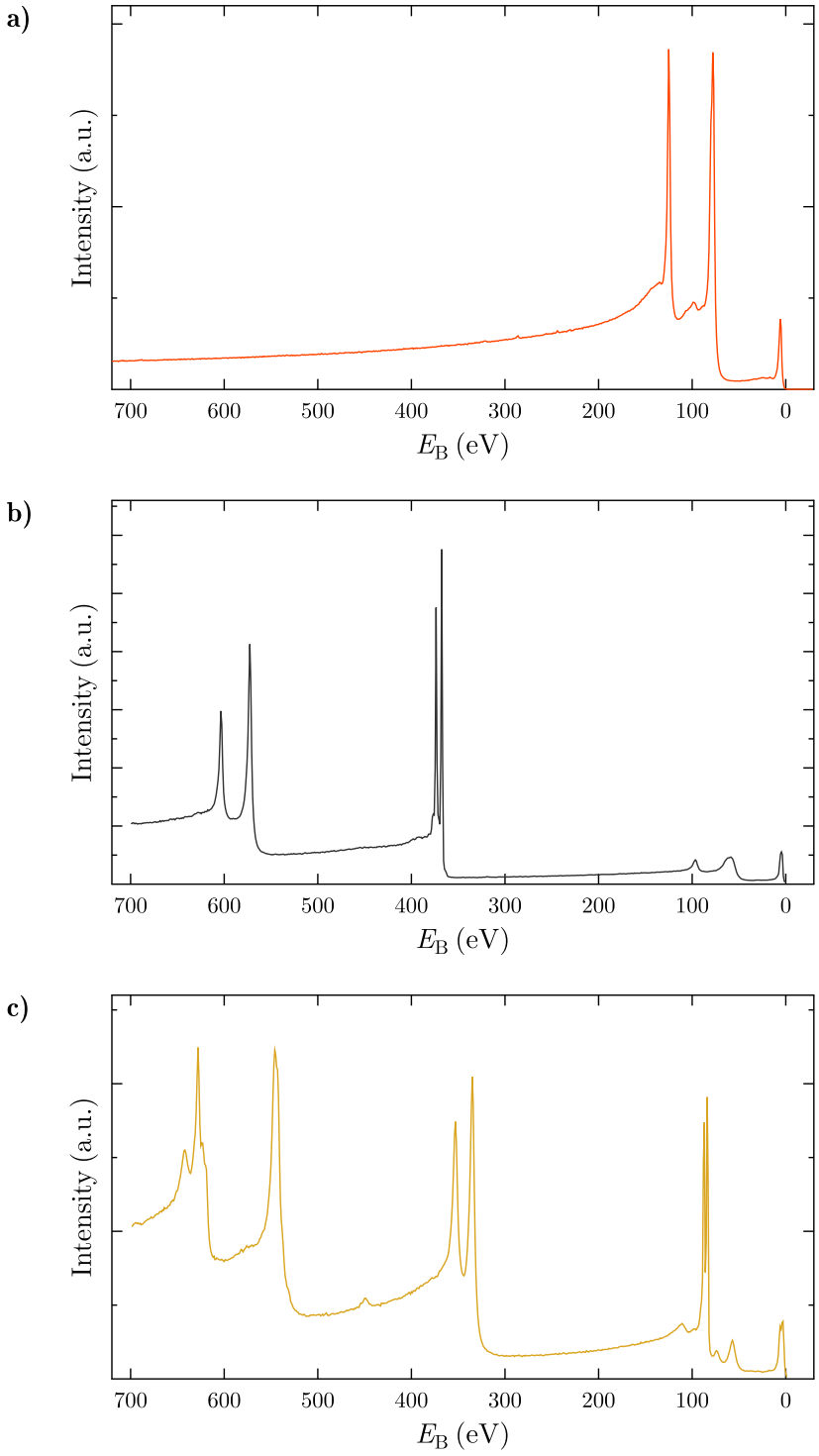

Figure 3.1: XPS survey of the clean Cu(111), Ag(111), and Au(111) substrate (from (a) to (c)).The x-axis (binding energy) was calibrated such that the Fermi edge was set to $E_B = 0$ eV.

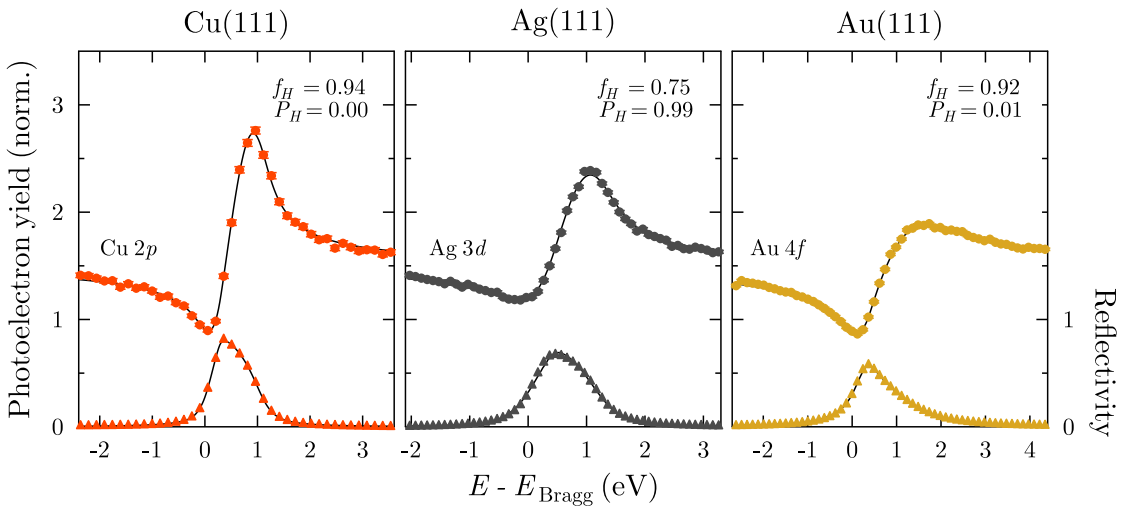

Figure 3.2: Bragg scans of the Cu(111), Ag(111), and Au(111) single crystals. For a Bragg angle of 88°, the (111) Bragg energies are 2.972 keV, 2.630 keV, and 2.634 keV, respectively. The *FWHM* of the reflectivity curves are: Cu(111): 0.87 eV, Ag(111): 1.18 eV, and Au(111): 1.12 eV.

the Bragg-reflected X-ray intensity ("Reflectivity") the upper curve depicts the normalized photoelectron yield of one or more chemical species.

The substrate XSW scans reveal high f_H values, which correspond to a high vertical order, and indicate that the substrates have a high crystallinity. The coherent positions are, as expected, close to 0 or 1. For P_H both values are equivalent, which can be rationalized using the Argand diagram described in Figure 2.10. The widths of the individual Bragg reflections are 0.87 eV, 1.18 eV, and 1.12 eV for the Cu(111), Ag(111), and Au(111) crystals. The layer spacings d_0 corresponding to this Bragg reflection are for Cu(111) 2.086 Å, for Ag(111) 2.357 Å, and for Au(111) 2.353 Å. More parameters of the substrates can be found in Table 3.1.

3.3 Sample preparation

The organic compounds were filled in powder form into the crucibles of a Knudsen cell and degassed thoroughly under UHV conditions. A detailed description of the Knudsen cell can be found in Section 4.3. Using a quartz crystal microbalance (QCM), the evaporation of the molecules was monitored. When the evaporation rate was constant, a clean metal crystal was put at the position of the QCM for the desired duration of deposition. Typical deposition rates were 0.1 Å/s to 0.5 Å/s. The final coverages of the samples were calculated as described in Section 2.3 and are summarized in Appendix A.3.

Table 3.1: Properties of the Cu(111), Ag(111), and Au(111) single crystals: Unit cell constant, lattice spacing d_0 associated with the (111) Bragg reflection, Bragg energy at (almost) normal incidence conditions (88° with respect to the surface), the *FWHM* of the (111) reflection, and real and imaginary parts of the crystal susceptibilities χ for the incoming and Bragg reflected wave.

	Cu(111)	Ag(111)	Au(111)
Unit cell constant a (Å)	3.615	4.085	4.078
(111) Lattice spacing d_0 at RT (Å)	2.086	2.357	2.353
Bragg energy at 88° (keV)	2.972	2.630	2.634
FWHM of (111) Bragg reflection (eV)	0.87	1.18	1.12
$\mathrm{Re}\{\chi_0\}$	$-3.84 \cdot 10^{-4}$	$-4.70 \cdot 10^{-4}$	$-6.11 \cdot 10^{-4}$
$\mathrm{Im}\{\chi_0\}$	$-4.52 \cdot 10^{-5}$	$-5.70 \cdot 10^{-5}$	$-3.40 \cdot 10^{-4}$
$\mathrm{Re}\{\chi_H\}$	$-2.81 \cdot 10^{-4}$	$-3.49 \cdot 10^{-4}$	$-4.62 \cdot 10^{-4}$
$\mathrm{Im}\{\chi_H\}$	$-4.37 \cdot 10^{-5}$	$-5.60 \cdot 10^{-5}$	$-3.40 \cdot 10^{-4}$

Chapter 4

Experimental Setup

The experiments presented in Chapter 5 were performed at the European Synchrotron Radiation Facility (ESRF, beamline ID32) and at the Diamond Light Source (DLS, beamline I09). In this chapter, the end stations of both beamlines will be described.

4.1 Experimental setup at the ESRF

The majority of the XSW experiments shown in this work were performed at the insertion device beamline ID32 at the ESRF in Grenoble (France). In 2010, the setup and equipment of the end station changed substantially. Therefore, the old and the new setup will be described in the following.

The beamline emitted linearly polarized X-rays, with the polarization vector being in the plane of the synchrotron storage ring. The Bragg-reflected intensity (reflectivity) was monitored using the photocurrent of the fluorescence screen, which was installed inside the UHV chamber. The XSW experiments were always carried out in back-reflection geometry. In other words, the angle of the X-rays with respect to the surface was close to 90°.

4.1.1 XSW setup at the ESRF until 2009

The old XSW setup [57], which was in use until 2009, consisted of a combined preparation and analysis chamber, which was pumped by a turbo molecular pump and ion getter pump. The base pressure was at $\sim 5.0 \times 10^{-10}$ mbar. For the cleaning of the metal single crystals, an installation for Ar^+ sputtering was allocated. Knudsen cells and a quartz crystal microbalance (QCM) were mounted on free flanges prior to the experiments. A hemispherical Perkin Elmer PHI Model 10-360 electron analyzer was placed with an angle of 45° relative to the direction of the incident beam, in the plane of the polarization vector. Figure 4.1 depicts the relevant components of the UHV chamber.

As a consequence of the photoelectron emission angle of 45° relative to the incident X-rays, the non-dipole parameters S_R, $|S_I|$, and ψ are required for the XSW analysis. At this analyzer angle, the dipole approximation leads to significant deviations of the photoelectron yield curve and thus to wrong results [52, 58]. The S_R parameter was

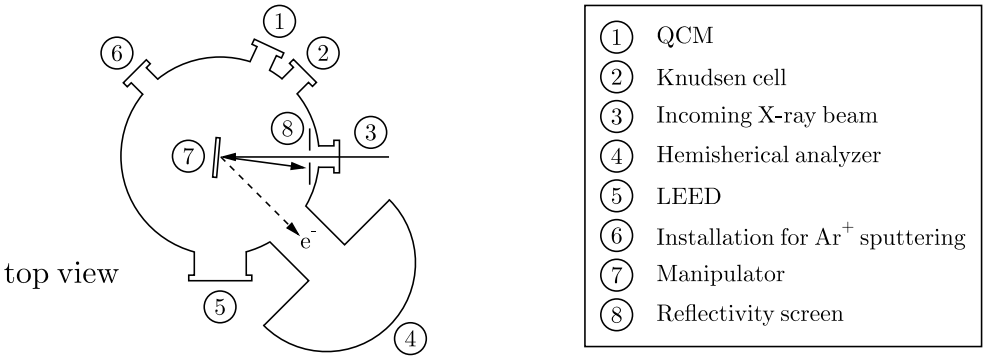

Figure 4.1: Schematic picture of the chamber at beamline ID32, which was in use until 2009. The angle of incidence of the X-rays was almost parallel to the surface normal (normal incidence), the analyzer was placed at 45° relative to the incident beam. A QCM was installed to monitor the evaporation rate of the Knudsen cell, and a LEED could be used to check for crystallinity of the metal substrates (picture adapted from Ref. [13]).

Table 4.1: Non-dipole parameters for the C 1*s*, N 1*s*, and O 1*s* orbitals. S_R was determined also experimentally [13], Ψ and $|S_I|$ were calculated.

	Cu(111)			Ag(111)	
	C 1*s*	N 1*s*	O 1*s*	C 1*s*	O 1*s*
S_R (exp.)	1.85	1.77	1.72	1.89	1.89
S_R (theo.)	1.742	1.708			
$\|S_I\|$	1.43	1.388	1.36	1.45	1.45
Ψ	-0.055	-0.067	-0.075	-0.066	-0.093

determined experimentally for atoms that are common in organic compounds [13, 52, 59]. A description of the experiment to determine the S_R parameter is given in Section 2.2.5. The non-dipole parameter Ψ can be calculated [60]. The description of the experiment to measure Ψ is given in Section 4.1.3. In case the XSW experiments are done in the normal incidence geometry (Θ_{Bragg} close to 90°), S_I is not independent, but can be determined using S_R and Ψ (see Equation 2.43). Table 4.1 lists the non-dipole parameter, which were used for the XSW analysis of H2Pc, PYT, and COHON on Cu(111), respectively, as well as for PYT on Ag(111).

4.1.2 XSW setup at the ESRF starting in 2010

The new XSW setup at the ESRF beamline ID32 [44] was in use since 2010. A schematic picture of the end station with the relevant items is supplied in Figure 4.2. The setup contained two vacuum chambers plus a load lock, which could all be isolated by gate valves. An Omicron transfer system with two transfer rods enabled the transfer between load lock and preparation chamber, and between preparation chamber and main chamber.

The preparation chamber was pumped by a turbo pump and an ion getter pump, which resulted in typical base pressures of $\sim 8.0 \times 10^{-10}$ mbar. A home-made Knudsen cell (for details see Section 4.3) was attached to the preparation chamber. Permanent equipment of the preparation chamber was a QCM, installations for Ar^+ sputtering, a temperature-controlled sample stage, and a LEED.

The analysis chamber was pumped by a combination of turbo and ion getter pump. The base pressure was at $\sim 4.0 \times 10^{-10}$ mbar. The anlysis chamber, in which the XSW measurements were performed, was equipped with a sample manipulator and a hemispherical SPECS PHOIBOS 225 HV photoelectron analyzer. The chosen analyzer slits resulted in an acceptance angle of ±7.5°. The detection angle of the analyzer was at 90° relative to the incident X-ray beam. For XSW experiments the sample was slightly rotated by ca. 2° toward the analyzer. This scenario is visible in Figure 4.2. Due to this configuration non-dipole contributions to the photoelectron yield can be effectively avoided [58]. In the following section XSW results are presented of an experiment that examines the validity of the dipole approximations for this experimental setup.

4.1.3 Influence of the new XSW setup on the non-dipole parameter S_R

At a photoelectron detection angle close to 90° relative to the surface normal, the photoelectron yield are supposed to be almost the same for the dipole and quadrupole approximation. Exactly the same yield for both approximations is expected for exactly 90°, as described in Section 2.11. Here we give experimental evidence to theory and determine the non-dipole parameter S_R (see 2.2.5) for the new XSW setup. A multilayer film of molecules containing carbon and oxygen atoms was prepared on Cu(111). For fitting of the yield curves, the coherent fraction was set to 0. This is justified by the assumption that for thick films the atoms adsorb at random distances with respect to the nodes of the

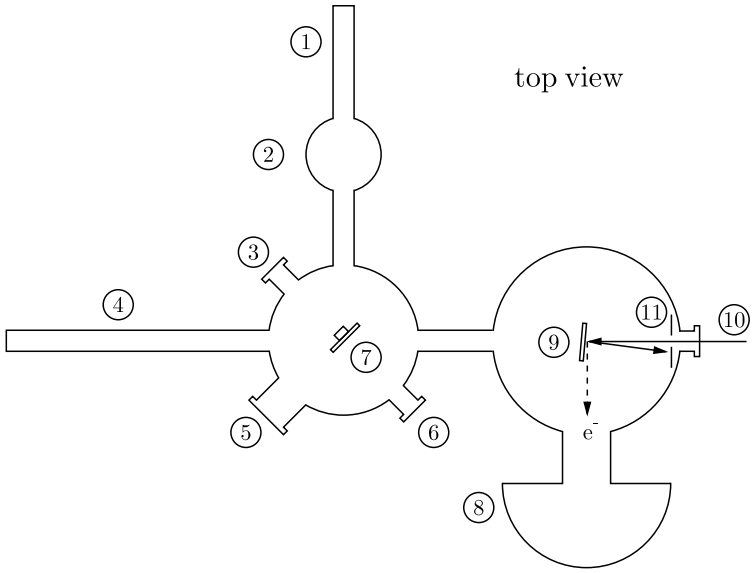

(1)	Transfer rod (load lock ↔ preparation chamber)	(7)	Manipulator (QMC at its backside)
(2)	Load lock	(8)	Hemispherical analyzer
(3)	Knudsen cell	(9)	Manipulator
(4)	Transfer rod (preparation chamber ↔ analysis chamber)	(10)	Incoming X-ray beam
(5)	LEED	(11)	Reflectivity screen
(6)	Installation for Ar^+ sputtering		

Figure 4.2: Schematic and simplified top view picture of the UHV experimental setup (starting in 2010) at the ESRF beamline ID32, displayed for "normal-incidence" conditions. In fact, the angle deviates by a few degrees from 90° in order to be able to detect the reflected X-ray beam. The photoelectron analyzer is mounted at 90° relative to the incident beam. Not drawn are the valves between the three chamber parts (load lock, preparation chamber, and analysis chamber) and the pumping units of the chambers.

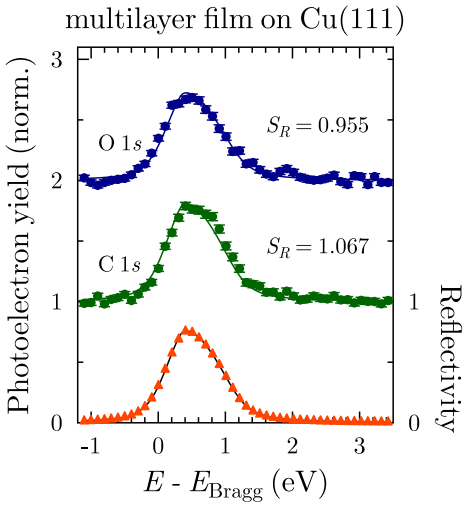

Figure 4.3: Experimental determination of the non-dipole parameter S_R. A multilayer film of COMs made of carbon and oxygen atoms was prepared on Cu(111). The fit parameter here was S_R, while f_H was set to 0. The coherent position does not play any role if $f_H = 0$.

XSW field. This scenario is depicted in Figure 2.10(f). The equation for the photoelectron yield has now the simple form

$$Y = 1 + S_R R. \tag{4.1}$$

The photoelectron yield and reflectivity can be determined experimentally, and S_R is the fitting parameter.

The result is shown in Figure 4.3 for the carbon and oxygen atoms. We obtain for the carbon atoms $S_R = 1.067 \pm 0.021$ and for the oxygen atoms $S_R = 0.955 \pm 0.020$. The error given here is related to the uncertainty of the fit curve to the experimental data.

Both values are close to the case of the dipole approximation, where $S_R = 1.000$. An $S_R < 1$, which is the case for the oxygen atoms, can not be explained by the considered theory except for detection angles $> 90°$ relative to the surface normal. Yet, it is impossible to detect photoelectrons at such angles, as they can not penetrate the substrate. This indicates that the small deviations from unity emerge from our data analysis rather than from the description of the photoemission process. However, the deviations are small and without committing a significant error, the dipole approximation can be used for the normal incidence XSW analysis, in case the electron analyzer is placed at 90° relative to the incident beam.

Concerning future work, the XSW technique can be used to determine the second independent non-dipole parameter, Ψ. To obtain Ψ experimentally, the following procedure has to be run through: First, an XSW scan has to be done at 90° photoelectron emission angle with respect to the direction of the X-rays. At this electron emission angle the dipole approximation is valid and accurate values for f_H and P_H are obtained. In a second step a different photoemission detection angle has to be realized, which can be done if the electron analyzer is rotated or enables angular resolved measurements. The analysis for a second

XSW scan of the same sample has to be performed, now using the following equation for the photoelectron yield (see Section 2.2.5):

$$Y_{\mathrm{P}} = 1 + S_R \cdot R + \sqrt{R}|S_I| f_H \cdot \cos(\nu - 2\pi P_H + \Psi) \tag{4.2}$$

With the values of f_H and P_H, which were determined before, and the relation between $|S_I|$ and Ψ for the normal incidence XSW geometry, $|S_I| = \frac{1}{2}(S_R + 1)\sqrt{1 + \tan^2 \Psi}$, the non-dipole parameter Ψ can now be varied to fit the theoretical curve the experimental photoelectron yield.

4.2 XSW setup at the Diamond Light Source

The setup at the beamline I09 at the Diamond Light Source (DLS) near Didcot (UK) was not in the final state, when our experiments took place. The following description represents the conditions during the experiment.

The beamline I09 features currently a soft and a hard X-ray branch, which are guided separately from the storage ring to the end station, where they match on the same spot of the sample. A sketch of the beamline for hard X-rays is shown in Figure 4.4. The energy of the hard X-ray branch can be tuned from 2.1 keV $\leq \hbar\omega \leq$ 18 keV. For the hard X-ray measurements, the energy of the undulator radiation was selected by a Si(111) double-crystal monochromator. The overall energy resolution was about 350 meV for the photon energies we worked at, dominated by the resolution of the Si monochromator. The X-ray beam at the sample was defocused to a size of approximately 300 $\times$ 300 μm^2.

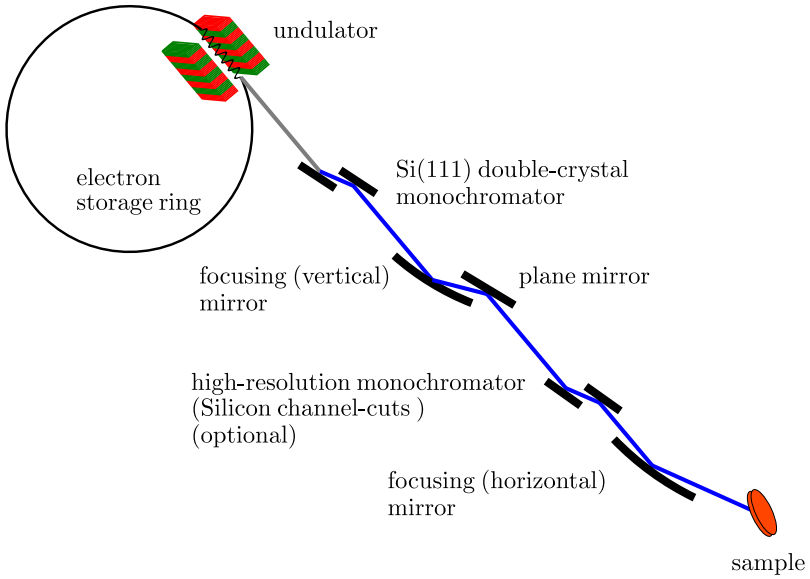

Figure 4.4: Schematic and simplified picture of the hard X-ray branch at beamline I09.

The end station in the experimental hutch 2 at I09 contains a load lock, a preparation chamber and an analysis chamber. Each of them can be isolated by gate valves. A sketch

of the setup is displayed in Figure 4.5. A five axis (x, y, and z translations and polar and azimuth rotations) manipulator is used for surface preparation in the preparation chamber and for X-ray measurements in the analysis chamber. It is equipped with a sample heater capable of electron beam and resistive heating and a cooling system, which was operated with liquid nitrogen for the LT measurements.

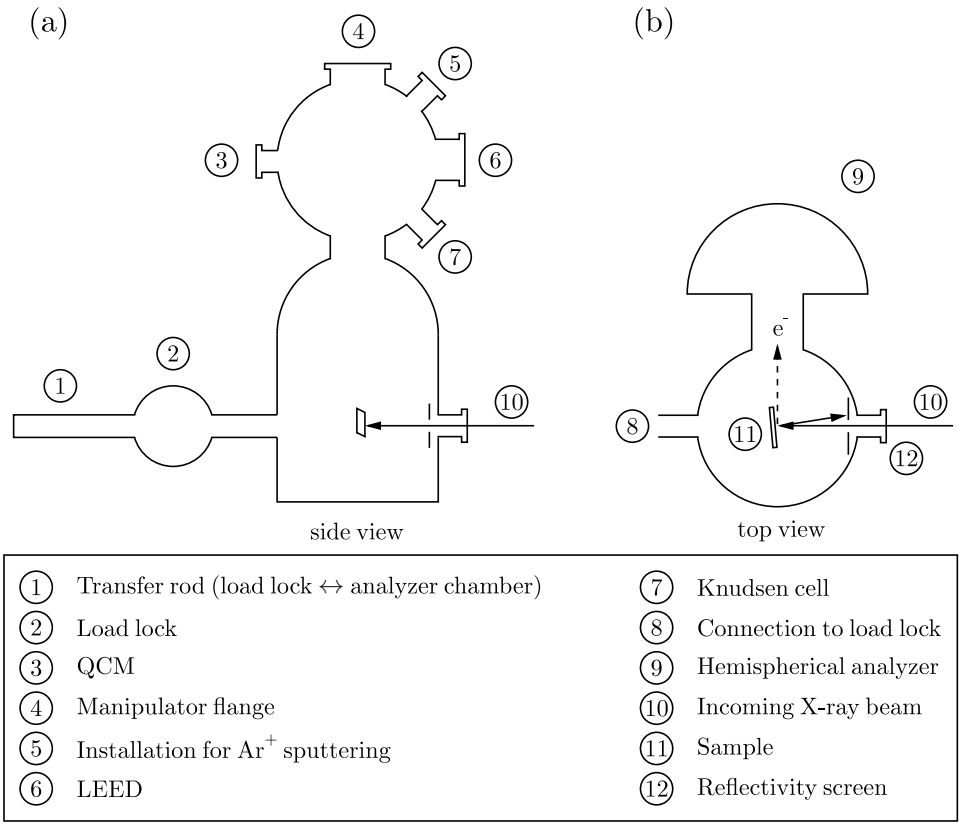

Figure 4.5: Schematic and simplified top view picture of the setup in experimental hutch 2 at the DLS beamline I09. Not drawn are the pumping units of the chambers and the valves between the load lock, preparation and analysis chamber.

The preparation chamber features an ion gun for Ar^+ sputtering, evaporator ports, a QCM on a linear translation, and a LEED system. The analysis chamber (base pressure 3×10^{-10} mbar) contains a VG Scienta EW4000 HAXPES hemispherical electron analyzer, which is mounted at $\sim 90°$ relative to the incident X-ray beam. The acceptance angle of the electron analyzer is $\pm 30°$. The intensity of the Bragg-reflected X-ray beam is monitored by measuring the light intensity of the reflected beam spot on a fluorescence screen using a CCD camera.

4.3 Knudsen effusion cell

The samples presented in this work were prepared by organic molecular beam deposition (OMBD) using a home-built triple Knudsen effusion cell. A schematic picture of this evaporator can be found in Figure 4.6. Mounted on a CF-38 flange, three individual quartz

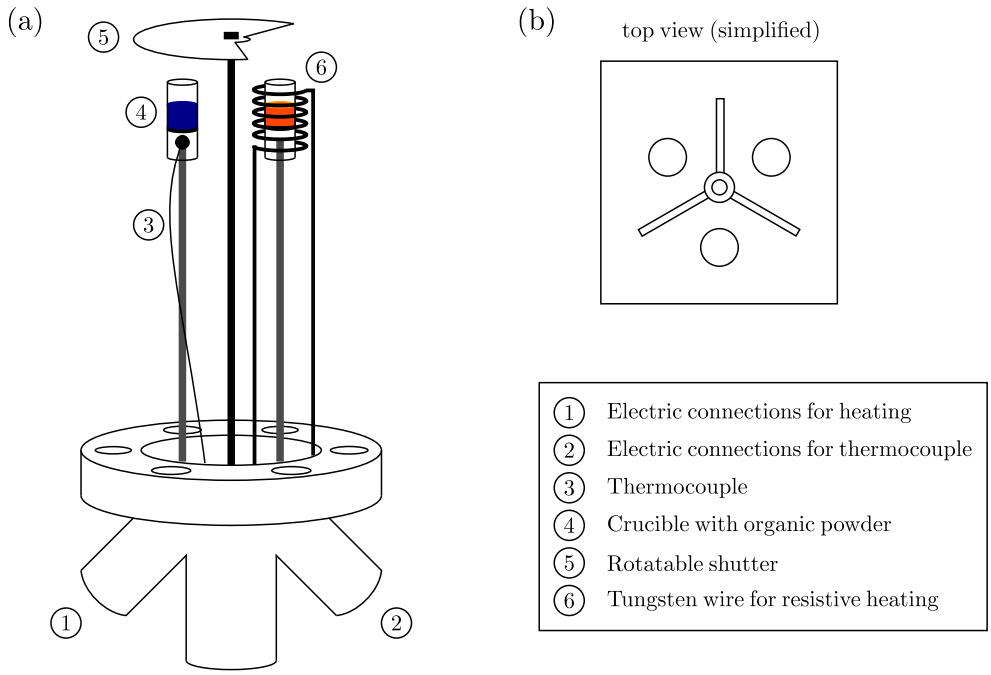

Figure 4.6: Schematic and simplified picture of the Knudsen cell, which was used for OMBD. (a) Side view: For clarity only two of three crucibles are displayed, the heating wire and thermocouple is drawn in only once, and the thermal shielding between the crucibles is omitted. In reality each crucible has its own thermocouple and heating wire. (b) Top view without shutter, only the three crucibles and the shielding are displayed.

crucibles can be filled with different organic compounds. The crucibles have a cylindrical shape with the length of ~ 15 mm and a diameter of ~ 3 mm. Each crucible is temperature-controlled via a K-type thermocouple and a tungsten wire for resistive heating. A double plated shielding between the individual crucibles reduces the temperature transfer from the intentionally heated crucible to the neighbouring ones. For simultaneous installation of more than one organic compound this shielding permits an increased difference of the sublimation temperature of the molecules. For instance, heating one crucible up to 500 K leads to ~ 360 K in the adjacent crucibles. Above the crucibles a rotatable metal disc with a cut-out of $\sim 120^\circ$ served as shutter.

4.4 Data acquisition and analysis

An XSW scan contained the following measurements: For each of the 30–60 photon energies around the Bragg energy of the single crystal, an XP spectrum of the core-level of interest, e.g. C 1*s* or N 1*s*, was acquired. A typical spectrum is shown in Figure 4.7. This

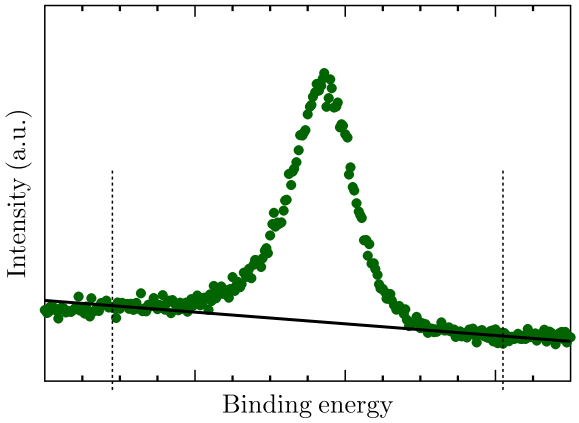

Figure 4.7: Usual raw XP spectrum. To determine the photoelectron yield of the core-level signal, an appropriate range of the spectrum was chosen (dashed line) and a linear background (solid line) was subtracted. The yield corresponds to the area between data points and background slope within the selected range.

figure also displays the subtraction of a linear background that was applied to each XP spectrum. In Section 5.5 a more sophisticated analysis was required and a Shirley-background was subtracted from the spectra. The photoelectron yield of a spectrum corresponds to the area of the background-subtracted XPS peak. The second necessary information was the intensity of the Bragg-reflected beam, $R(E_{\mathrm{photon}})$, which was measured for the same photon energies as the photoelectron yield.

The evaluation of the XSW data was performed using the software package `dare`, which was developed at the ESRF. At first, the data of the reflectivity curve was fitted. In a second step, the file containing the photoelectron yield, $Y_{\mathrm{p}}(E_{\mathrm{photon}})$, was fitted to the theoretical photoelectron yield curve (see Equation 2.41). In case the experimental setup required the use non-dipole parameters, the corresponding values for S_R, S_I and Ψ had to be entered prior to fitting. The values used in this work are listed in Table 4.1. The fitting result of each XSW measurement comprised the coherent fraction f_H and coherent position P_H. The latter determines the average bonding distance of the atom that is related to the analyzed core-level.

Chapter 5

Results and Discussion

In this chapter, XPS and XSW results of COMs on Cu(111), Ag(111), and/or Au(111) surfaces are presented. The organic compounds were selected to gain insight into fundamental adsorption processes. In particular, this work explores how the bonding distance can depend on:

- The substrate (Section 5.1)
- The coverage (Section 5.4)
- The temperature (Sections 5.3 and 5.9)
- Molecular modifications due to different side groups (Sections 5.6 and 5.7) and central metal ion (Sections 5.8 and 5.9)

Additionally, the question of the adsorption geometry and orientation of a non-planar molecule (Section 5.10) and of a bilayer system, consisting of two different molecules – one on top of the other – is addressed (Section 5.5).

5.1 DIP on Cu(111), Ag(111), and Au(111)

Parts of this section have been published in Ref. [61], Figures and Tables are reprinted (adapted). Copyright (2013) by the American Physical Society.

5.1.1 Introduction

The reliable prediction of the equilibrium structure and energetics of hybrid inorganic/organic systems from first principles represents a great challenge for theoretical methods due to the interplay of covalent interactions, electron transfer processes, Pauli repulsion, and van der Waals (vdW) interactions. During recent years, huge efforts have been made to incorporate vdW interactions into density functional theory (DFT) calculations in order to determine the structure and stability of π-conjugated organic molecules on solid surfaces [23, 62–66]. Understanding these interface properties is relevant, *inter alia*, for electron transfer processes in organic devices. Until now and despite the obvious benefit, there are only few studies of metal-organic interfaces combining theory and experiment. Here, X-ray standing wave (XSW) measurements can provide an important test for DFT calculations [28, 63]. This is particularly important for systems with strong vdW contributions to the overall bonding, for which no simple substrate dependence is expected.

As model system we chose diindenoperylene (DIP, $C_{32}H_{16}$, molecular structure is inset in Figure 5.1), a π-conjugated organic semiconductor with excellent optoelectronic device performance, which has been studied over the last decade both in thin-films [67–70] and in monolayers on noble metal surfaces [71–73]. With respect to its chemical structure, DIP is a relatively simple, planar hydrocarbon without heteroatoms. In contrast to the intensely studied perylene derivative 3,4,9,10-perylene tetracarboxylic dianhydride (PTCDA, $C_{32}H_8O_6$) [12, 13, 15, 74, 75] with its four carbonyl groups, the DIP–substrate interaction is not complicated by polar side groups, and the influence of intermolecular interactions is expected to be smaller than for PTCDA [76].

5.1.2 XPS measurements of DIP on Cu(111), Ag(111), and Au(111)

The C 1*s* core-level signals of DIP on Cu(111), Ag(111), and Au(111), which were used for the XSW measurements, are shown in Fig. 5.1. The main peaks are expected to consist of two principal components (C–C vs C–H bound atoms) which, however, could not be resolved with the energy resolution of the XSW setup.

In addition to each main peak, a second weak feature at ∼1 eV higher binding energy possibly related to a shake-up process can be observed. The binding energy of the C 1*s* main line of DIP follows $E_B^{Ag} > E_B^{Cu} > E_B^{Au}$, being 284.5 eV on Ag(111), 284.2 eV on Cu(111), and 283.7 eV on Au(111). Furthermore, the C 1*s* peak of DIP on Ag(111) exhibits a stronger asymmetry than on Cu(111) and Au(111). This may be related to the creation of electron-hole-pairs close to the Fermi level caused by the higher density of states near the Fermi edge of DIP adsorbed on Ag(111) (Refs. [77] and [78]).

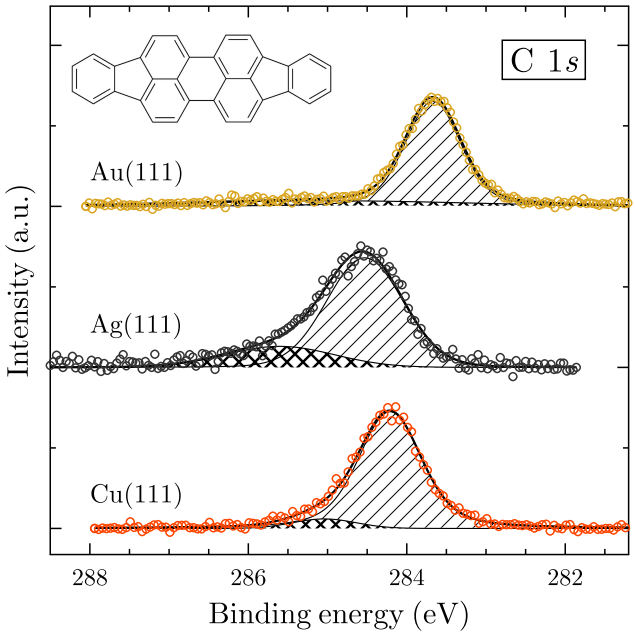

Figure 5.1: C 1*s* core-level shift observed for a submonolayer of DIP (inset) on Cu(111), Ag(111), and Au(111). The spectra were taken at an emission angle of 45° with the XSW setup at ID32. From each signal a Shirley background was subtracted and then fitted with a Voigt function for the main peak and a Gaussian function for possible shake-up peaks.

5.1.3 XSW measurements of DIP on Cu(111), Ag(111), and Au(111)

Representative results of the XSW experiments are shown in Fig. 5.2. In each diagram the measured reflectivity of the substrate and the corresponding C 1*s* photoelectron yield is displayed. Least-squares fits of the data give the coherent position P_H and hence the average bonding distance $d_H = d_0(1 + P_H)$ [39], where d_0 is the substrate lattice plane spacing. Based on results of all XSW experiments we calculate the average bonding distance d_H and the standard deviation; see Fig. 5.3. For Cu(111) we thus find (2.51 ± 0.03) Å, and for Ag(111) (3.01 ± 0.04) Å. Due to the reconstruction of the Au(111) surface, which results in a 3% larger spacing between the first and second Au layers [74], the bonding distance decreases from the measured apparent value (3.17 ± 0.03) Å to (3.10 ± 0.03) Å. All experimental results are summarized in Table 5.1. The distribution of the individual XSW scans is visualized in Figure 5.3 using the Argand diagram. Each marker represents a single XSW measurement, whose position is given by the XSW fit result. f_H determines the length of the vector and P_H the angle of the vector pointing to the corresponding marker. Although the coverage of the two (three) DIP films prepared on each substrate was not identical, we did not observe a significantly coverage-dependent bonding distance d_H.

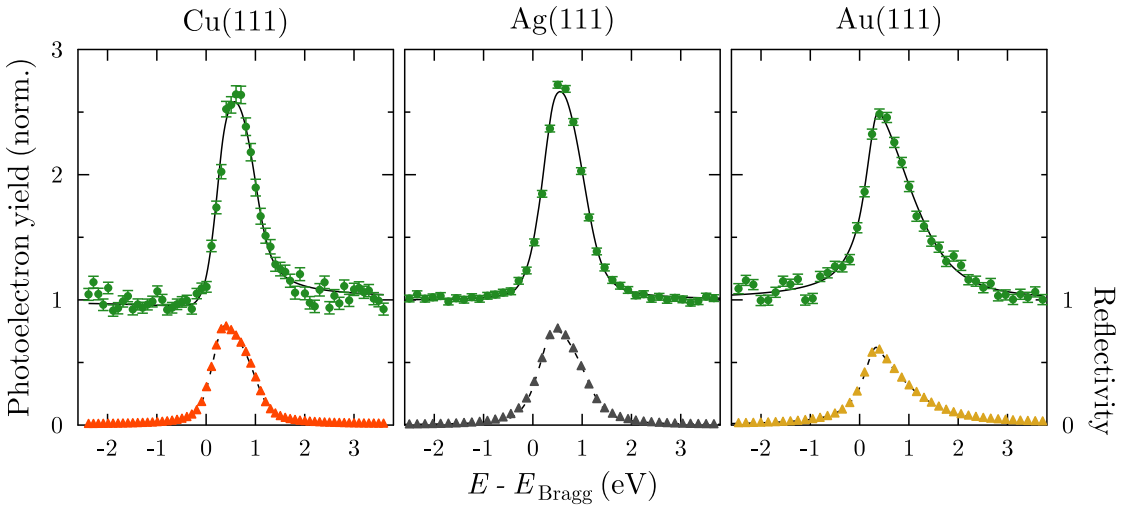

Figure 5.2: Reflectivity (triangles) and photoelectron yield (circles) of the DIP C 1*s* signal on Cu(111), Ag(111), and Au(111). Each photoelectron yield curve corresponds to a least square fit of a single XSW scan revealing the coherent fraction f_H and coherent position P_H. Bragg energies are $E_{\mathrm{Bragg}} = 2.97$ keV [Cu(111)] and $E_{\mathrm{Bragg}} = 2.63$ keV [Ag(111) and Au(111)].

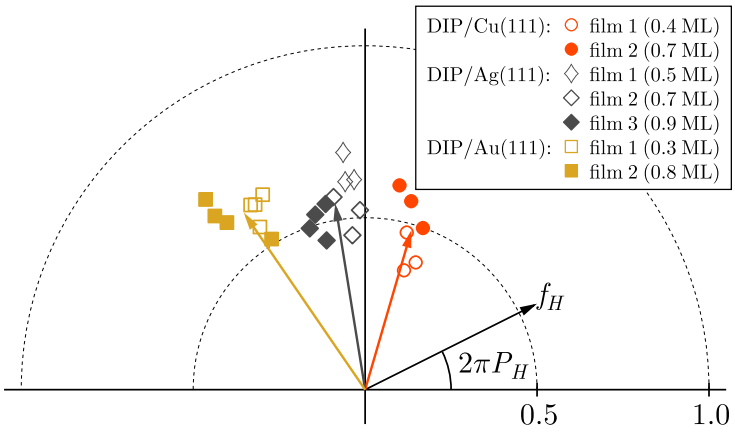

Figure 5.3: All XSW results for DIP on Cu(111) [circles], Ag(111) [diamonds], and Au(111) [squares] displayed in an Argand diagram. Here, each marker represents one single XSW measurement yielding f_H (length of a vector) and P_H (angle of a vector). The three vectors point to the average values of f_H and P_H for DIP on Cu(111), Ag(111), and Au(111). Film 1 of DIP on Ag(111) was measured with a different crystal compared to films 2 and 3.

Table 5.1: Result of XSW experiments: Coherent fraction f_H, coherent position P_H, and bonding distance d_H of DIP on the three noble metals. The parameters refer to an average of several XSW measurements with the corresponding standard deviation as error bars.

	f_H	P_H	d_H
Cu(111)	0.48 ± 0.09	0.20 ± 0.01	(2.51 ± 0.03) Å
Ag(111)	0.55 ± 0.08	0.28 ± 0.02	(3.01 ± 0.04) Å
Au(111)	0.62 ± 0.06	0.35 ± 0.01	(3.17 ± 0.03) Å[1]

5.1.4 Higher-order XSW measurements of DIP on Cu(111)

DIP on Cu(111) was investigated with XSW at the second order Bragg energy, $E_{\text{Bragg}} = 5.94$ keV. The analysis revealed results, which are very similar to our results from Section 5.1.3. The coherent fraction is $f_H = 0.50$ and the coherent position $P_H = 0.35$. As

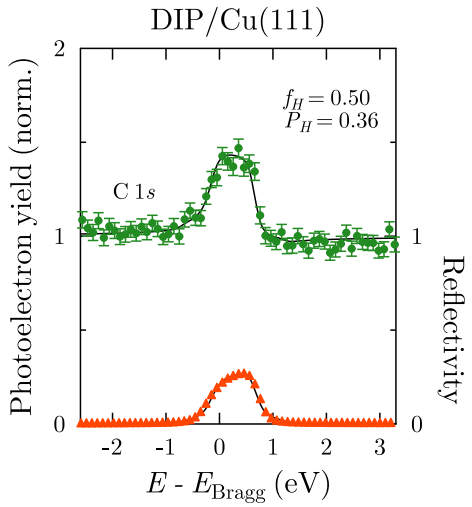

Figure 5.4: Reflectivity (triangles) and photoelectron yield (circles) of the DIP C 1s signal on Cu(111) for the second-order Bragg reflection around $E_{\text{Bragg}} = 5.94$ keV. The photoelectron yield curve corresponds to a least square fit of a single XSW scan revealing the coherent fraction f_H and coherent position P_H.

the second order Bragg reflection generates a standing wave field, whose periodicity is half of the one from the first order Bragg reflection, the corresponding lattice spacing is $d_{222} = 1.043$ Å. With $n = 2$, we get a bonding distance of $d_H = (n+P_H)d_{222} = 2.45$ Å, only 0.06 Å less than the result obtained using the first-order Bragg reflection. The different shape of the reflectivity curve compared to one obtained at the first-order Bragg reflection is related to the smaller width of the Cu(222) reflection. Before hitting the sample, the X-rays pass a monochromator, which is a Si(111) crystal. The width of the Si(111) reflection is broader than the Cu(222) reflection. The measured reflectivity is a convolution of both reflections, which has in our case the shape of the Si(111) reflection.

5.1.5 DFT calculations of DIP on Cu(111), Ag(111), and Au(111)

To obtain further insight in the adsorption of DIP on Cu(111), Ag(111) and Au(111), a collaboration with theoreticians was set in. Their results are presented in this paragraph.

Table 5.2: Adsorption energy E_{ads} of the relaxed structures, vdW$^{\mathrm{surf}}$ binding energy E_{vdW} as derived from data shown in Fig. 5.5(c), and distances d between the topmost layer of the metal and the carbon backbone of DIP. $d_{\mathrm{min/max}}$ refer to the lowest/highest bonding distance of a carbon atom within a DIP molecule.

	E_{ads}	E_{vdW}	d	d_{min}	d_{max}
Cu(111)	-4.74	-5.28 eV	2.59 Å	2.38 Å	2.79 Å
Ag(111)	-3.55	-4.56 eV	2.94 Å	2.89 Å	3.01 Å
Au(111)	-2.53	-3.06 eV	3.22 Å	3.15 Å	3.29 Å

Having established precise experimental data, we now turn to the results of our DFT calculations. The average bonding distances of DIP obtained from fully relaxed structures are $d = 2.59$ Å on Cu(111), $d = 2.94$ Å on Ag(111), and $d = 3.22$ Å on Au(111), see Table 5.2 and Fig. 5.5(c). We hence find that the PBE+vdW$^{\mathrm{surf}}$ method applied to DIP on Cu(111), Ag(111), and Au(111) yields an agreement better than 0.1 Å between theoretical calculations and experiments. In accordance with the bonding distances, the calculated adsorption energies listed in Table 5.2 follow the trend $|E_{\mathrm{ads}}(\mathrm{Cu})| > |E_{\mathrm{ads}}(\mathrm{Ag})| > |E_{\mathrm{ads}}(\mathrm{Au})|$. Interestingly, Fig. 5.5(c) shows that on Cu(111) the Pauli repulsion sets in rather weakly (a less steep $E_{\mathrm{ads}}(d)$ for small distances) compared to Ag(111) and Au(111), which is due to significant interaction between DIP and Cu(111). One may speculate that the interaction mechanism includes hybridization between DIP and Cu states.

In addition to the adsorption energies and average bonding distances, Table 5.2 holds the minimal and maximal bonding distances $d_{\mathrm{min/max}}$ of individual carbon atoms in DIP. These values indicate that the molecule adsorbs in a slightly tilted or distorted geometry. For Cu(111), where the effect is most pronounced, the calculated bonding distances d_{min} and d_{max} differ by ∼0.4 Å, which is equivalent to a molecular tilt angle of 1.5°. The corresponding spread of vertical positions of the carbon atoms leads to a reduced f_H in the XSW scans. Model simulations similar to those presented in Ref. [79] show that the DFT-derived adsorption geometry on Cu(111) results in a relatively small decrease of the coherent fraction ($\Delta f_H = -0.07$), which lies within the standard deviation of our XSW measurements.

To obtain a better understanding of the influence of lateral intermolecular interactions on the DIP adsorption geometry, we also computed the relaxed DIP geometry for different Cu(111), Ag(111), and Au(111) unit cells. For DIP on Cu(111), we increased the unit cell from (7×7) to (9×7) in order to reduce the molecule–molecule interactions. We studied various configurations, finding a flat relaxed geometry for each case considered. The bonding distance is slightly larger (2.64 Å) than for the calculation with the smaller

unit cell. For DIP on Ag(111), we also considered a unit cell which was determined from a closed packed monolayer on Ag(111) [72]. The relaxed geometry of the molecules in the monolayer is flat and the bonding distance $d = 2.99$ Å in almost perfect agreement with the experimental one, i.e., even better than the result for Ag(111) shown in Table 5.2. For a (9×5) unit cell of Au(111), the relaxed DIP geometry yields an equilibrium distance of 3.15 Å, also in slightly better agreement with experiment than the result shown in Table 5.2. Overall, these calculations agree with the experimental observation that the vertical DIP position depends only weakly on surface coverage.

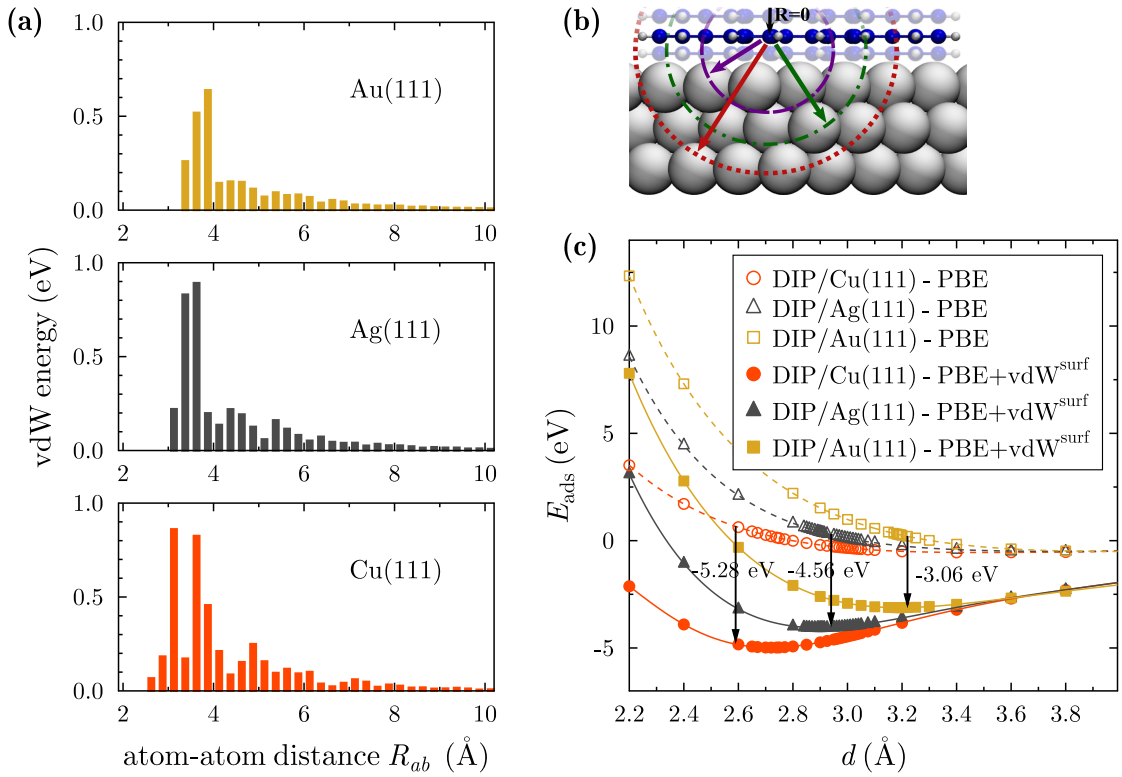

Figure 5.5: Results of the calculation of DIP on Cu(111), Ag(111), and Au(111). (a) The vdW energy as a function of the distance between adsorbate and substrate atoms, as illustrated in (b). (c) Adsorption energy E_{ads} for the unrelaxed DIP molecule as a function of its averaged distance d from the Cu(111), Ag(111), and Au(111) surfaces. The curves are shown for the PBE functional with (filled markers/solid line) and without (open markers/dashed line) the inclusion of long-range vdW interactions using the vdW^{surf} method. The reported contribution of the vdW energy is shown at the equilibrium distance corresponding to the fully relaxed DIP–surface geometry (see text).

5.1.6 Discussion

With the experimental and theoretical values at hand, and in view of their excellent agreement, we are in a good position to discuss the vdW interactions and the bonding distances in more detail. The (atom-atom) vdW energy is computed as $C_6^{ab} R_{ab}^{-6}$, where

the C_6^{ab} coefficient determines the strength of the interaction between atoms a and b, while R_{ab} is the distance between adsorbate and substrate atoms (Fig. 5.5(b)). Integrating the vdW energy for a single atom adsorbed on a semi-infinite surface yields the atom-surface vdW energy as [80, 81] $C_3^{\mathrm{A-S}}(z - z_0)^{-3}$, where now $C_3^{\mathrm{A-S}}$ determines the interaction strength between atom and surface, z corresponds to the distance of the atom to the uppermost surface layer, and z_0 indicates the position of the surface image plane. In a rather naive picture, the $C_3^{\mathrm{A-S}}$ coefficient can be determined simply from the C_6^{aa} and the C_6^{bb} coefficients that correspond to the adsorbed atom and the metal atom, respectively. However, the situation for real surfaces is more complex because both localized and bulk metal electrons contribute to the $C_3^{\mathrm{A-S}}$ coefficient in a non-trivial way, meaning that this coefficient depends on the dielectric function of the underlying solid. We computed the $C_3^{\mathrm{A-S}}$ coefficients (in units of Hartree·Bohr^3) corresponding to the interaction between a carbon atom and the Cu(111), Ag(111), and Au(111) surfaces. When describing the metal surface as a simple collection of non-interacting atoms we obtain $C_3^{\mathrm{C-Cu}} = 0.68$, $C_3^{\mathrm{C-Ag}} = 0.55$, and $C_3^{\mathrm{C-Au}} = 0.50$ Hartree·Bohr^3. In contrast, when using the more appropriate Lifshitz-Zaremba-Kohn (LZK) expression [82, 83] for $C_3^{\mathrm{A-S}}$, we obtain $C_3^{\mathrm{C-Cu}} = 0.35$, $C_3^{\mathrm{C-Ag}} = 0.35$, and $C_3^{\mathrm{C-Au}} = 0.33$ Hartree·Bohr^3. This clearly illustrates that the vdW interaction between an atom and a solid surface is significantly modified by the collective electronic response within the substrate surface [28, 80, 81]. The very similar LZK C_3 coefficients for Cu, Ag, and Au lead to essentially the same adsorption energy at large distances for DIP on Cu(111), Ag(111), and Au(111) (Fig. 5.5(c)). However, at shorter molecule-surface distances, which include the equilibrium distance, the adsorption energy is determined by an interplay between the vdW attraction and the Pauli repulsion with a possible covalent component. The Pauli repulsion follows roughly the trend of decreasing vdW radii, with a faster onset in terms of the molecule-surface distance for Au (the largest vdW radius), and then decreases for Ag and Cu. Therefore, for Au the balance between vdW attraction and the Pauli repulsion is obtained *further away* from the substrate (i.e. larger adsorption distances) than for Cu, which in turn makes the adsorption energies *lower* for Au than for Cu, in contrast to the possible naive expectation of Au with its higher polarizability and C_6 coefficient exhibiting stronger vdW interaction than Cu.

The difference in the vdW energy distribution for DIP on Cu(111), Ag(111), and Au(111) is visualized in Fig. 5.5(a), where the vdW energy between DIP and substrate atoms is plotted as a function of their distance R_{ab}. In contrast to Ag(111) and Au(111), the small bonding distance of DIP on Cu(111) results in a second peak in the histogram at ∼3.6 Å, which originates from the higher atomic density of the copper substrate.

5.2 P4O on Au(111)

5.2.1 Introduction

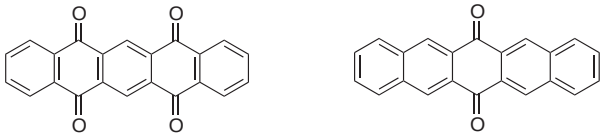

Figure 5.6: Molecular structure of P4O (left) and P2O (right). The latter was not investigated on Au(111) by XSW, however, the structure is given here for a better understanding when comparing to P4O.

The determination of the bonding distance of pentacene-5,7,12,14-tetraone ($C_{22}H_{10}O_4$, P4O, molecular structure shown in Figure 5.6) on Au(111) was part of a study to investigate systematically the adsorption behaviour of PEN-derivatives on metal surfaces, which was published in Ref. [84]. Before measuring P4O on Au(111), the XSW results of P4O and P2O on Cu(111) and Ag(111) were known. The multi-technique study also covered XPS and UPS measurements. The combination of PES and XSW experiments led to the conclusion that P2O is chemisorbed on Cu(111), indicated by a low bonding distance and charge transfer from metal to molecule. On Ag(111), the molecular bonding distance and XP spectra pointed toward a mainly physisorbed P2O molecule. P4O showed on Cu(111) qualitatively the same behavior as P2O. In contrast, P4O still was chemisorbed on Ag(111). PES measurements indicated a physisorbed P4O molecule on Au(111). This finding should be confirmed by XSW measurements, establishing further the correlation between PES and XSW results.

5.2.2 XPS measurements of P4O on Au(111)

The XP spectra of C 1*s* and O 1*s* are displayed in Figure 5.7. In the C 1*s* spectrum a second feature at the high BE side of the main peak is clearly visible, which originates from the carbonylic carbon atoms. Each of the four carbon atoms are bound to an oxygen atom. The spectrum was fitted using two Gaussian functions, with the main peak (C–C) at 284.0 eV and the side peak (C=O) at 286.6 eV. The ratio of the peak areas is $I(\mathrm{C-C})/I(\mathrm{C=O}) = 4.34$, deviating by only ∼5 % from the theoretical ratio of $18/4 = 4.5$.

5.2.3 XSW measurements of P4O on Au(111)

XSW measurements were performed both for the first order and the second order Bragg peak of the Au(111) substrate at 2.634 keV and 5.268 eV, respectively. The results of both experiments will be described now.

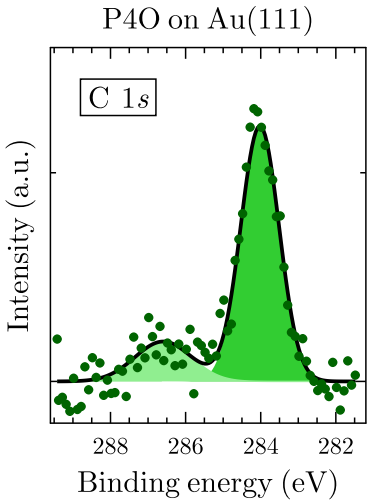

Figure 5.7: C 1*s* spectrum of P4O on Au(111). The low BE peak is related to the C–C-bonding carbons, the high BE peak to the C=O-bonding carbons.

First-order XSW measurements of P4O on Au(111)

Two films of P4O on Au(111) were prepared with a coverage of 1.0 ML. For each film, several XSW scans around the Bragg energy of the first-order Bragg reflection were taken. The average values (with the standard deviation as error) of the coherent fraction and coherent position is $f_H = (0.60 \pm 0.05)$ and $P_H = (0.42 \pm 0.005)$, respectively. Considering the 3% increase of the layer spacing between the first and the second layer of the Au(111) substrate due to surface reconstruction [74], the corresponding bonding distance is $d_H = (3.28 \pm 0.01)$ Å. Figure 5.8 shows a representative photoelectron yield curve of the C 1*s*

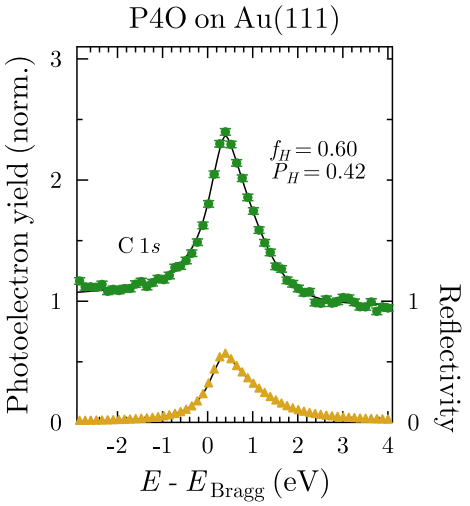

Figure 5.8: Reflectivity (triangles) and photoelectron yield curves (circles) of the carbon atoms of P4O on Au(111).

core-level. It is not possible to evaluate a O 1*s* XSW scan due to an Auger peak of the gold substrate, which crosses the O 1*s* peak during the first-order Bragg scan and thereby mixing up the O 1*s* peak intensities.

Second-order XSW measurements of P4O on Au(111)

One of the two films of P4O on Au(111) was also measured at the second-order Bragg energy of the Au(111) crystal. The average fitting results are $f_H = 0.34 \pm 0.06$ and $P_H = 0.79 \pm 0.01$. To calculate the bonding distance, the formula $d_H = (n + P_H)d_0$ has to be used with $n = 2$ and $d_0 = 1.178$ Å, resulting in a bonding distance of $d_H = 3.21$ Å, considering the surface reconstruction of Au(111). A typical photoelectron yield curve for a second-

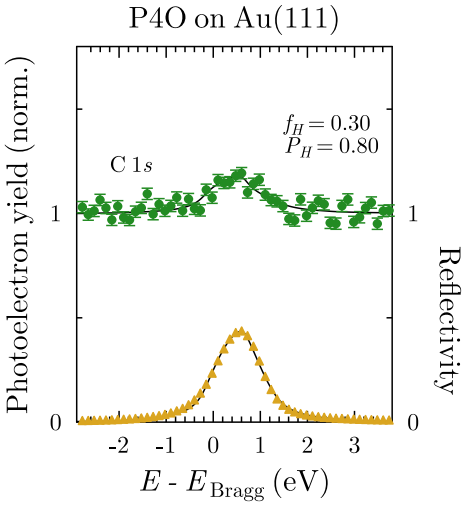

Figure 5.9: Reflectivity (triangles) and photoelectron yield curves (circles) of P4O on Au(111), measured at the (222)-Bragg energy (5.268 keV).

order XSW scan is displayed in Figure 5.9. As described in Section 5.1.4, the different shape of the reflectivity curve compared to the first-order reflectivity in Figure 5.8 originates here from the relatively broad energy distribution of the X-rays, which is determined by the Bragg reflection of the beamline monochromator made of Si(111), compared to the intrinsic width of the Au(222) Bragg reflection. The measured reflectivity curve is a convolution of both Bragg reflections.

5.2.4 Discussion

P4O adsorbs on Au(111) at a bonding distance, which was observed for other π-conjugated molecules on the Au(111) substrate. In those cases, the interaction between molecule and Au is dominated by weak dispersion forces. Similar bonding distances were found for the carbon backbone bonding distance of PTCDA on Au(111), being 3.27 Å [74]. For 1.0 ML CuPc at RT, the carbon bonding distance is 3.31 Å [85].

The bonding distance of the carbon atoms of P4O measured at the first-order and the second-order Bragg reflection are in good agreement and deviate by 3% only. On the other hand, the coherent fractions show a big difference. However, a lower coherent fraction for the higher-order XSW measurement might be explained: The periodicity of the XSW field is bisected for the second-order Bragg reflection compared to the first-order, and static disorder and the amplitude of vibrations of the molecule in relation to the spacing of the standing wave becomes larger. This is a possible reason for the lower coherent fractions observed for the second-order XSW measurement.

5.3 HBC on Au(111)

5.3.1 Introduction

Temperature dependent XSW experiments were performed for hexa-*peri*-hexabenzocoronene (HBC, $C_{42}H_{18}$, molecular structure shown in Figure 5.10(b)) on Au(111). This system was chosen to study the potential slope of the binding energy for HBC adsorbed on Au(111). A Lennard-Jones potential, which is commonly used to describe vdW interactions, is shown in Figure 5.10(a). With decreasing temperature the amplitude of the thermal vibrations of the molecule perpendicular to the Au(111) surface will decrease. Thermal vibrations along that axis follow the anharmonic shape of the potential of the binding energy. Therefore, a smaller amplitude of these vibrations should lead to a smaller average bonding distance of the molecule at low temperatures. This effect is the more pronounced the weaker the interaction potential is. For metal single crystals, previous results showed that a gold crystal is interacting weakly with a hydrocarbon [15, 86]. Two submonolayer films of HBC

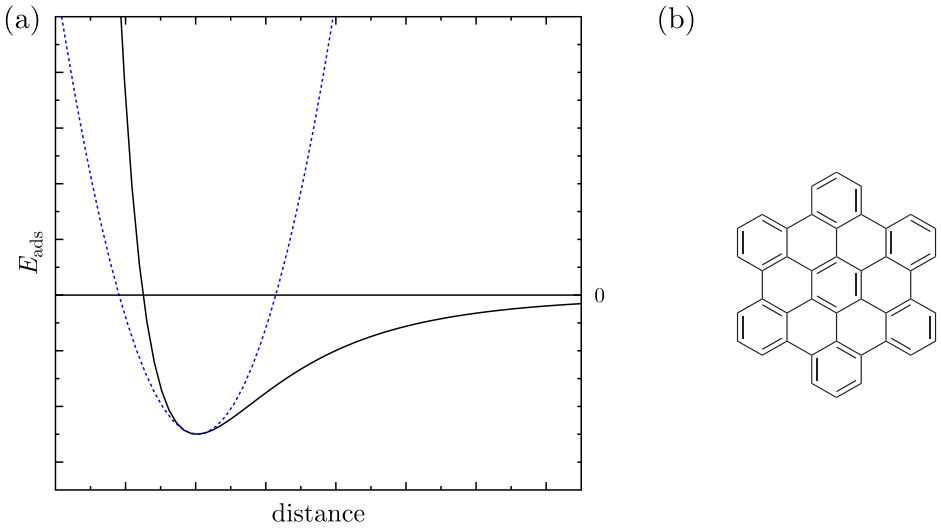

Figure 5.10: (a) Lennard-Jones potential (solid line), which represents vdW interactions. It can be approximated close to the minimum by a harmonic function (dotted line). (b) Molecular structure of HBC.

were prepared on Au(111) at RT *in situ* under UHV conditions by molecular beam epitaxy (0.2 ML and 0.3 ML). For HBC on Au(111), a repulsive behaviour between molecules was reported for coverages below 0.7 ML [87], which is an indication of intermolecular interaction. Hence, it is important for this experiment to prepare dilute films, where the intermolecular distance is large enough to ignore safely a possible influence of the coverage on the bonding distance.

5.3.2 Temperature determination using the Bragg energy

XPS and XSW measurements of HBC on Au(111) were done at RT (294 K) and upon cooling. Not only for that case, also other samples presented in this work were studied in view of temperature dependent bonding distance of molecules on a coinage metal surface. Therefore, at this place the method of temperature determination using the shift of Bragg energy will be explained exemplary for HBC on Au(111).

At RT (LT) we measured a Bragg energy of $E^{\mathrm{RT}}_{\mathrm{Bragg}} = 2.6342$ keV ($E^{\mathrm{LT}}_{\mathrm{Bragg}} = 2.6406$ keV). Using Bragg's law this rise of E_{Bragg}, for a fixed Bragg angle, can be related to a shrinking of the lattice spacing by $\Delta d = 5.72 \cdot 10^{-3}$ Å. Assuming a linear expansion coefficient at RT, $\alpha = 1.42 \cdot 10^{-5}$ 1/K [2], the temperature difference is

$$\Delta T = \frac{1}{\alpha} \frac{\Delta d}{d_0} = 171 \text{ K}, \tag{5.1}$$

where $d_0 = 2.353$ Å is the lattice spacing of Au(111) at RT. Hence, the LT value is 123 K. Note that, compared to the use of a thermocouple, this method is a very direct measurement of the substrate temperature. The error of the temperature arising from the determination of E_{Bragg} is 1.5 K. However, the larger uncertainty emerges from the linear expansion coefficient α. Actually, this value is not constant, but decreases slightly with temperature in the considered temperature range [88]. Therefore, the presented temperature has to be considered as an upper limit. We can refine the temperature determination assuming a linear decrease of $\alpha(T)$ with a gradient of $5 \cdot 10^{-9}$ $\frac{1}{\mathrm{K}^2}$. This slope is based on experimental values of α at 200 K and 300 K[89]. The final temperature is then 117 K. The uncertainty emerging from the error from the determination of E_{Bragg} and the slope of $\alpha(T)$ is estimated to be ±8 K.

5.3.3 Temperature-dependent XPS measurements of HBC on Au(111)

Figure 5.11 shows XP spectra of HBC on Au(111) at RT and LT. The analysis of the C 1s peak reveals a binding energy of $E^{\mathrm{RT}}_{\mathrm{B}} = 283.9$ eV at RT and $E^{\mathrm{LT}}_{\mathrm{B}} = 284.1$ eV at LT. Also the width of the peaks are similar ($FWHM = 1.0$ eV and $FWHM = 1.2$ eV, respectively). The spectra are displayed in Figure 5.11.

5.3.4 Temperature-dependent XSW measurements of HBC on Au(111)

A representative XSW photoelectron yield curve of C 1s at RT (open circle) and LT (filled circle) is shown in Figure 5.12. The average over individual results yielding the coherent fraction and coherent position for both temperatures are $f_H = 0.56 \pm 0.05$ and $P_H = 0.35 \pm 0.01$ at RT, and $f_H = 0.57 \pm 0.05$ and $P_H = 0.35 \pm 0.01$ at LT. The average XSW results are summarized in Tab. 5.3. The measured bonding distances are, considering

[2] The use of the bulk value α is justified here, because the penetration depth of the X-rays is in the order of µm, and the reflectivity signal is created from the bulk crystal.

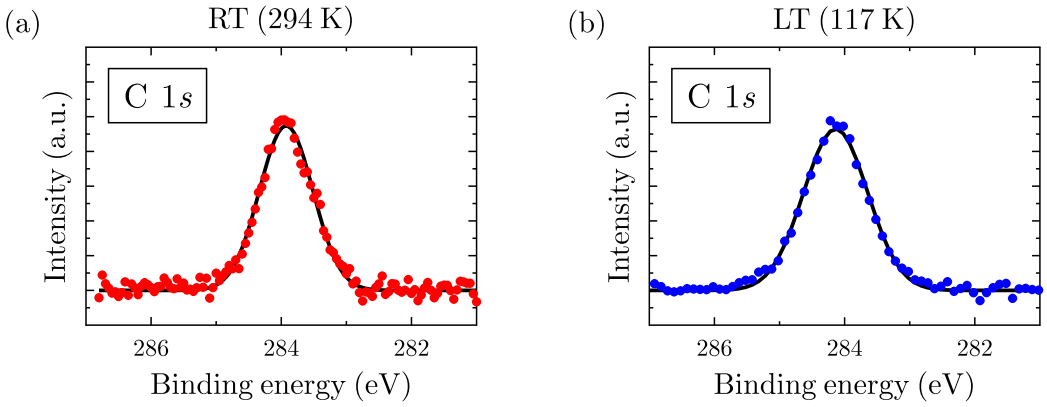

Figure 5.11: C 1*s* XP spectra of HBC on Au(111). (a) at RT (294 K) and (b) at LT (117 K).

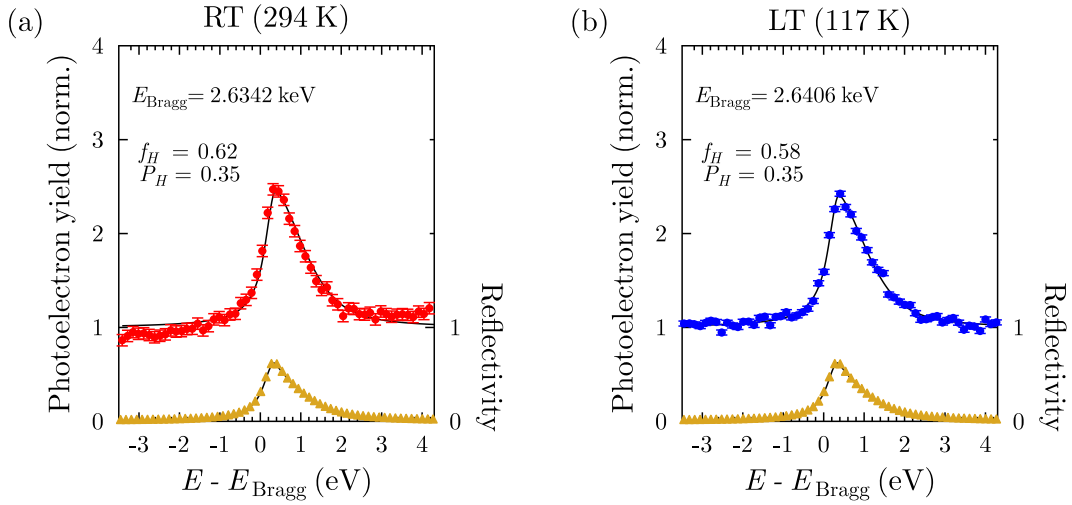

Figure 5.12: Representative photoelectron yield curves of HBC on Au(111) at RT and LT. Both figures display the yield as a function of deviation from E_{Bragg}. The thermal shrinking of the substrate lattice spacing upon cooling is related to an increase of E_{Bragg}, from $E^{\mathrm{RT}}_{\mathrm{Bragg}} = 2.6342$ keV at RT to $E^{\mathrm{LT}}_{\mathrm{Bragg}} = 2.6406$ keV at LT. The change of E_{Bragg} is exploited to determine the LT value. For details see main text.

Table 5.3: XSW results of HBC on Au(111) at RT and LT. The average over several XSW measurements is displayed.

Atom	T (°C)	f_H	P_H	d_H (Å)
C 1*s*	RT (294)	0.56	0.35	3.10 ± 0.03
C 1*s*	LT (117)	0.57	0.35	3.09 ± 0.03

the increased lattice spacing between the first and the second Au(111) layer due to surface reconstruction [74], $d_{RT} = 3.10 \pm 0.03$ Å and $d_{LT} = 3.09 \pm 0.03$ Å at RT and LT, respectively.

5.3.5 Discussion

The XSW results show that there is no difference of the bonding distance of HBC on Au(111) between RT and LT conditions within our error bars. The bonding distance of ∼3.1 Å both at RT and at LT is smaller than the sum of vdW radii of the carbon and gold atoms, which is 3.41 Å. Hence, the adsorption of HBC on Au(111) is not purely mediated by vdW interaction.

A consequence of this result for the study of the adsorption potential is that the decrease in vibrational amplitude at lower temperatures does not lead to a lower bonding distance. This fact gives rise to the assumption that, within the investigated temperature regime, the interaction potential of HBC on Au(111) can be approximated with a quadratic function around the equilibrium distance. To see a temperature dependent bonding distance it might be necessary to use either a different substrate, which interacts even more weakly with a molecule, and the slope of the interaction potential becomes less steep toward higher distances. The other possibility is to increase the temperature range, either by cooling further down or by measuring at elevated temperatures. The upper temperature limit is the desorption of the molecules, which occurs for a monolayer PEN on Au(111) at 516 K [90].

Comparing HBC with DIP (for details see Section 5.1) – another pure hydrocarbon – we see that both molecules adsorb on Au(111) at the same height, in contrast to PTCDA, P4O and CuPc on Au(111). For these molecules, larger bonding distances, namely 3.27 Å (PTCDA, [74]), 3.28 Å (P4O, Section 5.2), and 3.31 Å (CuPc, [86]) were reported. This difference is significant and probably due to the oxygen atoms (PTCDA, P4O) or other heteroatoms (CuPc).

5.4 PEN on Ag(111)

This section is reprinted (adapted) with permission from Ref. [91]. Copyright 2013, American Chemical Society. The publication emerged from a collaboration with the author of this work.

5.4.1 Introduction

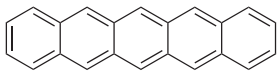

Figure 5.13: Molecular structure of PEN.

The adsorption strength of the pentacene (PEN, $C_{22}H_{14}$, molecular structure shown in Figure 5.13) on Ag(111) could not be determined unambiguously, although it was studied with several experimental techniques. While NEXAFS and TDS data provide indications of chemisorption [92], UPS data [93] and DFT modeling [94] are suggesting rather physisorption of PEN on Ag(111).

STM measurements of PEN molecules on Ag(111) displayed a particular adsorption behaviour. At RT, no STM images could be taken of molecules in direct contact with the Ag(111) substrate. Such behavior that does not allow to take STM pictures of adsorbed molecules is named "liquid-like". The reason is weak interaction between molecule and metal and therefore a high mobility of molecules, probably triggered by the STM tip. A different situation was observed for PEN molecules, which adsorb on top of one closed PEN ML. There, individual molecules could be imaged [95]. Only at 50 K, it was possible to display PEN molecules with STM in the first layer on Ag(111) [96]. However, it is not necessary to cool the sample down to 50 K. Low energy atom diffraction measurements observed no structural changes in the monolayer between 200 K and 50 K [97].

More recently, a theoretical study dealt with the adsorption of PEN on Ag(111) for an isolated molecule and a complete ML [94]. Their calculations reveal a rise of the bonding distance from 3.9 Å to 4.1 Å for the two extremal coverages due to intermolecular forces, which become more and more important with increasing coverage and hinder the molecule to find the energetically best adsorption site with respect to the substrate.

Here, our aim is to investigate the bonding distance for the disordered RT phase and for the ordered LT phase for different coverages, in order to assess the interaction strength, depending on coverage and temperature.

5.4.2 XPS measurements of PEN on Ag(111)

Each C 1*s* spectrum of both films was background subtracted. Fitting was done with only one Gaussian, see Figure 5.14, in contrast to PEN on Cu(111). There, a double peak was observed being split by 0.6 eV, which was explained with strong interaction of the molecule with the Cu(111) surface [14].

For the 0.5 ML film of PEN on Ag(111), the peak is located at $E_B = 284.8$ eV with $FWHM = 1.4$ eV, both for the RT and for the LT film. Small changes of these values were observed for the film with a coverage of 0.75 ML. There, the binding energy of the C 1s is $E_B = 285.1$ eV at RT and $E_B = 285.0$ eV at LT. The width of both Gaussians is slightly reduced to $FWHM = 1.1$ eV each.

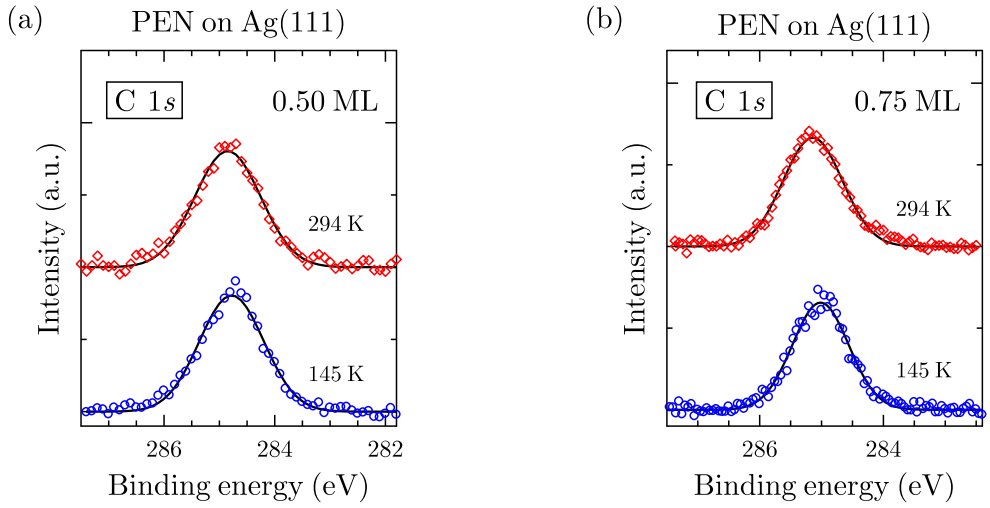

Figure 5.14: C 1s spectra of PEN on Ag(111) for a coverage (a) of 0.5 ML and (b) of 0.75 ML. The LT spectra are marked with circles in blue, the RT are marked with diamonds in red. For details see text.

5.4.3 XSW measurements of PEN on Ag(111)

To determine temperature and coverage dependent bonding distances, a minimum of three XSW scans were taken for each film at each temperature. Representative sets of data together with their fitting results of the four scenarios is plotted in Figure 5.15. For the 0.5 ML film, the bonding distance is similar for the RT and LT, being $d_H^{RT} = (2.99 \pm 0.01)$ Å and $d_H^{LT} = (3.04 \pm 0.01)$ Å. The error is given from the standard deviation. Upon cooling from 294 K to 145 K an increase of the coherent fractions can be observed from $f_H^{RT} = 0.78$ to $f_H^{LT} = 0.94$. We estimate an error of 0.05 for the coherent fractions. For the film with a coverage of 0.75 ML we measured both at RT and LT a bonding distance of $d_H = (3.13 \pm 0.01)$ Å. The coherent fractions increased from $f_H^{RT} = 0.64$ to $f_H^{LT} = 0.73$. All results are summarized in Table 5.4.

5.4.4 Discussion

On a first instance one can observe for PEN on Ag(111) a coverage dependent, but no (or only minor) temperature dependent bonding distance. The values, ranging between 2.99 Å and 3.13 Å – lower than the calculated values (3.9 Å - 4.1 Å [94]) – are significantly larger compared to the bonding distance of PEN on Cu(111) ($d_H = 2.34$ Å [14]) due to

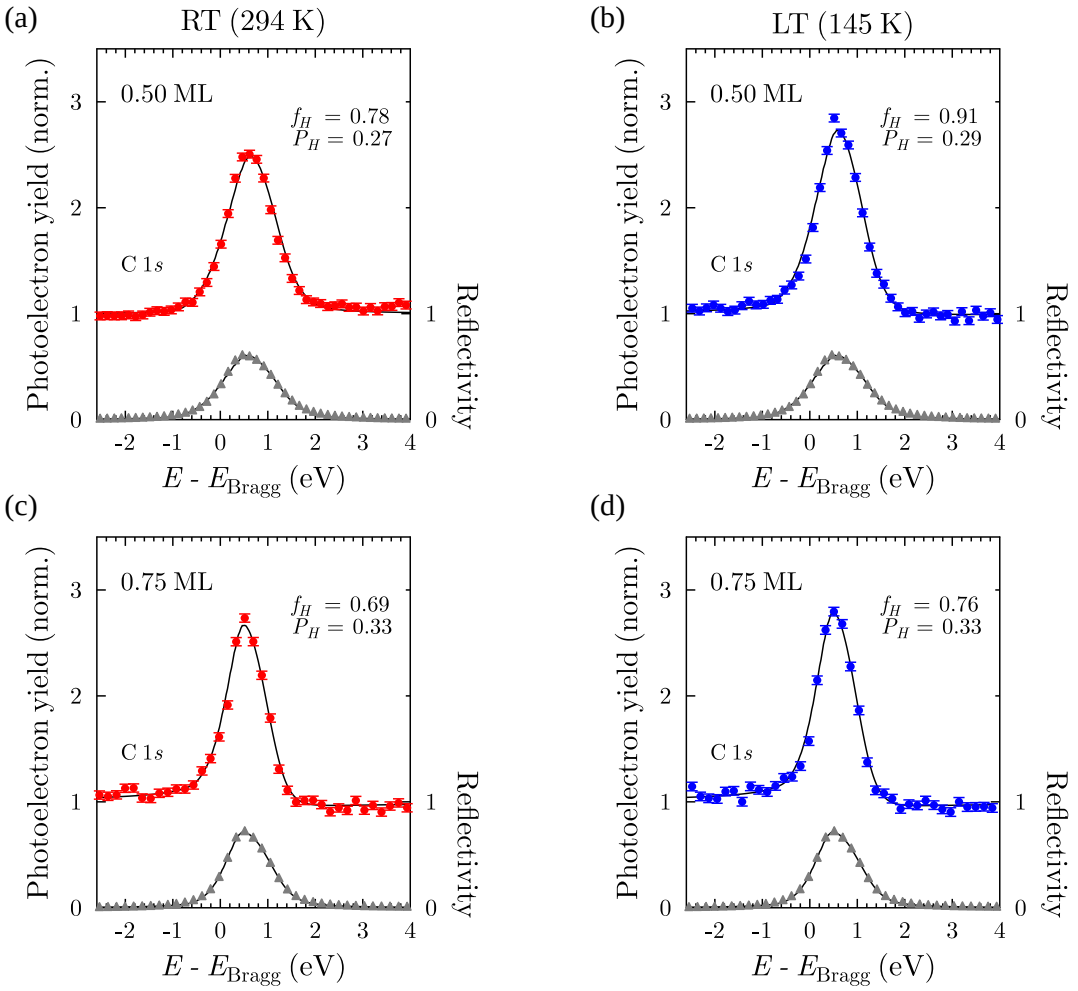

Figure 5.15: Reflectivity (triangles) and photoelectron yield curves (circles) of PEN on Ag(111) for two different coverages (0.5 ML and 0.75 ML), each measured at two temperatures (294 K and 145 K).

Table 5.4: Results of temperature and coverage depending XSW experiments of PEN on Ag(111): Coherent fraction f_H, coherent position P_H, and bonding distance d_H. The values refer to the average of several XSW measurements with the corresponding standard deviation as error bars.

ϑ	T	f_H	P_H	d_H
0.50 ML	294 K	0.77 ± 0.05	0.267 ± 0.005	(2.99 ± 0.01) Å
0.50 ML	145 K	0.94 ± 0.05	0.294 ± 0.004	(3.04 ± 0.01) Å
0.75 ML	294 K	0.64 ± 0.05	0.326 ± 0.004	(3.13 ± 0.01) Å
0.75 ML	145 K	0.73 ± 0.05	0.330 ± 0.005	(3.13 ± 0.01) Å

weaker molecule–substrate interaction on Ag(111). This finding is supported by the XPS data of only one C 1*s* peak for Ag(111) in contrast to the Cu(111) substrate, where the double peak of the C 1*s* peak was rationalized with the same argument.

The temperature does not influence the bonding distance, although the adsorption behaviour changed from the disordered 'liquid-like' phase at RT to an ordered phase with well defined adsorption places of the molecules at LT. Our results are in line with other XSW results, investigating the influence of temperature on the bonding distance. E.g., neither HBC on Au(111), as described in Section 5.3, nor CuPc on Cu(111), Au(111) [86], and Ag(111) [19] showed a temperature dependence.

On the other hand, we see an increase of the bonding distance by 3%–5% with coverage from 0.5 ML to 0.75 ML for PEN on Ag(111). This result can be explained with intermolecular forces, playing a larger role for smaller molecule–molecule distances and hinder the molecule to find the most favourable adsorption site with respect to the substrate. A similarly increasing bonding distance with coverage was found for CuPc on Ag(111) [19] and – even more pronounced – on Cu(111) [86]. Only for CuPc on Au(111) no coverage dependence of the bonding distance was found, due to the weak interaction between molecule and metal [86].

Summing up our observations, the coverage dependent bonding distance of PEN an Ag(111) indicates an interaction, which is stronger than physisorption. Yet, typical observations for chemisorbed systems are missing, leading to the conclusion that this system is in between the two extremal cases of interaction and hence might be named with 'soft chemisorption' [91].

5.5 Bilayer: PFP on PEN on Cu(111)

5.5.1 Introduction

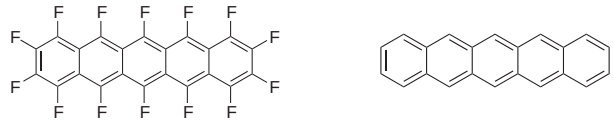

Figure 5.16: Molecular structure of PFP (left) and PEN (right).

In addition to the interface between organic molecules and metals also heterostructures of two different organic molecules are crucial for devices based on organic molecules. For instance, organic photovoltaic cells typically consist of – at least – two different organic compounds, whose interface properties are responsible for the device performance. Generally, the electronic and geometrical properties of the organic-organic interface is, in fact, least understood. Determination of these properties might answer the question of the interaction strength between the two molecular species. As our model system we chose the heterostructure of pentacene (PEN, $C_{22}H_{14}$) and its perfluorinated counterpart, (PFP, $C_{22}F_{14}$, molecular structure shown in Figure 5.16). Both molecules together represent a prototypical donor-acceptor system and have been studied intensely during the last years, including the two molecules individually at monolayer coverages [14, 98] and in thin films [99–101], and the molecules in mixed thin films [102–107].

It was shown in an XSW study by Koch *et al.* [14] that both PEN and PFP adsorb on Cu(111) in a flat lying phase, but differ considerably in adsorption height. The PEN molecule has a significantly lower bonding distance than its perfluorinated counterpart. Additionally, the bending of the fluorine atoms above the carbon backbone results in a distortion of the molecule. As the fluorine atoms have negative partial charge, such a molecular distortion implies a permanent dipole moment influencing the work function and hence the charge transport of such a sample. Our aim here is to study how the interaction of PFP with the Cu(111) substrate changes if a monolayer of the prototypical hydrocarbon PEN is placed in between.

In our first step we prepared a monolayer of PEN on Cu(111). During evaporation of PEN (nominal evaporated thickness: 15 Å) we kept the temperature of the substrate at $\sim$ 450 K. At this temperature the second layer of PEN starts to desorb on Cu(110) [108] and ensures that no molecules beyond the first layer adsorbs. After this monolayer preparation we performed XSW measurements of PEN on Cu(111).

Secondly, we evaporated a submonolayer of PFP on top of the monolayer PEN on Cu(111), followed by XSW and XPS measurements. The XPS signal of carbon can be fitted with three peaks, which is done in Figure 5.17. The largest peak corresponds to the carbon atoms of the PEN molecule. The two smaller peaks are related to the PFP molecule: The peak at higher binding energy emerges from the C–F binding, the other peak from the C–C binding within the PFP molecule. This XPS analysis allows to distinguish the photoelectron yield from the carbon atoms of PEN from the carbon atoms of PFP. Hence, a separate determination of the bonding distance of the carbon core of PEN and PFP within the bilayer system is possible.

5.5.2 XPS measurements of PFP on PEN on Cu(111)

The XPS analysis contains spectra of the fluorine and of the carbon atoms and is displayed in Figure 5.17. Based on the XPS analysis described in the following for the C 1*s* spectrum, the photoelectron yield of PEN and PFP was obtained. The F 1*s* XP spectrum is fitted with one Gaussian located at $E_B = 688.5$ eV. The C 1*s* spectrum of the bilayer is

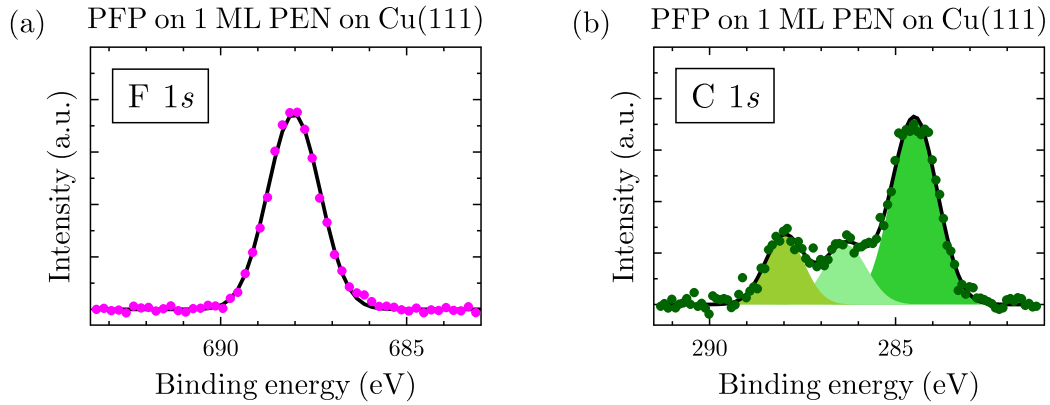

Figure 5.17: C 1*s* and F 1*s* core-level signal of PFP on PEN on Cu(111). The C 1*s* spectrum is fitted with three Gaussians, one for the PEN at low binding energy, and two for the PFP molecule (C–C and C–F bonds). Spectra are taken at $E_{ph} = 2975$ eV.

split up into three contributions, each of them fitted with a Gaussian. The highest peak has a binding energy of 284.5 eV and is related to the PEN molecule. The two lower peaks correspond to the PFP molecule, whose carbon atoms have two different binding types, one from the C–C bond ($E_B = 286.3$ eV) and the other from the C–F bond ($E_B = 287.9$ eV). The XPS measurements from Ref. [14] on monolayers of PEN on Cu(111) revealed a C 1*s* double peak at binding energies of 284.9 eV and 285.55 eV. The splitting is explained by strong chemisorption of PEN on Cu(111). Due to the resolution in our XPS measurements, this feature cannot be resolved, but the broad peak provides an indication of this feature. Our binding energy of PEN in the bilayer is lower than the earlier results. Glowatzki *et al.* measured one ML PFP on Cu(111), finding the carbon peaks at 285.8 eV (287.3 eV) for the C–C (C–F) components and the fluorine peak at 287.5 eV [109]. However, in our case PFP adsorbs in the second layer, and the interaction will be different than in the monolayer on Cu(111). A thick PFP film on Ag(111) was analyzed by Götzen *et al.* [110]. For thick films the influence of the substrate can be neglected. Their binding energies are at 286.3 eV for the C–C and 287.8 eV for the C–F peaks, while the fluorine peak is located at 688.0 eV.

The intensity ration between the PEN and PFP components is 1.65. Assuming the same unit cell size for PEN and PFP on top of PEN we can estimate that the PEN ML is covered by $\leq 65\%$ with PFP molecules. The equals sign can be chosen only if the PFP molecules do not scatter those photoelectrons that are released from the underlying PEN molecules.

Table 5.5: C 1*s* binding energies of PFP within the bilayer PFP on PEN/Cu(111), and comparison with binding energies from a ML of PFP on Cu(111) and a PFP multilayer film, found in literature.

System	C 1*s*		F 1*s*
	C–C	C–F	
PFP on PEN/Cu(111)	286.3	287.9	688.0
ML PFP on Cu(111) [109]	285.8	287.3	687.5
multilayer PFP [110]	286.3	287.8	688.0

5.5.3 XSW measurements of PFP on PEN on Cu(111)

A representative XSW measurement of 1 ML of PEN and of the bilayer PFP on PEN on Cu(111) can be seen in Figure 5.18. All fit results of the XSW scans are summarized in Table 5.6.

Our XSW results of the monolayer PEN on Cu(111) is a bonding distance of $d_H = 2.43$ Å. Upon deposition of a submonolayer PFP on top of the ML PEN, the bonding distance of PEN is slightly reduced to 2.35 Å. For the bonding distance of the PFP molecule we have

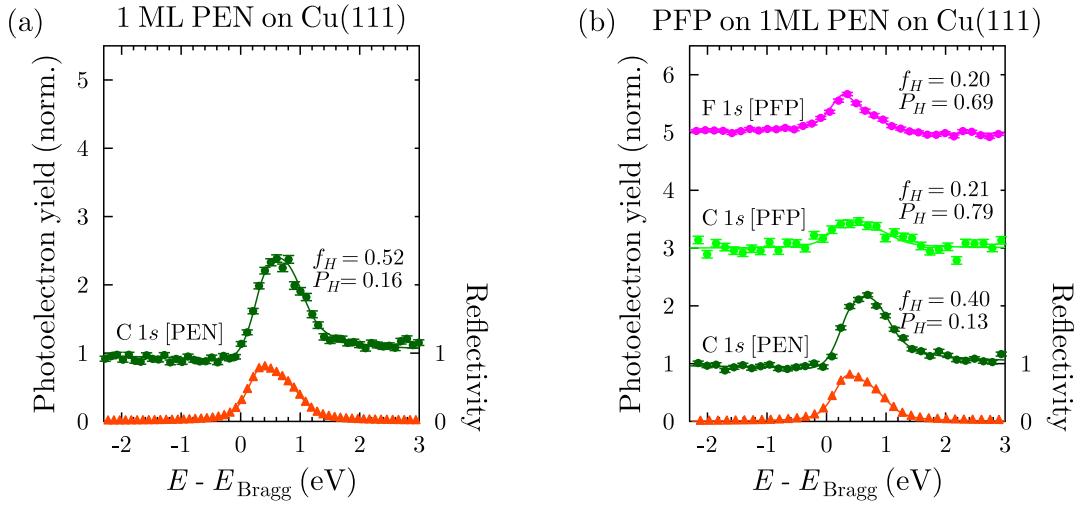

Figure 5.18: Photoelectron yield curves (circles) for 1 ML of PEN on Cu(111) [left] and of the bilayer PFP on PEN on Cu(111). The triangles mark the reflectivity of the (111) Bragg reflection of the substrate.

to consider the n-ambiguity of the coherent position. To understand this we should recall the basic idea that the XSW field appears also above the crystal with the periodicity of the substrate lattice spacing. The n-value determines, which lattice plane is chosen ($n = 0$: topmost atomic layer of the substrate single crystal; $n = 1$: first extrapolated lattice plane in vacuum above the crystal; etc.). The coherent position is determined with respect to a lattice plane. For PEN on Cu(111), $n = 1$ is chosen, and with the knowledge of the

spacing of two lattice planes d_0 the formula $d_H = (n + P_H) \cdot d_0$ can be used to determine the distance d_H with respect to the topmost atomic layer of the Cu(111) substrate. For

Table 5.6: XSW results (coherent fraction f_H, coherent position P_H, and distance to the uppermost Cu(111) layer) of the ML PEN on Cu(111) and of the bilayer PFP on PEN on Cu(111).

Atom (Mol.)	System	f_H	P_H	d_H (Å)
C 1s (PEN)	PEN/Cu(111)	0.48	0.16	2.43 ± 0.02
C 1s (PEN+PFP)	PFP/PEN/Cu(111)	0.13	0.05	4.28 ± 0.08
C 1s (PEN)	PFP/PEN/Cu(111)	0.36	0.13	2.35 ± 0.03
C 1s (PFP)	PFP/PEN/Cu(111)	0.23	0.75	5.73 ± 0.06
F 1s (PFP)	PFP/PEN/Cu(111)	0.22	0.66	5.54 ± 0.08

the carbon atoms of the PFP molecule we measured $P_H = 0.75$. To obtain a sensible distance for PFP that adsorbs in the second layer, $n = 2$ has to be chosen. In that case, the distance of PFP to the topmost lattice plane is 5.73 Å. Analogue considerations for the fluorine atoms of PFP yield a distance of 5.54 Å above the Cu(111) surface, i.e. the fluorine atoms are 0.19 Å below the carbon backbone of PFP.

5.5.4 Discussion

In the first step of the experiment we could reproduce the earlier result of PEN on Cu(111). The measured bonding distance is with 2.43 Å only slightly higher than the results from Koch *et al.* ($d_H = 2.35$ Å [14]). We have to consider that the bonding distance of PEN presented in this work was measured using a different XSW setup compared to the PEN bonding distance from Ref. [14]. For the setup of the latter experiment the use of non-dipole parameters was necessary. The small deviation of the bonding distance can also emerge from a different coverage. In this work a complete ML was measured, while Koch *et al.* analyzed a submonolayer coverage. The coverage-dependence of the bonding distance, i.e. an increasing bonding distance with increasing coverage, was found, among others, for PEN on Ag(111), which was described in Section 5.4.

For the bilayer system, the bonding distance of PEN is reduced relative to the bare ML, from 2.43 Å to 2.35 Å. No significant change of the bonding distance of PEN indicates that the ML of PEN stays intact after deposition of PFP molecules. This finding is further supported by the coherent fractions. For the total C 1s photoelectron yield, arising from both PEN and PFP molecules, the coherent fraction is $f_H = 0.13$. If the contributions from PFP and PEN to the overall signal are separated by an XPS analysis as described above in Section 5.5.2, the coherent fractions increase, for PEN to $f_H = 0.36$, which is closer to the ML value, and for PFP to $f_H = 0.23$. This increase of the coherent fractions is a sign for higher vertical order of the individual molecules and provides evidence that significant diffusion of PFP molecules into the first molecular layer is unlikely. If intermixing takes

place, the coherent fraction of PFP would even be lower compared to the overall C 1*s* signal. We can conclude therefore that PFP adsorbs on top of the PEN ML.

The individual measurements of the components within the bilayer are displayed in the Argand diagram in Figure 5.19(a). Open circles are related to the C 1*s* of PEN and crosses mark the results of C 1*s* of PFP. The sum of both C 1*s* components are related to the crossed circles. The XSW results of F 1*s* are represented by stars.

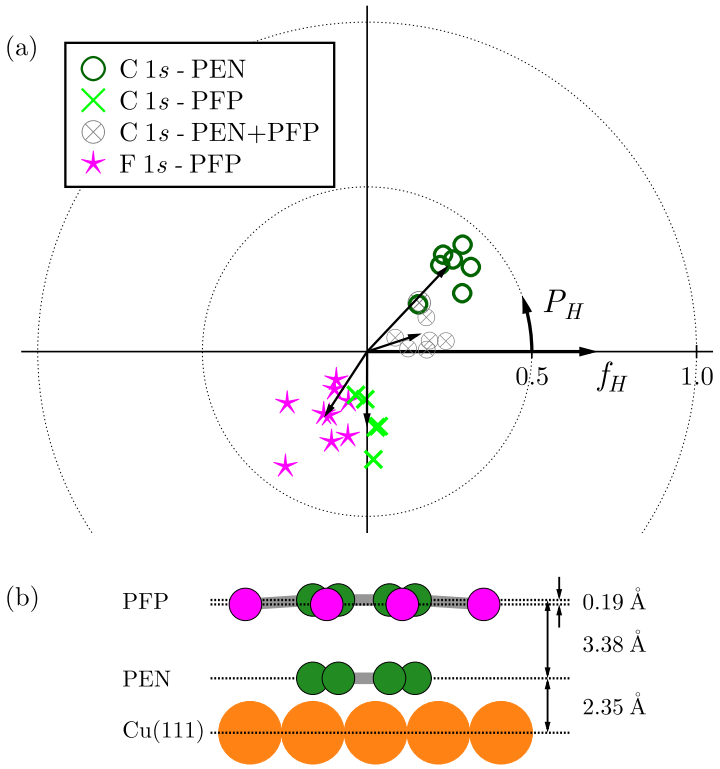

Figure 5.19: (a) Argand diagram displaying the results of the bilayer PFP on PEN on Cu(111). Each marker corresponds to the result of a single XSW scan. The position is determined by f_H (length of a vector) and P_H (angle of the vector). The different symbols represent different atoms: Carbon atoms from PEN (open circle), carbon atoms from PFP (cross), the sum of both (crossed circle), and the fluorine atoms of PFP (stars). (b) Schematic picture of the adsorption geometry of PFP on PEN on Cu(111).

For the bilayer system, the measured distance of the carbon atoms of PFP to the substrate surface is 5.73 Å, while PEN adsorbs at a bonding distance of 2.35 Å. The vertical distance between the backbones of PEN and PFP is therefore 3.38 Å. The latter value is a typical interplanar distance in crystals of π-conjugated molecules of one type. In molecular crystals this distance is explained with the sum of two carbon vdW radii (3.4 Å), and can be related to weak interaction (physisorption) between the backbones of the two molecules. Also for single crystals made of mixtures of octafluoronaphthalene with different polyaromatic hydrocarbons similar intermolecular distances are found. These crystal represent a situation, which is close to our system, as they consist of aromatic hydrocarbon and

perfluorinated molecules. The reported interplanar distance between these two different molecules is 3.39 Å [111] and therefore very similar to our result.

The fluorine atoms of PFP have a bonding distance of 5.54 Å and are therefore bent downwards by 0.19 Å, toward the PEN molecule. Figure 5.19(b) shows schematically the geometric result of the bilayer. The bending of the fluorine atoms toward the PEN molecules is probably induced by quadrupole interaction. The quadrupoles emerge due to the polar bonds between H–C and F–C of the PEN and PFP molecule. Therefore, within a PEN molecule positive partial charge is at the place of the hydrogen atoms and negative partial charge in the central part of the molecule, at the positions of the carbon atoms. For the PFP molecule partial charge distribution is qualitatively reversed, resulting in Coulomb-attraction between the two molecules.

Now we turn to a comparison of the PFP C 1*s* binding energies. In the ML, the metal substrate screens the hole created by the photoemission process and the attraction of the escaping electron to the hole is reduced. This screening is less effective in the multilayer due to a small polarizability of the organic compound, decreasing the kinetic energy of the photoelectron and shifting the binding energy to a higher value. According to Table 5.5, the PFP in the bilayer displays the same binding energies than a multilayer of PFP.

In the literature XSW results of a different bilayer can be found. A ML of PTCDA was prepared on Ag(111), and CuPc was added on top of PTCDA [112]. As in our case, the PTCDA molecules are slightly pressed toward the substrate upon adsorption of CuPc (from 2.86 Å to 2.81 Å). The CuPc molecules adsorb in a flat geometry within differences of the adsorption height of 0.1 Å, and the distance to the PTCDA layer is 3.22 Å. This value is smaller than the sum of two carbon vdW radii, indicating a stronger interaction mechanism between CuPc and PTCDA compared to the case of PFP on PEN/Cu(111). In addition, the bilayer F_{16}CuPc on CuPc/Ag(111) was analyzed recently, the distance between F_{16}CuPc and CuPc is 3.06 Å. There, no distortion of the perfluorinated molecule is observed.

The bilayer PFP on PEN/Cu(111) was prepared and the bonding distances of the individual compounds could be resolved. Our XSW measurements suggest that the carbon skeletons of both molecules are interacting mainly via vdW forces. To gain further insight into the organic-organic interface, a collaboration with theoreticians was set in to model this bilayer system using state-of-the-art DFT calculations.

5.6 COHON and PYT on Cu(111)

5.6.1 Introduction

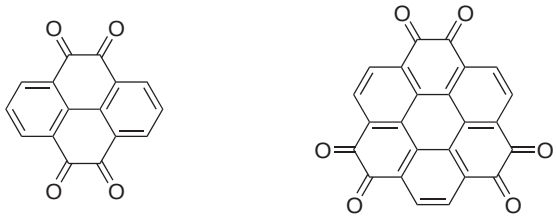

Figure 5.20: Molecular structure of PYT (left) and COHON (right).

The adsorption geometry of P4O on Au(111) is explained in Section 5.2 as part of a systematic study on PEN derivatives – 6,13-pentacenequinone (P2O) and pentacene-5,7,12,14-tetraone (P4O) – on Cu(111), Ag(111), and Au(111) [84]. In the gas phase, the conjugation of the rod-like molecules P2O and P4O does not extend over the whole molecule, as it is interrupted by the carbonyl groups. However, when they adsorb on certain (111)-surfaces of coinage metals they suffer a surface-induced aromatic stabilization. This phenomenon includes a CTC and hybridization, which extends the conjugation over almost the whole molecule and renders the monolayer metallic. In addition, chemical shifts of the C 1*s* and O 1*s* core-levels were observed.

To see whether the adsorption behavior described there can be extended to other COMs, which contain on the one hand a carbon backbone with embedded carbonyl-groups and on the other hand a different shape, the disk-like COMs coronene-hexaone (COHON, $C_{24}H_6O_6$) and pyrene-4,5,9,10-tetraone (PYT, $C_{16}H_6O_4$, molecular structure shown in Figure 5.20) are measured on Cu(111) with XSW. PYT is a relatively small molecule containing four carbonyl-groups and has the ability to host side groups as bromine atoms or nitro (NO_2) groups, e.g., in order to change the functionality of the molecule. The influence on NO_2-side group on the bonding distance is studied in Section 5.7 for the Ag(111) substrate. COHON is a discoidal COM made of six benzene units attached to a ring and hosts six carbonyl-groups, i.e. more than P2O, P4O and PYT.

The study of COHON and PYT on Cu(111) was performed using the old XSW setup at the ESRF, and non-dipole parameters in the XSW analysis are required.

5.6.2 XPS measurements of COHON and PYT on Cu(111)

The C 1*s* and O 1*s* spectra are shown in Figure 5.21. We will start with COHON, whose slightly asymmetric C 1*s* spectrum can be fitted with two Gaussians at binding energies of 285.0 eV and 286.2 eV. For the O 1*s* spectrum, the peak is located at 531.1 eV. The results for PYT are similar: The C 1*s* signal consists of two contributions, one peak at 284.7 eV, the other at 285.8 eV. The O 1*s* peak is located at 530.7 eV.

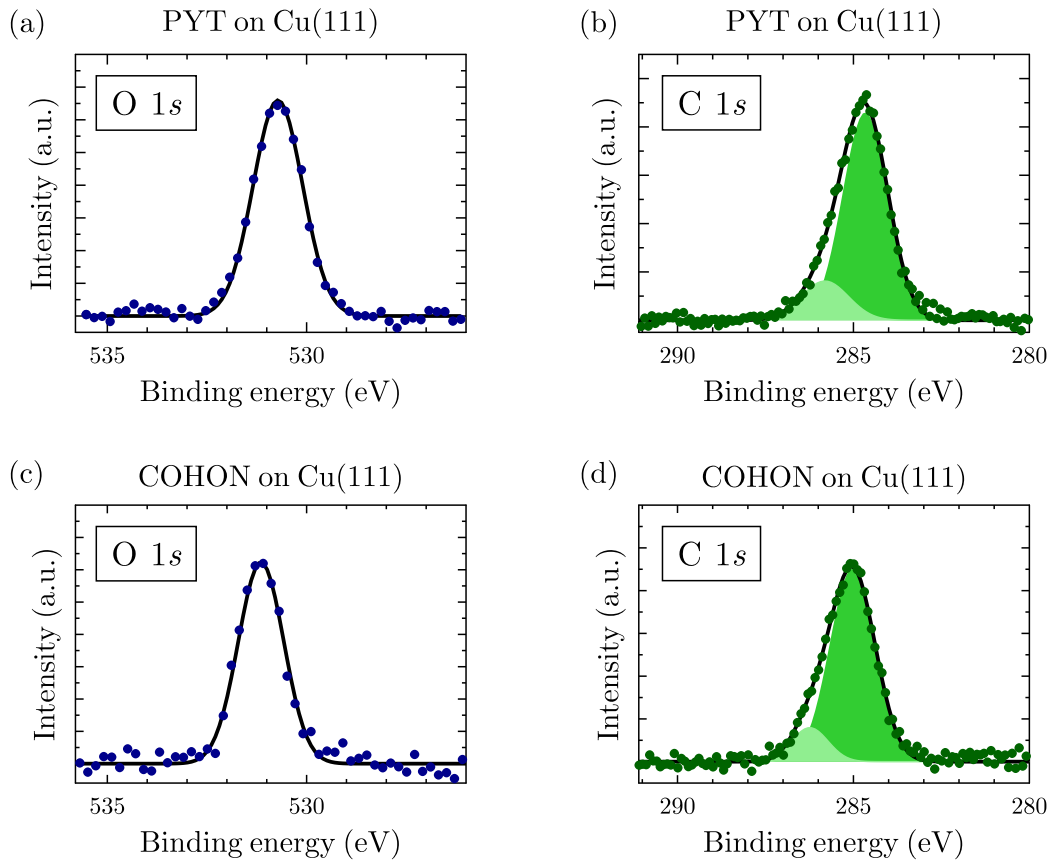

Figure 5.21: XP spectra of COHON and PYT on Cu(111).

5.6.3 XSW measurements of COHON and PYT on Cu(111)

The XSW analysis of COHON and PYT on Cu(111) is exemplarily shown in Figure 5.22. For COHON on Cu(111) we get on average of measurements at different spots for the carbon atoms $f_H = 0.25 \pm 0.05$ and $P_H = 0.17 \pm 0.02$, and for the oxygen atoms $f_H = 0.48 \pm 0.03$ and $P_H = 0.03 \pm 0.01$. Their bonding distances are 2.45 ± 0.04 Å and 2.14 ± 0.03 Å, respectively. The XSW analysis for PYT on Cu(111) reveals on average for the carbon atoms a coherent fraction of $f_H = 0.35 \pm 0.03$ and a coherent position of $P_H = 0.11 \pm 0.01$. The analysis of the oxygen atoms leads to $f_H = 0.43 \pm 0.05$ and $P_H = 0.97 \pm 0.02$. The average bonding distance of the carbon skeleton is therefore 2.31 ± 0.03 Å, whereas the oxygen atoms adsorb at a distance of only 2.04 ± 0.06 Å.

5.6.4 Discussion

The XSW analysis of COHON and PYT on Cu(111) shows two strongly distorted molecules. The relative distortion within each molecule is in both cases very similar, the oxygen atoms adsorb almost 0.3 Å below the average carbon adsorption height. Looking at the absolute numbers, the carbon atoms of COHON adsorb at a larger bonding distance

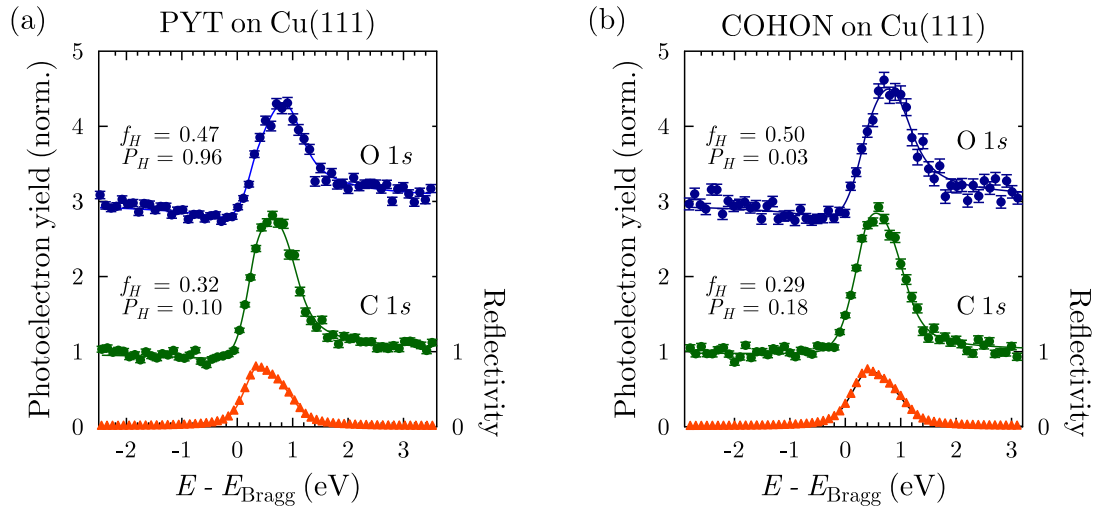

Figure 5.22: Representative photoelectron yield curves (circles) of COHON and PYT on Cu(111) for the carbon and oxygen atoms together with their fit results. The triangles mark the reflectivity of the Cu(111) substrate.

than those of PYT, whose bonding distance is very similar to the PEN derivatives P2O and P4O on Cu(111) [84]. In addition to the similarity of the XSW results of PYT and COHON with the PEN derivatives, we see an analogy in the XPS. In the C 1s spectra of PYT and COHON, the side peak, being related to the bond to the oxygen atom, is located close to the main peak. In contrast, the weakly interacting P4O on Au(111) exhibits a clearly separated side peak (see Figure 5.7), a few eV above the main peak. Therefore, the XPS data of PYT and COHON on Cu(111) are an evidence for a charge redistribution at the place of the carbonylic carbon atom, probably related to a charge transfer from the substrate to the molecule leading toward a C–O single bond. Also the strong distortion of the molecule is a hint that the C=O double bond changed toward a single bond, as the latter is expected to be more flexible. The small bonding distance of the oxygen atoms and the chemically shifted C 1s peak of the carbonyl groups are evidence for a covalent bond of the oxygen atoms with substrate atoms. We can conclude that COHON and PYT behave on Cu(111) qualitatively in the same way as P2O and P4O on Cu(111). The carbonyl group plays an important role for the bonding of these molecules on Cu(111). One exception is PTCDA on Cu(111), whose carbonylic oxygen atoms are bent upwards and the average carbon bonding distance is substantially higher than PYT ($\Delta d_H \sim 0.3$ Å) and COHON ($\Delta d_H \sim 0.15$ Å). PTCDA contains besides the carbonylic oxygen atoms two anhydride oxygen atoms, which might be responsible for the different interaction mechanism.

5.7 PYT and NO2PYT on Ag(111)

5.7.1 Introduction

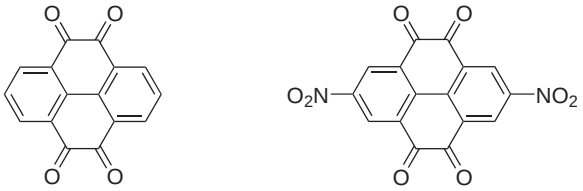

Figure 5.23: Molecular structure of PYT (left) and NO2PYT (right).

PYT is a strong electron accepting and relatively lightweight molecule. A possible problem of light molecules is the diffusion of the molecule into layers of a different organic material. By adding two NO_2 (nitryl)-groups, the molecular weight of the new molecule 2,7-dinitropyrene-4,5,9,10-tetraone (NO2PYT, $C_{16}H_4N_2O_8$, molecular structure shown in Figure 5.23) is increased, and the probability of diffusion is reduced. Interlayer diffusion was observed for the small organic acceptor 2,3,5,6-tetrafluoro-7,7,8,8-tetracyanoquinodimethane (F4-TCNQ), and diffusion of molecules into the neighbouring organic compound is considered a major problem for the production of reliable and stable organic devices. To shed light on the influence of side groups on the bonding distance, PYT and NO2PYT were investigated with the XSW technique on Ag(111). These results are a first step to understand, if or how side groups change the interface properties. First, by comparing the XSW results of PYT on Ag(111) with the ones of the Cu(111) substrate (see Section 5.6) we can study, whether the adsorption mechanism of PYT depends on the substrate. Second, we can address the question, whether the side groups modify the interaction of the molecule with the Ag(111) substrate.

The study of PYT on Ag(111) was performed using the old XSW setup at the ESRF. Therefore, non-dipole parameters in the XSW analysis are required.

5.7.2 XPS measurements of PYT and NO2PYT on Ag(111)

The XPS analysis for PYT on Ag(111) reveales one symmetric C 1s peak at 284.8 eV and one peak of O 1s at 530.9 eV. The O 1s signal is slightly assymmetric. The second peak is probably related to contamination during sample preparation. However, we are confident that the XSW results are not affected significantly for reasons given later. The XPS analysis of NO2PYT was done for the C 1s and O 1s core-levels by fitting each spectrum with two Gaussians. The two components of the C 1s signal were found at $E_B^{C-N} = 287.2$ eV and at $E_B^{C-C} = 284.4$ eV. The O 1s signal is split up in components originating from the carbonyl group and from the nitryl group. Their binding energies are $E_B^{O=C} = 529.6$ eV and $E_B^{O-N} = 531.3$ eV, respectively. The ratio of the peak intensities of $I(O=C)/I(O-N) = 0.9$ is close to the expected value of 1.

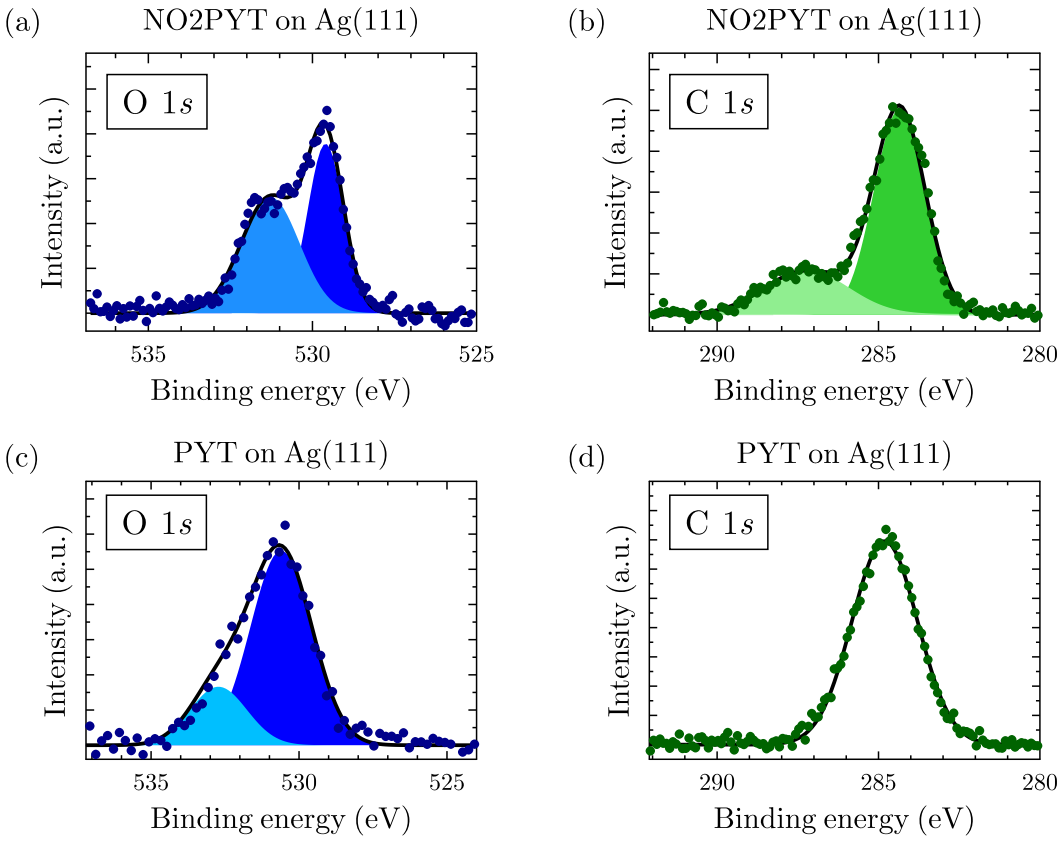

Figure 5.24: XP spectra of C 1*s* and O 1*s* of PYT (bottom panel) and NO2PYT (upper panel) on Ag(111).

5.7.3 XSW measurements of PYT and NO2PYT on Ag(111)

Our results of the XSW analysis of PYT on Ag(111), an average of several individual XSW scans, are a coherent fraction $f_H = 0.29 \pm 0.06$ and a coherent position $P_H = 0.05 \pm 0.01$ for the carbon atoms, and $f_H = 0.47 \pm 0.06$ and $P_H = 0.96 \pm 0.02$ for the oxygen atoms. The average bonding distance for the oxygen atoms is 2.25 ± 0.04 Å, significantly lower than the carbon atoms, which adsorb on average at a distance of 2.47 ± 0.03 Å.

A representative XSW yield curve for the atoms of PYT and NO2PYT on Ag(111) is displayed in Figure 5.25. The analysis for the NO2PYT molecule on Ag(111) shows $f_H = 0.59 \pm 0.11$ and $P_H = 0.20 \pm 0.01$ for the carbon atoms, $f_H = 0.55 \pm 0.10$ and $P_H = 0.95 \pm 0.02$ for the carbonyl oxygen, and $f_H = 0.42 \pm 0.09$ and $P_H = 0.11 \pm 0.03$ for the nitryl oxygen. The coherent positions can be translated into average bonding distances of 2.82 ± 0.02 Å for the carbon atoms, 2.61 ± 0.07 Å for the nitryl oxygen, and 2.23 ± 0.03 Å for the carbonyl oxygen atoms.

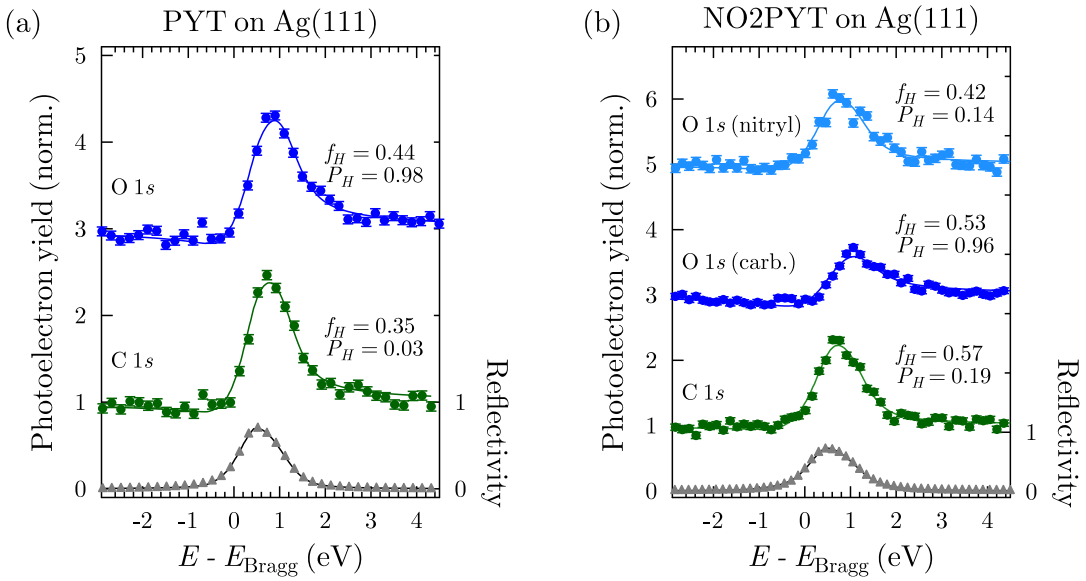

Figure 5.25: Photoelectron yield curves (circles) of PYT and NO2PYT on Ag(111). For NO2PYT it is possible to distinguish between the oxygen of the carbonyl groups and the oxygen of the nitryl group. For details see Section 5.7.2.

5.7.4 Discussion

We begin the discussion with PYT. On Ag(111), the XSW results show a distorted molecule, with the carbonylic oxygen atoms being bent towards the Ag(111) surfaces, very similar to the adsorption geometry on Cu(111) described previously in Section 5.6. The difference in adsorption height on Ag(111) between the carbon and oxygen atoms is ~ 0.2 Å, which implies a distorted molecule. Regarding the core-level analysis, we observe no second peak a few eV above the main peak in the C 1s spectrum. This peak is expected

to emerge from the C=O bond and occurred for the weakly interacting P4O on Au(111) in Section 5.2. Therefore, the C 1*s* spectrum here is an indication of a charge transfer from PYT to the metal. This charge transfer modifies the bond substantially and is a sign for surface-induced aromatic stabilization [84]. The lower coherent fraction for the carbon atoms compared to the oxygen atoms can be explained with the distorted molecule, in which carbon atoms at different positions within the molecule have different adsorption heights. It is likely that the carbon core is bent in a way, where the carbonylic carbon atoms are closer to the surface than the other carbon atoms. The small bonding distance of the oxygen atoms are a sign for a bond of a covalent type between oxygen and silver atoms. Thus, the oxygen atoms have a preferred adsorption site on the surface. This finding is further supported by the high coherent fraction of the oxygen atoms compared to the carbon atoms, indicating vertically ordered oxygen atoms. This means that, even if the O 1*s* peak is broadened due to contamination, the latter does not play a big role, as a decrease of the coherent fraction would be expected in a more drastic way.

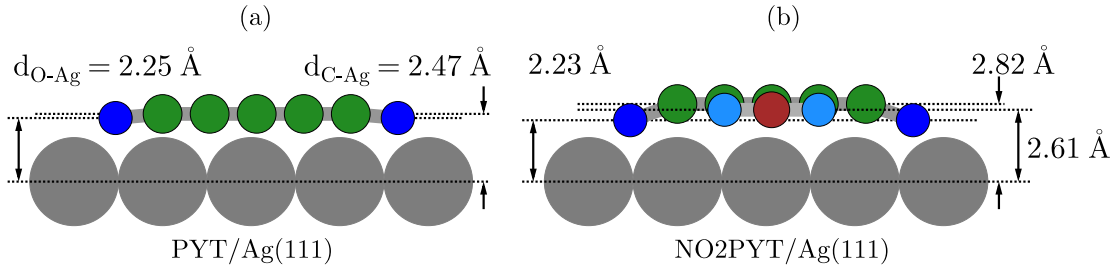

Figure 5.26: Schematic of the adsorption geometry of (a) PYT and (b) NO2PYT on Ag(111). The carbon skeleton is displayed flatly, because the XSW experiments yield an average of all carbon atoms. It is expected that the skeleton is bent.

Now we turn to the PYT derivative. For a better understanding, Figure 5.26 provides the schematic adsorption geometry of PYT and NO2PYT. For NO2PYT we observe again a similar distortion of the molecule regarding the carbonyl oxygen. However, the carbon atoms have a larger bonding distance compared to the pure PYT molecule. The average distance between the carbonylic oxygen and the carbon atoms is now ~ 0.6 Å. The nitrylic oxygen atoms, which are located in the side groups, adsorb at lower bonding distances than the carbon atoms. In relation to PYT on Ag(111) we can conclude that the NO_2 side groups apparently have an influence on the adsorption mechanism. While the carbonylic oxygen atoms adsorb at the same height as it was observed for PYT, the carbon skeleton is pulled away from the surface by ~ 0.35 Å.

5.8 H2Pc on Cu(111)

5.8.1 Introduction

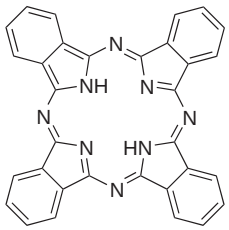

Figure 5.27: Molecular structure of H2Pc.

The phthalocyanine (Pc, $C_{32}H_{16}N_8$) molecule can be modified relatively easy, because the center of the macro-cycle can host either two hydrogen atoms (H2Pc, molecular structure shown in Figure 5.27) or a metal atom (MPc). Therefore, dozens of different MPc molecules exist, each of them with potentially different properties, making Pcs interesting components for electronic devices [113, 114]. This huge potential led to intense research of different metal Pcs on metal surfaces, using the whole spectrum of analysis techniques.

One way to get a better understanding of the adsorption mechanism and the influence of the central metal ion on the bonding distance and therefore the interaction strength between Pc and metal substrate is to compare the metallized Pcs with the metal-free Pc (H2Pc). Some MPcs have already been studied on Cu(111) with the XSW technique [11, 79, 86, 115, 116]. In addition, H2Pc has been investigated on Ag(111) using XSW, i.a. [117].

The study of H2Pc on Cu(111) was performed using the old XSW setup at the ESRF, and non-dipole parameters in the XSW analysis are required.

5.8.2 XPS measurements of H2Pc on Cu(111)

XPS measurements were performed for H2Pc on Cu(111). The molecular coverage is determined to be 0.7 ML. Figure 5.28 shows XP spectra of the C 1s and N 1s core-levels. The binding energy of the N 1s peak is $E_B = 399.1$ eV. The C 1s peak was fitted with two contributions, which originate from the C–C and C–N bondings. Their binding energies are $E_B^{C-N} = 286.3$ eV and $E_B^{C-C} = 285.1$ eV, respectively. The intensity ratio of both peaks, $I(C-C)/I(C-N)$ was determined to be 3.15, close to the theoretical value of $24/8 = 3$.

5.8.3 XSW measurements of H2Pc on Cu(111)

The XSW analysis – a representative XSW scan in displayed in Figure 5.29 – revealed an average bonding distances of 2.45 ± 0.07 Å for the carbon atoms and 2.39 ± 0.06 Å for the nitrogen atoms.

5.8.4 Discussion

The bonding distance of the metal-free Pc is smaller than the one reported for CuPc on Cu(111). At a comparable coverage (0.6 ML) the carbon and nitrogen atoms of CuPc

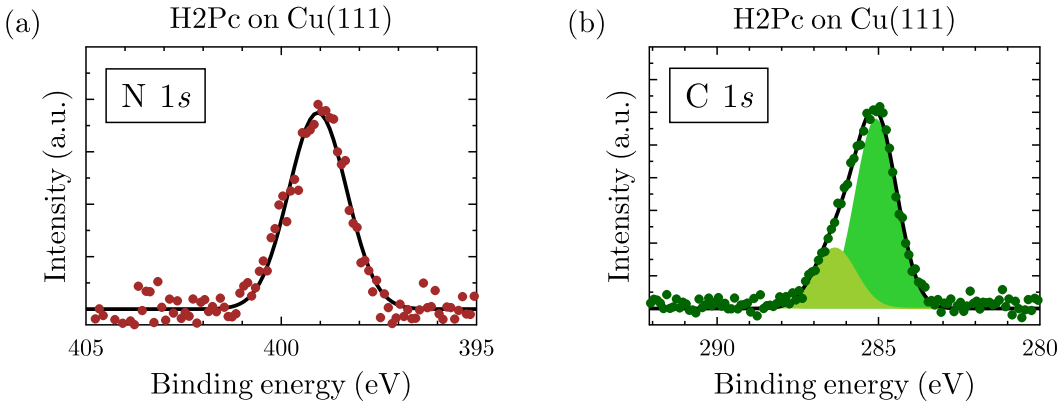

Figure 5.28: XP spectra of (a) N 1*s* and (b) C 1*s* core-level, taken at photon energies ~ 5 eV above E_{Bragg}. The asymmetric C 1*s* peak could be fitted best with two Gaussians.

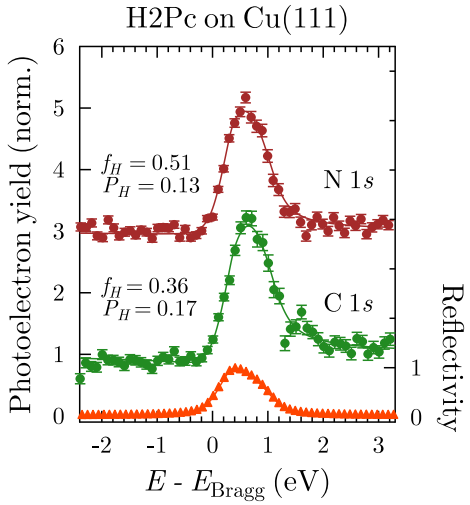

Figure 5.29: Exemplary reflectivity (triangles) and photoelectron yield curves (circles) of H2Pc on Cu(111) with the fitting parameters f_H and P_H for the yield curves of the nitrogen (upper yield curve) and carbon (lower yield curve) atoms.

have bonding distances of 2.57 Å and 2.48 Å, respectively [86]. The the result of an XSW study of H2Pc on Ag(111) revealed a significantly larger bonding distance for the carbon (3.04 Å) and nitrogen atoms (2.81 Å) at 0.7 ML coverage [86]. However, one has to bear in mind that silver atoms are significantly larger than copper atoms. To compare bonding distances between different substrates and to related them to the interaction strength, one can normalize the bonding distance to the sum of vdW radii of a substrate and carbon atom [86]:

$$d_{\mathrm{C}} = \frac{d_H}{r_{\mathrm{C}}^{\mathrm{vdW}} + r_{\mathrm{sub}}^{\mathrm{vdW}}} \tag{5.2}$$

The case $d_{\mathrm{C}} = 1$ represents pure vdW interaction, while for the other limiting case, a covalent bond, $d_{\mathrm{C}} = 0.66$ and $d_{\mathrm{C}} = 0.63$ are obtained for Cu(111) and Ag(111), respectively. The covalent radii are taken from Ref. [118]. To put these two extremal cases to 1 and 0, respectively, we extend the normalization:

$$d_{\mathrm{norm}} = \frac{d_{\mathrm{C}} - d_{\mathrm{C}}^{\mathrm{cov}}}{d_{\mathrm{C}}^{\mathrm{vdW}} - d_{\mathrm{C}}^{\mathrm{cov}}} \tag{5.3}$$

Now, for a bonding distance that is equal to the sum of the vdW radii we get $d_{\mathrm{norm}} = 1$. If the bonding distance equals the sum of the covalent radii, we obtain $d_{\mathrm{norm}} = 0$. The calculations of the normalized bonding distance should be regarded as a possibility to compare bonding distances on different substrates. For H2Pc on Cu(111) $d_{\mathrm{norm}} = 0.32$ was

Table 5.7: Comparison of carbon bonding distances of H2Pc and CuPc on Cu(111) and Ag(111), normalized to the sum of the substrate and carbon vdW radii. The values for H2Pc on Ag(111), CuPc on Cu(111), and CuPc on Ag(111) are taken from the literature. The vdW radii are extracted from Ref. [18].

	H2Pc			CuPc		
	d_H (Å)	d_{C}	d_{norm}	d_H (Å)	d_{C}	d_{norm}
Cu(111)	2.45	0.77	0.32	2.57	0.81 [86]	0.44
Ag(111)	3.04	0.87 [117]	0.65	2.99	0.86 [19]	0.62

obtained, while these values increase for CuPc on Cu(111), 0.44, and H2Pc on Ag(111), 0.65, as can be seen in Table 5.7. Clear indications were found that CuPc is chemisorbed on Cu(111) [85]. Therefore, the – compared to CuPc – even smaller normalized bonding distance indicates a strong, chemisorptive interaction between H2Pc and Cu(111). Indeed, molecular local DOS at the Fermi edge was found for H2Pc on Cu(111), leading to a metallic behavior of the first molecular layer [119].

5.9 TPP on Cu(111)

5.9.1 Introduction

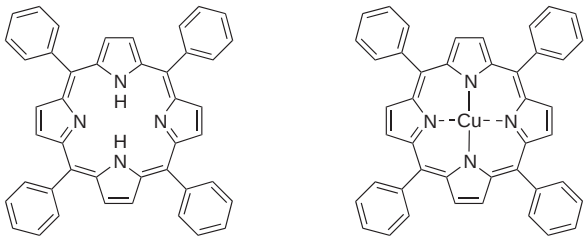

Figure 5.30: Molecular structure of 2HTPP (left) and CuTPP (right).

Similar to Pcs, porphyrins are very promising compounds as they can be chemically modified to a large extent. The center can host a metal atom, and side groups can be attached. For instance, by adding four phenyl group we obtain 2H-tetraphenylporphyrin (2HTPP, $C_{44}H_{30}N_4$, molecular structure shown in Figure 5.30), but also more complicated structures are possible. A few years ago, different studies reported the metalation at room temperature (RT) of 2HTPP on Ag(111) by coadsorption of Co [121, 122] and Fe [123] atoms. The first self-metalation of a porphyrin on a metal substrate was observed rather recently for protoporphyrin (H2PPIX) on Cu(110) and Cu(100) surfaces [124]. This behavior was later found, also at RT, for 2HTPP on Fe(111) and Ni(111) substrates [125]. Then, the thermally activated self-metalation of 2HTPP on Cu(111) to CuTPP + H_2 was reported [126] and different experimental techniques have been used to understand the process, which leads to changes in the geometric and electronic structure of this molecule [126, 127]. In X-ray photoelectron spectroscopy (XPS), the N 1*s* core-level of 2HTPP on Cu(111) consists of a double peak, which indicates that there are two different bonding mechanisms for the nitrogen atoms. The peak at higher binding energy is assigned to the two aminic nitrogen atoms (–NH–, in literature also assigned as *pyrrolic* nitrogen), while the other peak corresponds to the iminic nitrogen atoms (–N=) [122]. Compared to a multilayer 2HTPP film, the binding energy of the iminic nitrogen atoms in a monolayer on Cu(111) is lowered by 0.65 eV [128], which is explained by strong interaction of the iminic nitrogen atoms with the Cu(111) surface. After annealing to 500 K, the XP spectrum of N 1*s* changes substantially and only one N 1*s* peak is visible [126]. This result is explained by self-metalation, i.e. the formation of CuTPP [126], which involves the removal of an H_2 molecule and causes all nitrogen atoms to be equally coordinated to the central metal atom, as shown in Figure 5.30. This means that it is possible by annealing to transform the metal-free TPP to a TPP with a central metal atom.

Besides the electronic changes, STM pictures of 2HTPP and CuTPP on Cu(111) reveal irreversible structural changes upon heating to 500 K [127]. While at RT individual 2HTPP molecules can be imaged with STM due to the strong interaction of the iminic nitrogen atoms with the Cu(111) surface, this is not possible for the self-metalated CuTPP molecules

because of their high mobility on the Cu(111) surface. Instead, only at 200 K the diffusion of the molecules was slowed down sufficiently to enable STM measurements. Therefore, this system offers a relatively easy way to study the bonding distance of TPP to the substrate surface with and without a central metal ion, and to shed light on the influence of the central metal ion on the interaction strength between COM and metal.

Here we use the X-ray standing wave (XSW) technique to study 2HTPP and the self-metalated CuTPP on Cu(111) at different temperatures. In recent years the XSW technique has demonstrated its potential to disentangle the complex bonding mechanism of large aromatic molecules on noble metal surfaces [12, 15, 61, 74, 76, 79, 85, 129]. Details of the XSW technique can be found in Refs. [38, 39, 42]. Our study provides new insight into the influence of the central metal atom on the adsorption geometry of π-conjugated molecules on metal surfaces.

5.9.2 XPS measurements of TPP on Cu(111)

The XPS analysis of the N 1*s* and C 1*s* core-level signals of TPP on Cu(111) are displayed in Figure 5.31 and 5.32, respectively, which are arranged as follows: The uppermost spectra were recorded on a fresh spot on the sample (labeled "before XSW scan", the central spectra were taken after an XSW measurement ("after XSW scan"), and the bottom panels show spectra measured after annealing to 500 K. Each spectrum is background subtracted (Shirley background for the C 1*s* and linear background for the N 1*s*) and fitted with two Gaussians. The difference of the Bragg energy was used to determine the LT to be 146 K.

XPS measurements of the N 1*s* signal

As expected from previous work [122, 127, 128], the N 1*s* signal consists of two contributions, one from the aminic and the other from the iminic nitrogen atoms. The latter interacts more strongly with the copper atoms in the substrate surface. The expected intensity ratio of the two contributions is 1:1, but we measured a weaker aminic component and noticed a continuous change of the intensity ratio due to exposure to X-ray radiation, causing the aminic component to diminish and the iminic component to grow as can be clearly seen in Figure 5.31 at both RT and LT. The total N 1*s* was found to stay constant during the exposure. Note that the two spectra in the middle were taken after different X-ray exposure times. Therefore, the difference in height of the aminic peak is not due to the different sample temperatures, but rather due to different exposure times. Upon heating the sample to 500 K, only one peak N 1*s* remains due to the bond of all nitrogen to the Cu atoms, as observed previously [126].

Our measured binding energies for the iminic and aminic nitrogen atoms stay constant within the error bars: 398.3 eV and 399.9 eV, respectively. After annealing the single nitrogen peak is located at 398.4 eV. They are in good agreement with previously determined binding energies [126, 127]. No noticeable change in binding energy is observed upon cooling or annealing. All binding energies are summarized in Table 5.8. Similarly, no variation beyond our error bars is found for the widths (FWHM) of the individual N 1*s* peaks, being around 0.9 eV.

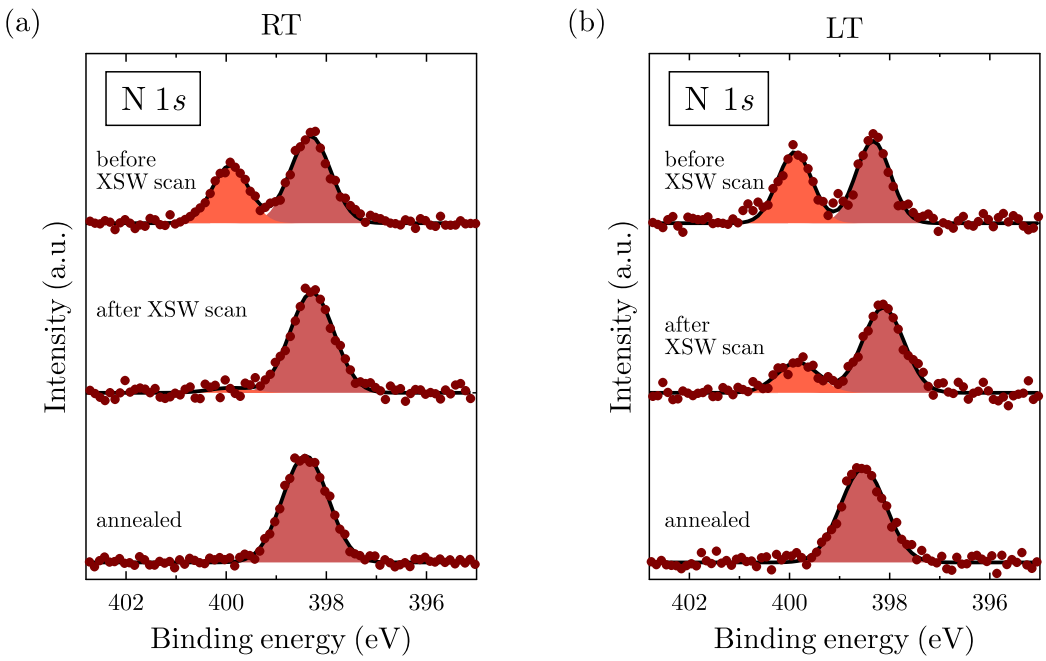

Figure 5.31: XPS analysis of the N 1*s* core-level signal of 2HTPP on Cu(111). We observed spectral changes for the N 1*s* signal due to synchrotron radiation. Therefore, spectra are shown for a fresh spot ("before XSW scan"), for a spot exposed to X-rays ("after XSW scan"), and for the annealed sample, both for RT and for LT. The vanishing aminic N 1*s* is related to metalation to CuTPP upon illumination of X-rays with energy $h\nu = 2.98$ keV.

XPS measurements of the C 1*s* signal

The asymmetric shape of all C 1*s* signals is fitted with two Gaussians with the constraint of having the same width. The higher binding energy component originates from the carbon atoms that form bonds with the nitrogen, while the lower binding energy one accounts for those forming bonds with other carbon an/or hydrogen atoms. For all sample conditions (RT, LT, and annealed), the intensity ratio of the two peaks, $I(\mathrm{C}-\mathrm{C})/I(\mathrm{C}-\mathrm{N})$ agrees with the expected value of 4.5 within a variation of ± 0.2.

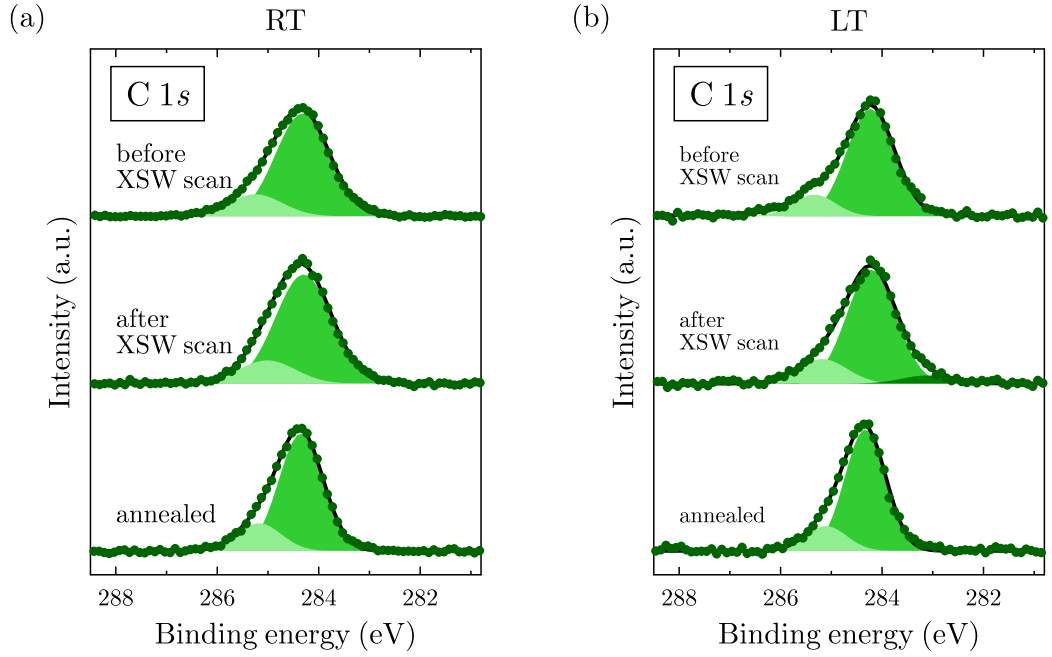

Figure 5.32: XPS analysis of the C 1*s* core-level signal of 2HTPP on Cu(111). Spectra are shown for a fresh spot ("before XSW scan"), for a spot exposed to X-rays ("after XSW scan"), and for the annealed sample, both for RT and for LT. No substantial change in the C 1*s* spectra indicate that molecule stays intact upon X-ray illumination. The vanishing peak correlated with the aminic nitrogen atoms can be explained by the metalation of the 2HTPP molecule to CuTPP induced by X-rays.

The binding energy of the stronger component (carbon surrounded by other carbon) is 284.3 eV. The weaker component (carbon atoms bound to also nitrogen atoms) is found to be at a binding energy of 285.2 eV. The width of the peaks changes only slightly. The FWHM is found to be 1.3 eV, 1.1 eV and 1.0 eV for 2HTPP/CuTPP measured at LT, RT and the annealed sample, respectively. All binding energies are summarized in Table 5.8.

5.9.3 Corrections of XSW measurements of 2HTPP on Cu(111)

The change of the N 1*s* spectra upon thermal annealing to 500 K has been explained by self-metalation of the 2HTPP molecule forming CuTPP [126]. Here, we observed a similar behavior induced by X-rays of 2.98 keV. The fact that the C 1*s* signal does not change

Table 5.8: Binding energies for C 1*s* and N 1*s* core-level signal of TPP on Cu(111) for different situations: Measured on a fresh spot ("before"), after an XSW measurement ("after") and for the annealed sample. All values in units of eV.

	RT			LT		
	before	after	annealed	before	after	annealed
N 1*s* (iminic)	398.3	398.3	–	398.3	398.2	–
N 1*s* (aminic)	399.9	399.9	–	399.9	399.8	–
N 1*s* (N–Cu)			398.4			398.5
C 1*s* (C–C)	284.3	284.3	284.4	284.2	284.2	284.3
C 1*s* (C–N)	285.3	285.0	285.2	285.4	285.2	285.1

during exposure of X-rays supports the occurrence of a beam induced chemical reaction from 2HTPP to CuTPP and rules out beam damage as the cause of the nitrogen core-level changes, because in the latter case the molecules would have been destroyed upon X-ray illumination.

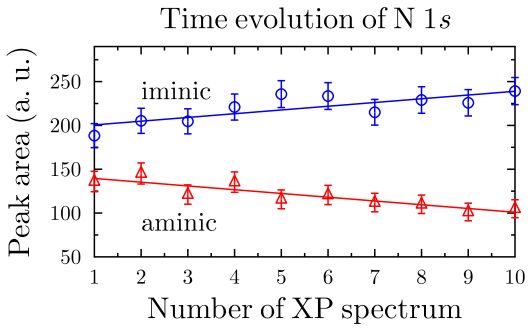

Figure 5.33: Time evolution of the N 1*s* peak upon illumination of hard X-rays. Ten spectra were taken one after another. The depicted range of the x-axis corresponds to ~ 25 min. After background subtraction each peak was integrated to obtain the area of the aminic and iminic component. The gradient of the two best-fit lines reveal similar values of opposite sign, evidencing the chemical reaction from 2HTPP to CuTPP.

As this chemical reaction changes the intensities of the two N 1*s* components, the XSW-modulated photoelectron yields are affected. To account for the changing N 1*s* intensities due to this beam induced chemical reaction we applied a correction to the yield curves. An XP spectrum before and after an XSW scan and the time between the two spectra were used to determine the reaction rate. A linear slope with a gradient of the reaction rate (as shown in Figure 5.33) was subtracted from the iminic photoelectron yield and added to the aminic one. The result of this correction can be seen in Figure 5.34. The uncorrected yield curves are displayed in Figure 5.34(a), where the measured iminic N 1*s* yields are mostly below (above) the best fit at the start (end) of the scan, which is on the

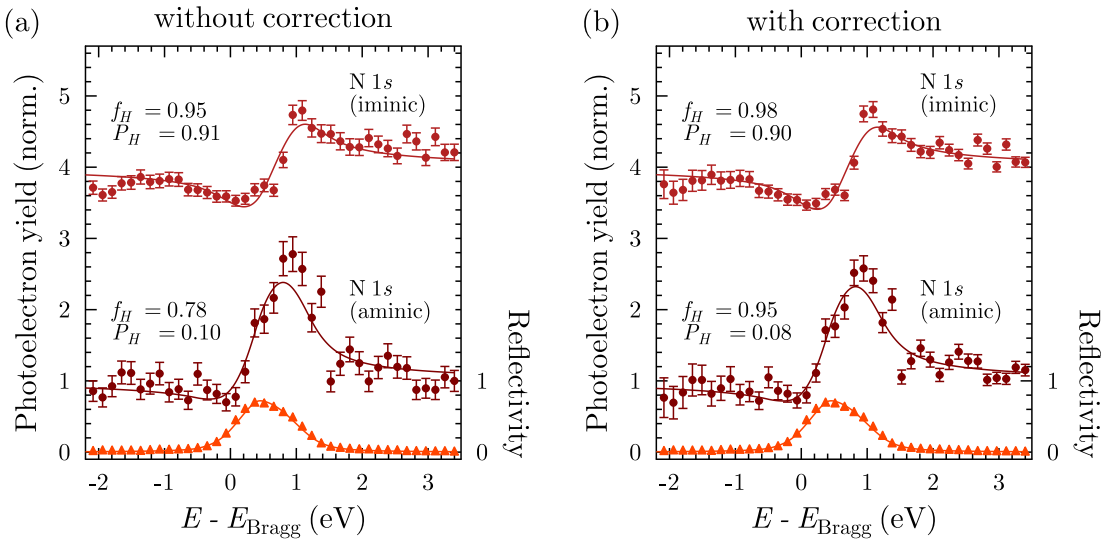

Figure 5.34: Exemplary reflectivity (triangles) and photoelectron yield curves (circles) of 2HTPP on Cu(111) with the fitting parameters f_H and P_H for the yield curves of the N 1*s* signal, measured at LT. (a) Not corrected yield curves for the aminic and iminic nitrogen atoms. (b) A linear correction was added (subtracted) to the yield curves of the aminic (iminic) nitrogen atoms in order to account for the metalation of 2HTPP upon X-ray illumination.

left (right) of the plot. The opposite can be observed for the yield curve of the aminic nitrogen. Figure 5.34(b) displays the corrected yield curves, where one can see a better agreement with the best fit due to the correction. This correction leads to changes of the coherent positions of the order of $\Delta P_H \leq 0.02$, and coherent fractions of $\Delta f_H \leq 0.2$.

5.9.4 XSW measurements of 2HTPP on Cu(111)

Several XSW measurements were performed for the C 1*s* and N 1*s* core-levels at RT and LT. All aminic and iminic N 1*s* photoelectron yields were corrected as described in the previous section. Note that the numbers given below refer to the average over all individual results of one species, while in Figure 5.35 and Figure 5.36 one single XSW measurement is shown.

At RT, the analysis of the N 1*s* photoelectron yield reveals for the aminic nitrogen atoms a bonding distance to the Cu(111) surface of 2.23 Å and for the iminic nitrogen 2.02 Å. The average carbon bonding distance is 2.40 Å. At LT, small changes are observed for the aminic nitrogen atoms (2.28 Å), iminic nitrogen atoms (1.97 Å), and carbon atoms (2.34 Å). All results are summarized in Table 5.9.

5.9.5 XSW measurements of CuTPP on Cu(111)

After annealing the sample to 500 K, 2HTPP was transformed to CuTPP. Several XSW measurements were performed for the new system at RT and LT, one of those is displayed

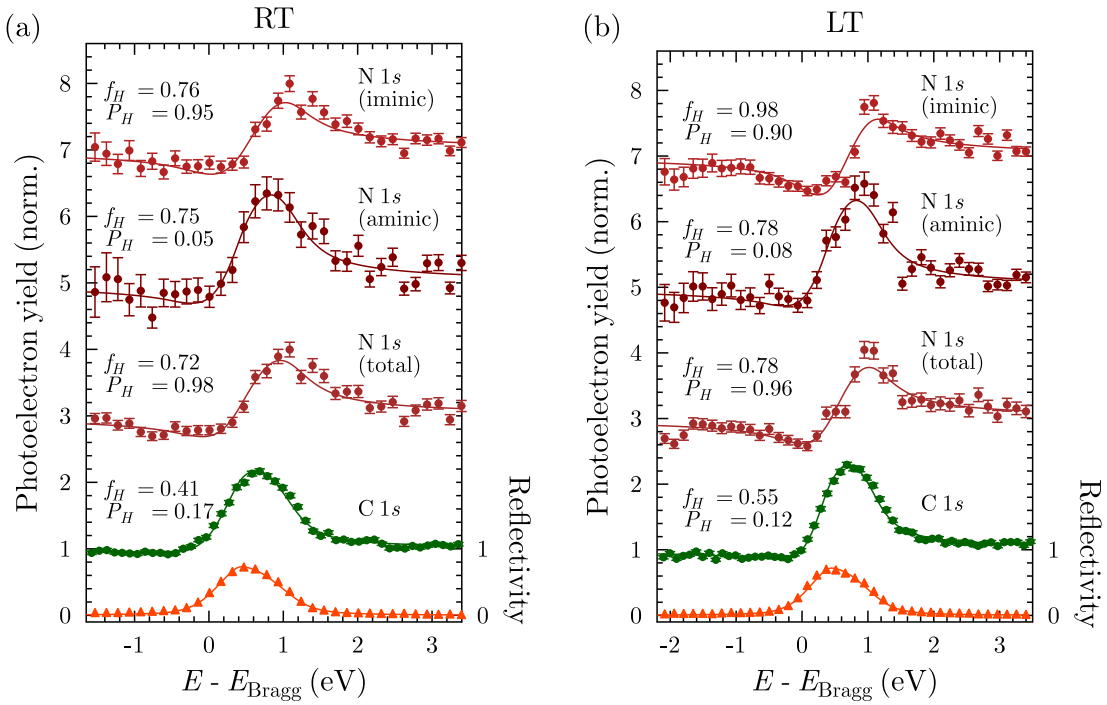

Figure 5.35: Exemplary reflectivity (triangles) and photoelectron yield curves (circles) of 2HTPP on Cu(111) with the fitting parameters f_H and P_H for the yield curves of the C 1s and N 1s signals at RT and LT. The N 1s yield curves of the aminic and iminic nitrogen atoms are corrected as described in the previous section.

Table 5.9: Average XSW results (coherent fraction, coherent position, bonding distance) of 2HTPP on Cu(111) at RT and LT. The results of the aminic and iminic nitrogen atoms were obtained performing the correction method described earlier.

	RT			LT		
	f_H	P_H	d_H (Å)	f_H	P_H	d_H (Å)
N 1s (iminic)	0.67	0.97	2.02 ± 0.08	0.84	0.94	1.97 ± 0.08
N 1s (aminic)	0.72	0.07	2.23 ± 0.05	0.85	0.09	2.28 ± 0.05
N 1s (total)	0.61	0.03	2.15 ± 0.08	0.70	0.98	2.04 ± 0.06
C 1s (total)	0.52	0.15	2.40 ± 0.03	0.65	0.12	2.34 ± 0.02

in Figure 5.36 for both temperatures. The carbon atoms are found to adsorb on average at a distance of 2.38 Å (RT) and 2.33 Å (LT) to the Cu(111) surface. The average distance

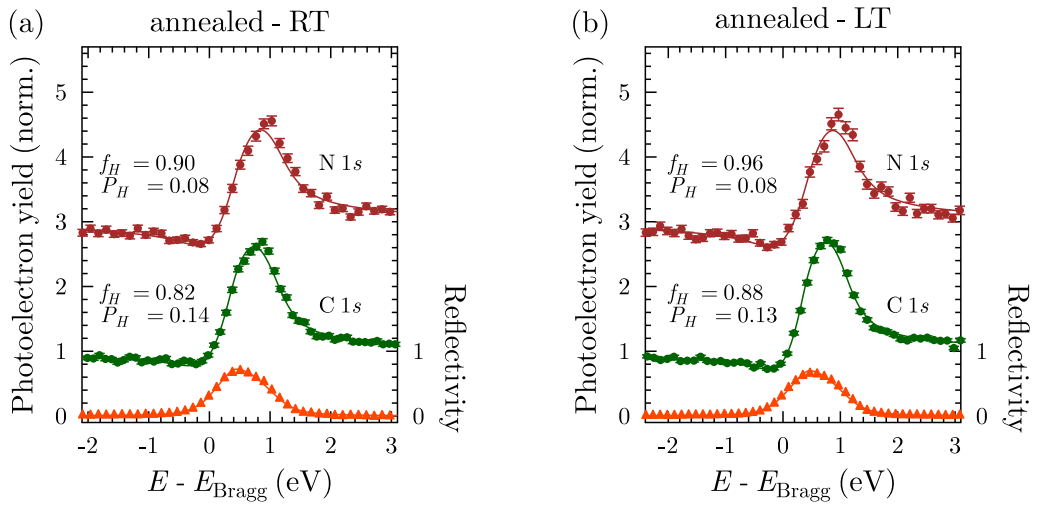

Figure 5.36: Exemplary reflectivity (triangles) and photoelectron yield curves (circles) of CuTPP on Cu(111) with the fitting parameters f_H and P_H for the yield curves of the C 1s and N 1s signals at RT and LT.

for the nitrogen atoms is determined to be 2.25 Å at both RT and LT. All results of the annealed sample are summarized in Table 5.10.

Table 5.10: The average values of several XSW measurements are displayed here as final result (coherent fraction, coherent position, bonding distance) of 2HTPP on Cu(111) at RT and LT.

	RT			LT		
	f_H	P_H	d_H (Å)	f_H	P_H	d_H (Å)
N 1s	0.90	0.08	2.25 ± 0.02	0.93	0.08	2.25 ± 0.02
C 1s (total)	0.71	0.14	2.38 ± 0.02	0.84	0.12	2.33 ± 0.02

5.9.6 Discussion

The chemical reaction of 2HTPP on Cu(111) to CuTPP has an influence on the bonding distance to the substrate. As expected, the two types of nitrogen atoms, the aminic nitrogen atom (with a N–H bond) and the iminic nitrogen atoms, which strongly interact with the Cu(111) substrate, adsorb at different distances to the Cu(111) surface. At RT, the rather small bonding distance of the iminic nitrogen (2.02 Å) supports the earlier finding of a strong interaction between nitrogen and the substrate involving an covalent bond. The

bonding distance of the aminic nitrogen atom is ~ 0.2 Å larger (2.23 Å). These different distances signify a saddle-shape of the porphyrin ring. This geometry was also found using near edge X-ray absorption fine structure (NEXAFS) spectroscopy [126] of 2HTPP on Cu(111) and by density functional theory (DFT) calculations of the reaction of porphyrin with single metal atoms, including Cu [122].

The average distance of the carbon atoms of 2HTPP (2.40 Å at RT) suggests that the phenyl groups, which can rotate around the axis of the bond to the porphyrin core, adsorb rather parallel to the surface. Another finding that supports this statement are the relatively high coherent fractions for the carbon atoms, which clearly indicate an essentially flat-lying molecule, including its phenyl groups. This finding is in line with other experimental results: NEXAFS measurements determined an inclination angle of the phenyl groups of 20° [126], and a tilt angle of only 10° [130] was estimated based on STM measurements.

This adsorption scenario is qualitatively the same both for RT and LT. As observed before in XSW studies at different temperatures (see, e.g., Refs. [91, 117]), the coherent fractions are higher at lower temperatures, most likely due to a smaller vibrational amplitude.

Upon annealing of 2HTPP and the thereby induced chemical reaction to CuTPP, a change of the bonding distance of the nitrogen atoms was observed. Now one nitrogen peak in the N 1*s* spectrum is observed. This finding is explained by a bond formation between all nitrogen atoms and the central copper atom, which is removed from the surface. For CuTPP all nitrogen atoms adsorb at a bonding distance of 2.25 Å to the Cu(111) surface. The formerly iminic nitrogen atoms of 2HTPP are lifted upon metalation by 0.2 Å. This increase can be an explanation for STM findings, where the mobility of CuTPP is higher compared to 2HTPP, due to a weaker interaction of the nitrogen atoms with the substrate. All nitrogen atoms at the same distance to the Cu(111) surface signifies that we have a flat porphyrin ring for the metalated molecule in accordance with results from NEXAFS measurements [126]. The average distance of the carbon atoms remains basically unaffected (2.38 Å at RT) from the chemical reaction.

The two different distances of the carbon and nitrogen atoms represent a distorted CuTPP molecule. Assuming a flat macrocycle, which is oriented parallel to the surface (at a distance of 2.25 Å), the different adsorption heights of nitrogen and carbon atoms must base on a larger average distance of the phenyl groups compared to the carbon atoms within the porphyrin ring. A larger distance to the surface can be achieved by an upward bending of the phenyl groups, as it is depicted in Figure 5.37. To obtain the experimentally determined mean carbon distances of 2.38 Å, the average distance of the phenyl groups, marked by a cross in Figure 5.37, to the surface has to be 2.48 Å. This value is consistent with a bending of the phenyl groups of 5°. Note that the influence of the bending of the phenyl groups is independent on their tilt angle. The fact that the average bonding distance of the carbon atoms does not change implies that in 2HTPP the strong interaction between the iminic nitrogen and the Cu surface cannot be responsible for the small distance of the carbon backbone to the surface, as the metalation weakens the former without affecting the latter. Although the annealing does not influence the adsorption distances of the TPP

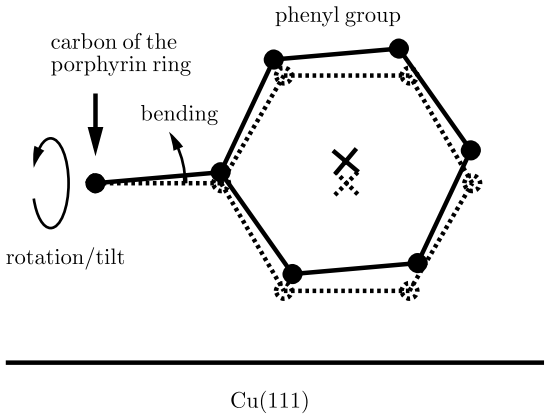

Figure 5.37: Schematic picture showing the bending by 5° of a phenyl group of CuTPP, resulting in an mean distance of the phenyl groups of 2.48 Å. The displayed tilt angle is arbitrarily chosen, as the average distance of the phenyl group, marked by a cross, is not affected by the tilt angle. NEXAFS data of CuTPP on Cu(111) revealed a tilt angle of the phenyl groups of $40° - 50°$ [126].

molecule, the vertical order is clearly affected, as one can see from the increase of the coherent fractions for both the carbon and the nitrogen atoms.

We now compare the CuTPP molecule with Cu-phthalocyanine (CuPc) on Cu(111), which has been studied by XSW in great detail at different submonolayer coverages and temperatures (300 K and 183 K) [86]. It is shown that CuPc on Cu(111) does not show a temperature dependent adsorption distance, in line with our results of CuTPP. Instead, for CuPc on Cu(111) a dependence of the bonding distance on the coverage was detected. We compare therefore our values with the results for 0.9 ML of CuPc, which is close to our coverage of CuTPP (0.8 ML). The distance to the Cu(111) surface for CuPc (d_H(C) = 2.79 Å and d_H(N) = 2.69 Å) is larger than for CuTPP, where the d_H(C) = 2.38 Å, and d_H(N) = 2.25 Å. Qualitatively the two molecules adsorb in a similar way on the Cu(111) surface, with the nitrogen atoms at lower distances to the surface. Yet, the CuTPP molecule is by $\sim$ 0.4 Å considerably closer to the surface, and therefore interacting stronger with the surface than CuPc.

H2Pc on Cu(111) was presented in Section 5.8. The bonding distance of the carbon atoms is very similar for the H2Pc an the 2HTPP molecule, at $\sim$ 2.4 Å. However, the nitrogen atoms in the 2HTPP molecule adsorbs at smaller bonding distances compared to the nitrogen atoms in the H2Pc atom. There, a average bonding distance of $d_H(N) = 2.39$ Å on Cu(111) was determined. Apparently the iminic nitrogen atoms of the TPP molecule make the difference. Their strong, chemical interaction with the substrate is visible in XPS by a chemical shift of 0.6 eV compared to the multilayer signal and in XSW by means of a very small bonding distance (2.02 Å and 1.97 Å at RT and LT, respectively).

In conclusion, we find evidence for a strong interaction between metal-free and metalated TPP molecule with the Cu(111) substrate. The distance of the carbon atoms to the Cu(111) surface before and after the metalation is very similar, showing a flat-lying

molecule. For 2HTPP, the bonding distance of the two types of nitrogen atoms reveal a distorted porphyrin ring toward a saddle-shape, which becomes flat upon metalation as all four nitrogen atoms are now involved in the bond to the central Cu atom in the same way. No changes in the bonding distance was observed for RT and LT, neither for the 2HTPP nor for CuTPP. Beside the thermally activated self-metalation we detected a self-metalation induced by hard X-rays.

5.10 VOPc on Cu(111)

5.10.1 Introduction

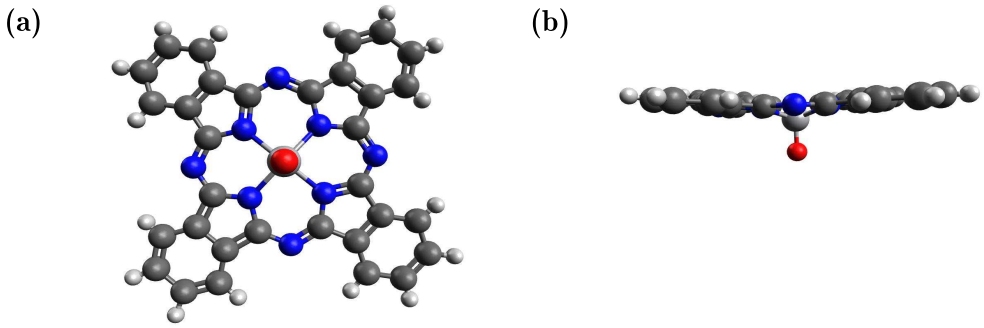

Figure 5.38: Molecular structure of VOPc in (a) top view and (b) side view, with the oxygen atom (red) pointing downwards (O-down). The carbon atoms are displayed in black, the nitrogen atoms in blue, and the hydrogen atoms in light gray.

In contrast to H2Pc, vanadium(IV) oxide phthalocyanine (VOPc, $C_{32}H_{16}VON_8$) is a non-planar molecule, where the vanadium-oxygen bond is perpendicular to the tetraazaporphyrin ring, hence the oxygen atom (and even slightly the central vanadium atom) is protruding from the phthalocyanine macro-cycle, whose four carbon lobes are bent slightly in the other direction, as shown in Figure 5.38. For such a non-planar molecule the fundamental question arises, whether it adsorbs in an oxygen (O)-down or oxygen (O)-up position. The orientation of the intrinsic dipole along the V–O axis influences the charge transport through the interface. Such a question was addressed before to GaClPc on Cu(111). An XSW study revealed that the GaClPc adsorbs in the chlorine-down position, decreasing the work function of the metal-organic compound [79].

In a recent study, the adsorption geometry of VOPc on Au(111) was investigated using the photoelectron diffraction (PhD) technique [131]. They revealed that the VOPc molecule adsorbs in the O-up configuration on Au(111), and the carbon backbone with the vanadium atom in the center is flattened. These molecular changes of the shape compared to its geometric structure in the crystalline phase was rationalized with interaction between the VOPc molecule and the Au(111) surface.

Our aim was to elucidate the bonding of the non-planar VOPc molecule on the Cu(111) surface with the XSW technique. The bonding distance of the different chemical species within the VOPc molecule can give rise to the molecular conformation and, at the end, also to the interaction of VOPc with the Cu(111) surface.

5.10.2 XPS measurements of VOPc on Cu(111)

The XPS measurements of VOPc revealed binding energies of the two contributions of C 1s at $E_B^{C-N} = 285.2$ eV and $E_B^{C-C} = 284.0$ eV and of N 1s at $E_B = 398.3$ eV. The O 1s

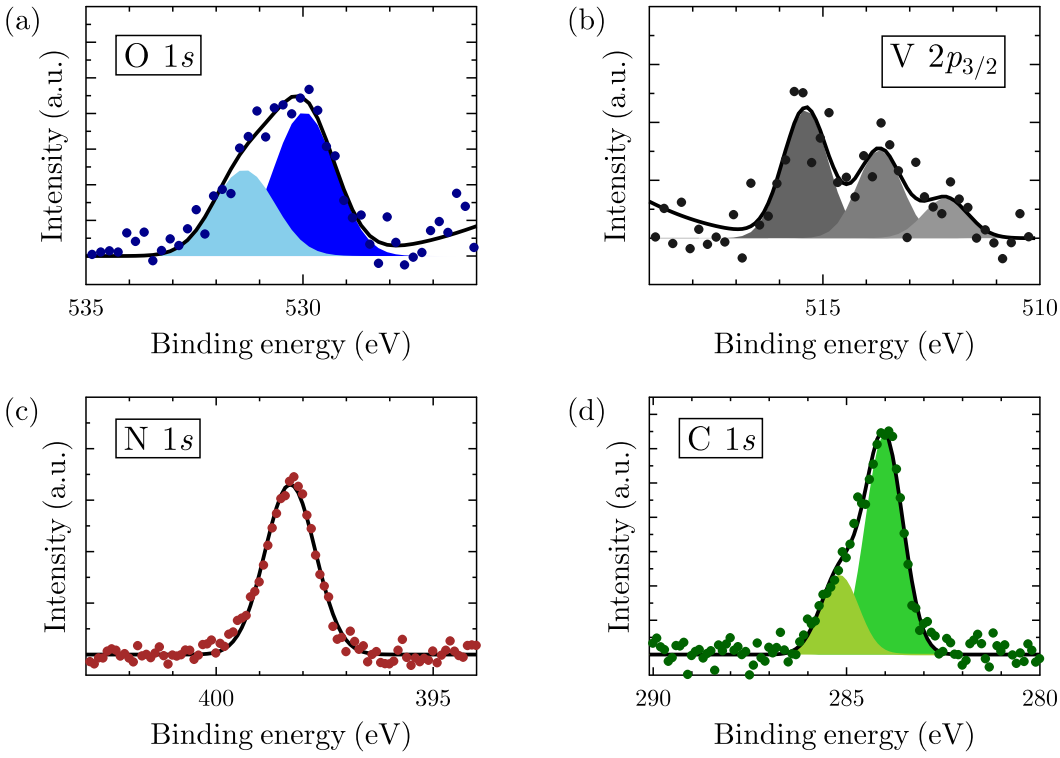

Figure 5.39: XP spectra of the components of VOPc on Cu(111): (a) O 1*s*, (b) V $2p_{3/2}$, (c) N 1*s*, and (d) C 1*s*.

and V $2p_{3/2}$ signals are relatively noisy due to the low number of oxygen and vanadium atoms (one atom each per molecule). The two components of the O 1s signal are located at 530.0 eV and at 531.4 eV. The V $2p_{3/2}$ signal is fitted with three components, at 512.2 eV, 513.7 eV, and 515.4 eV.

5.10.3 XSW measurements of VOPc on Cu(111)

Exemplary XSW scans, which represent well the average result, from the elements within the VOPc molecule are displayed in Figure 5.40, together with the corresponding fit results. The average coherent positions are $P_H = 0.30$ for C 1s, $P_H = 0.35$ for N 1s, $P_H = 0.38$

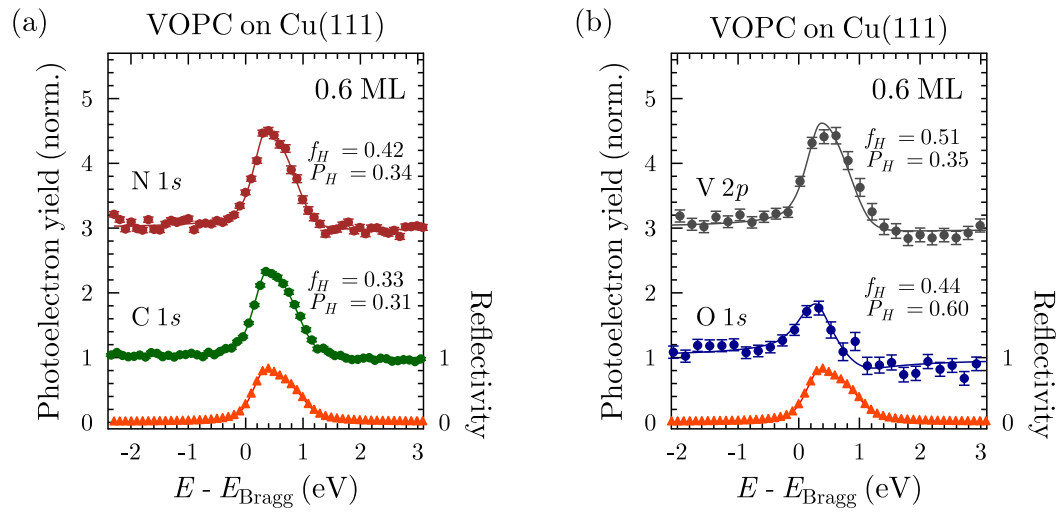

Figure 5.40: Reflectivity (triangles) and photoelectron yield curves (circles) of VOPc on Cu(111) with the fitting parameters f_H and P_H for the yield curves of the O 1s, V $2p_{3/2}$, N 1s, and C 1s atoms.

for V $2p$, and $P_H = 0.61$ for O 1s. An overview of the results is given in Table 5.12. The calculation of the bonding distances from the coherent positions is not trivial, as one has to consider the modulo-n ambiguity of the XSW formula $d_H = (n + P_H)d_0$. For the oxygen atom possible average bonding distances might be 1.28 Å ($n = 0$) or 3.36 Å ($n = 1$). The most likely bonding distance of the vanadium atom is 2.88 Å ($n = 1$).

To elucidate, which value of n has to be taken for each element in order to determine, whether the molecule adsorbs in the O-down or O-up position or in a combination of both, it is helpful to simulate XSW fit results using the structure of the molecule.

5.10.4 XSW simulations of VOPc on Cu(111)

The simulation of XSW fit results were performed using Formula 2.31 in a modified way, for each chemical species:

$$f_H e^{2\pi i P_H} = \frac{1}{N} \sum_{i=1}^{N} e^{2\pi i \ z_i/d_0}. \tag{5.4}$$

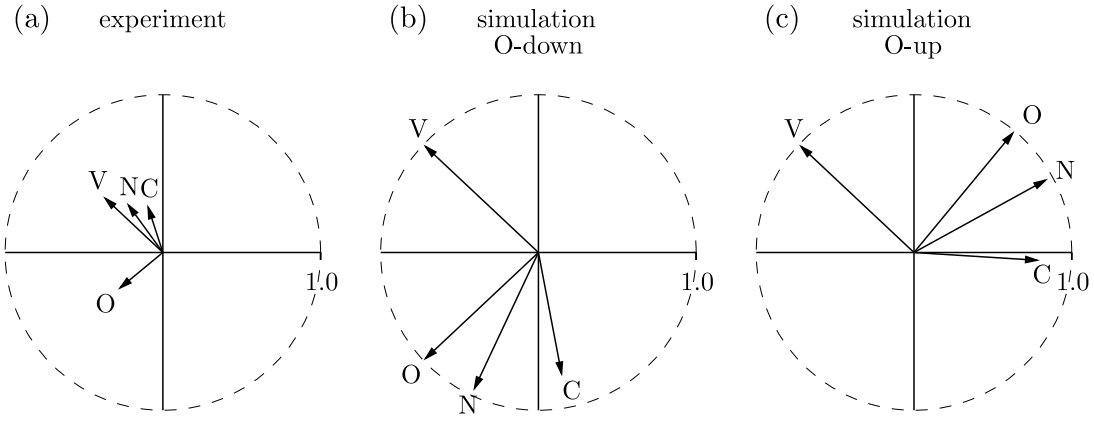

Figure 5.41: Argand diagram: (a) experimental XSW results. (b) and (c) displays simulated XSW results for VOPc in O-down and O-up orientation, respectively. For the simulations, the vanadium atom was put at experimentally determined position. The position of the remaining atoms were taken from the CSD, and the molecule was rotated until the V–O bond was aligned parallel to the surface normal of Cu(111).

N is the number of atoms of one element, z_i the height of the ith atom above the surface, and d_0 the lattice spacing of the substrate. The xyz-coordinates of the molecule, taken from the Cambridge Structural Database (CSD) of the Cambridge Crystallographic Data Centre [132], were used and the molecule was moved in a position, where the V–O bond is along the z axis (O-up), which we define as being parallel to the substrate normal. Rotation by 180° resulted in the O-down orientation. The z-offset is chosen such that the

Table 5.11: P_H values of the experimental results, and of simulations based on the molecular structure of VOPc, obtained from the CSD database. Two scenarios are simulated, the O-up and O-down orientation of VOPc. The P_H values correspond to the angles of the vectors divided by 2π in the Argand diagram in Figure 5.41.

	Experiment	Simulations	
		O-down	O-up
Atom	P_H	P_H	P_H
V $2p$	0.38	0.38	0.38
O $1s$	0.61	0.62	0.14
N $1s$	0.35	0.68	0.99
C $1s$	0.30	0.77	0.08

vanadium atom is at the experimentally determined bonding distance. The results of the simulations of the remaining atoms can then be taken for comparison with the experiment. An overview of the simulated results of VOPc on Cu(111) in O-down and O-up orientation is given in Table 5.11. For the sake of clarity, only the P_H values are listed.

5.10.5 Discussion

Comparing the experimental results with the simulations we see that neither the O-up nor the O-down orientation agrees for all atoms. For the O-up orientation none of the remaining atoms agree with experiment. For the O-down orientation, the simulations (1.58 Å) reproduce almost exactly the experimental result of the V–O bond length (1.60 Å). This conformity is expressed in the Argand diagram in Figure 5.41 by the same angles of the vectors representing the vanadium and oxygen atoms. However, for this orientation, no agreement for the nitrogen and carbon atoms is achieved. Even a combination of O-up and O-down VOPc molecules with the geometry from the database does not yield an agreement with experiment. A combined O-up and O-down orientation might be suggested by the XPS analysis of the O 1*s* signal. The oxygen atoms in the O-up and O-down orientation have different surroundings, leading to two components in the XPS signal. In the Argand diagram combinations of both orientations can be imagined by vector addition. Let us assume half of the molecules is adsorbed in O-up, the other half in O-down orientation, both with the vanadium atom at the same distance (experimentally determined value) to the substrate. We can see that the vectors of the oxygen atoms in Figure 5.41(b) and (c) almost cancel each other out, because they are opposing each other. The vector length is related to the coherent fraction, which in this case would be almost zero. The resulting nitrogen and carbon atoms share the same resulting vector, due to symmetrical reasons. This vector is pointing in opposite direction to the vector of the vanadium atom. This finding does not represent the experimental result at all, neither do simulations with other mixing ratios of O-up and O-down molecules match the experiment.

A probable way out of the dilemma could be a different molecular geometry than that from the database. A bending of the phthalocyanine lobes was reported for many Pcs, and this phenomenon can also occur for VOPc. One can imagine especially in the O-down orientation a strong bending of the lobes toward the Cu(111) surface. This molecular distortion would lower the P_H of the nitrogen and carbon atoms compared to the molecular structure from the CSD. A bending of the lobes was reported for AlClPc on Cu(111) [133] and for CoPc [134], involving a reduction of the molecular symmetry. All Pcs display a fourfold symmetry in the gas phase. If upon adsorption two opposite lobes of the molecule are bent in a different way compared to the other two lobes, reducing the symmetry from fourfold to twofold. Also for a computational study of CoPc on Cu(111), a bending of the lobes was found [135], accompanied with symmetry reduction of the molecule.

Table 5.12: XSW results, f_H and P_H, and proposed bonding distance of VOPc on Cu(111). The results are obtained by averaging several individual results.

Atom	f_H	P_H	d_H (Å)
V 2*p*	0.52 ± 0.07	0.38 ± 0.03	2.88 ± 0.07
O 1*s*	0.37 ± 0.04	0.61 ± 0.02	1.28 ± 0.04
N 1*s*	0.39 ± 0.04	0.35 ± 0.04	2.82 ± 0.08
C 1*s*	0.32 ± 0.05	0.30 ± 0.03	2.70 ± 0.06

To check the suggestion of a VOPc molecule, which adsorbs in O-down orientation we want to check now, if it is plausible to have a oxygen atom at a vertical distance of 1.28 Å above the first Cu(111) plane. The adsorption of (pure) oxygen on different copper surfaces was subject of various studies in the past. In an early study using the surface extended X-ray absorption fine structure (SEXAFS) technique, the nearest-neighbour O–Cu bond length was determined to be 1.83 Å [136]. This distance can be translated into a vertical distance of 1.1 Å for adsorption in a hollow site. They also found that the Cu(111) surface undergoes a reconstruction process upon adsorption of $\sim$ 0.5 ML of oxygen. In another investigation, using surface extended electron energy loss fine structure (SEELFS) technique, it was found that the oxygen atoms adsorb at a distance of 0.5 Å above the topmost Cu(111) layer [137]. This low bonding distance is explained by an increased lateral Cu–Cu distance due to reconstruction. This adsorption height was later confirmed by an XSW study [138]. Lastly, there are two studies of the adsorption geometry of methoxy species on Cu(111). A photoelectron diffraction study determined an oxygen adsorption height of 1.33 Å and adsorption in FCC hollow sites [139]. The XSW study of methoxy on Cu(111) yields an oxygen bonding distance of 1.3 Å [138]. There, the adsorption of oxygen occurs in a combination of fcc and hcp hollow sites. Both results are very close to our bonding distance of the oxygen atom of VOPc.

In summary, there are various studies reporting for oxygen atoms bonding distances of $\sim$ 1.3 Å above the topmost Cu(111) layer, both for single oxygen atoms and for molecules containing oxygen. These investigations support the possibility of VOPc adsorbed in the O-down orientation. Assuming conformational changes of the phthalocyanine skeleton, as it was reported in other studies, our measured P_H values of N 1s and C 1s become reasonable. Therefore we conclude that VOPc on Cu(111) adsorbs predominantly in the O-down orientation, with the oxygen atom at 1.28 Å, the vanadium atom at 2.88 Å, and the carbon and nitrogen atoms at a bonding distance of 2.82 Å and 2.70 Å, respectively, above the first Cu(111) layer. These adsorptions heights are listed in Table 5.12. However, to obtain a more complete picture of the adsorption of VOPc on Cu(111), further experimental techniques like STM might be helpful.

5.11 Overview of XSW results of COMs on (111) coinage metal surfaces

The following tables contain bonding distances of COMs on the Cu(111) [Table 5.13], Ag(111) [Table 5.16], and Au(111) [Table 5.19] surfaces that are found in the literature or presented in this work. This overview of what has been studied so far renders it possible to deduce general trends of the adsorption behavior. On the other hand, these tables may also display, which information is still lacking and how to proceed to get a more complete understanding of the various bonding phenomena of COMs on metal surfaces.

5.11.1 The Cu(111) surface

Table 5.13: XSW results of COMs on Cu(111).

Molecule	Comment	Orbital	f_H	P_H	d_H (Å)
PTCDA [13]		C 1s	0.50	0.26	2.61
		(O 1s)$_{\mathrm{anh}}$	0.48	0.28	2.89
		(O 1s)$_{\mathrm{carb}}$	0.18	0.31	2.73
DIP [61]	0.6 ML	C 1s	0.48(9)	0.20(1)	2.51(3)
H_2Pc	0.7 ML	C 1s	0.27(6)	0.18(4)	2.45(7)
		N 1s	0.46(5)	0.15(3)	2.39(6)
ZnPc [115]	0.7 ML	C 1s			2.49(3)
		N 1s			2.55(2)
		Zn 2$p_{3/2}$			2.25(5)
F_{16}ZnPc [115]		C 1s			2.66(10)
		N 1s			2.85(2)
		F 1s			3.15(9)
		Zn 2$p_{3/2}$			2.58(5)
GaClPc [79]	0.8 ML, Cl down	C 1s	0.23	0.14	4.44(7)
		N 1s	0.41	0.27	4.71(3)
		Ga 1s	0.51	0.03	4.21(5)
		Cl KLL	0.67	0.90	1.88(3)

Table 5.14: XSW results of COMs on Cu(111) (continuation).

Molecule	Comment	Orbital	f_H	P_H	d_H (Å)
CuPc [86]	0.4 ML, 300 K	C 1s	0.65(3)	0.268(4)	2.64(7)
		N 1s	0.74(3)	0.220(4)	2.54(7)
	0.6 ML, 300 K	C 1s	0.457(18)	0.232(5)	2.57(7)
		N 1s	0.43(5)	0.190(12)	2.48(7)
	0.9 ML, 300 K	C 1s	0.298(15)	0.337(7)	2.79(7)
		N 1s	0.45(3)	0.292(6)	2.69(7)
	0.4 ML, 183 K	C 1s	0.59(3)	0.258(5)	2.62(7)
		N 1s	0.68(4)	0.229(6)	2.56(7)
	0.6 ML, 183 K	C 1s	0.36(3)	0.214(7)	2.53(7)
		N 1s	0.49(9)	0.224(14)	2.55(7)
	0.9 ML, 183 K	C 1s	0.301(11)	0.352(5)	2.82(7)
		N 1s	0.56(3)	0.308(6)	2.73(7)
F_{16}CuPc	[11]	C 1s	0.50(1)	0.251(5)	2.61
		N 1s	0.30(1)	0.297(8)	2.70
		F 1s	0.31(1)	0.381(9)	2.88
	[116]	C 1s	0.299	0.285	2.68
		F 1s	0.435	0.543	3.21
VOPc	0.6 ML	C 1s	0.32(5)	0.30(3)	2.70(6)
		N 1s	0.39(4)	0.35(4)	2.82(8)
		V 2p	0.52(7)	0.38(3)	2.88(7)
		O 1s	0.37(4)	0.61(2)	1.28(4)
PEN [14]		C 1s	0.55	0.12	2.34(2)
PFP [14]		C 1s	0.41	0.42	2.98(7)
		F 1s		0.47	3.08(4)
P2O [84]		C 1s	0.16	0.12	2.34
		O 1s	0.17	0.94	2.02
P4O [84]		C 1s	0.23	0.07	2.25
		O 1s	0.22	0.95	1.98

Table 5.15: XSW results of COMs on Cu(111) (continuation).

Molecule	**Comment**	**Orbital**	f_H	P_H	d_H (Å)
PYT	0.9 ML	C 1*s*	0.35(3)	0.11(1)	2.31(3)
		O 1*s*	0.43(5)	0.97(2)	2.04(6)
COHON	0.4 ML	C 1*s*	0.25(5)	0.17(2)	2.45(4)
		O 1*s*	0.48(3)	0.03(1)	2.14(3)
2HTPP	0.8 ML, 294 K	C 1*s*	0.52	0.15	2.40(3)
		N 1*s* (aminic)	0.72	0.07	2.23(5)
		N 1*s* (iminic)	0.67	0.97	2.02(8)
	0.8 ML, 146 K	C 1*s*	0.65	0.12	2.34(2)
		N 1*s* (aminic)	0.85	0.09	2.28(5)
		N 1*s* (iminic)	0.84	0.94	1.97(8)
CuTPP	0.8 ML, 294 K	C 1*s*	0.71	0.14	2.38(2)
		N 1*s*	0.90	0.08	2.25(2)
	0.8 ML, 146 K	C 1*s*	0.84	0.12	2.33(2)
		N 1*s*	0.93	0.08	2.25(2)
F4TCNQ [140]		C 1*s*	0.11	0.32	–
		N 1*s*	0.20	0.29	2.7(1)
		F 1*s*	0.32	0.58	3.3(1)

5.11.2 The Ag(111) surface

Table 5.16: XSW results of COMs on Ag(111).

Molecule	Comment	Orbital	f_H	P_H	d_H (Å)
PTCDA	[12, 13, 74]	C 1s	0.52	0.21	2.86
		(O 1s)$_{\mathrm{anh}}$	0.46	0.27	2.97
		(O 1s)$_{\mathrm{carb}}$	0.62	0.14	2.68
	LT [76]	C 1s			2.80(2)
		(O 1s)$_{\mathrm{anh}}$			2.83(4)
		(O 1s)$_{\mathrm{carb}}$			2.49(4)
	300 K [141]	C 1s	0.54(5)	0.214	2.86(1)
		(O 1s)$_{\mathrm{anh}}$	0.79(8)	0.263(32)	2.98(8)
		(O 1s)$_{\mathrm{carb}}$	0.47(22)	0.128(12)	2.66(3)
		(O 1s)$_{\mathrm{av}}$	0.52(6)	0.212(10)	2.86(2)
	100 K [141]	C 1s	0.62	0.193(10)	2.81(2)
		(O 1s)$_{\mathrm{anh}}$	0.48(6)	0.204(18)	2.83(4)
		(O 1s)$_{\mathrm{carb}}$	0.40(5)	0.063(17)	2.50(4)
		(O 1s)$_{\mathrm{av}}$	0.47(5)	0.135(9)	2.67(3)
NTCDA	relaxed ML [142]	O 1s	0.59(11)		3.02(2)
		O KLL	0.56		3.03
	compressed ML [142]	O 1s	0.46(4)		3.12(3)
		O KLL	0.64		3.06
	[59]	C 1s	0.579(24)		2.997(16)
		(O 1s)$_{\mathrm{carb}}$	0.373(24)		2.747(25)
		(O 1s)$_{\mathrm{anh}}$	0.84(3)		3.004(15)
		(O 1s)$_{\mathrm{av}}$/O KLL	0.480(18)		2.872(14)
DIP [61]	0.5 ML	C 1s	0.55(8)	0.28(2)	3.01(4)
TBA [143]		N 1s			3.21(5)
Azobenzene [63]		C 1s	0.24(4)	0.28(3)	
		N 1s	0.53(9)	0.30(1)	3.07(2)

Table 5.17: XSW results of COMs on Ag(111) (continuation).

Molecule	Comment	Orbital	f_H	P_H	d_H (Å)
CuPc [19]	0.5 ML, 300 K	C 1s	0.631(13)	0.293(2)	3.049(5)
		N 1s	0.65(8)	0.269(9)	3.00(4)
		Cu 2$p_{3/2}$	0.95(8)	0.265(5)	2.98(4)
	0.85 ML, 300 K	C 1s	0.627(2)	0.269(2)	2.993(3)
		N 1s	0.69(8)	0.282(4)	3.03(4)
		Cu 2$p_{3/2}$	0.70(8)	0.233(4)	2.90(4)
	1.00 ML, 300 K	C 1s	0.475(5)	0.310(2)	3.089(3)
		N 1s	0.57(8)	0.297(3)	3.04(4)
		Cu 2$p_{3/2}$	0.53(8)	0.258(2)	2.97(4)
	0.5 ML, 153 K	C 1s	0.754(13)	0.272(2)	2.999(4)
		N 1s	0.94(8)	0.248(7)	2.94(4)
		Cu 2$p_{3/2}$	0.91(8)	0.224(5)	2.89(4)
	0.85 ML, 140 K	C 1s	0.647(5)	0.277(1)	3.010(2)
		N 1s	0.85(8)	0.278(3)	3.01(4)
		Cu 2$p_{3/2}$	0.81(8)	0.250(3)	2.94(4))
	1.00 ML, 140 K	C 1s	0.545(5)	0.305(1)	3.077(2)
		N 1s	0.64(8)	0.299(3)	3.07(4)
		Cu 2$p_{3/2}$	0.58(8)	0.280(3)	3.02(4)
F_{16}CuPc [11]		C 1s	0.30	0.380	3.25
		F 1s	0.46	0.463	3.45
SnPc [144]	1 ML, 300 K	C 1s	0.46(3)		3.16(3)
		N 1s	0.64(12)		3.24(6)
		Sn 3d	0.88(5)		2.46(3)
	0.87 ML, 150 K	C 1s	0.57(8)		2.93(6)
		N 1s	0.76(19)		3.12(7)
	Sn down/up	Sn 3d			2.59/4.01

Table 5.18: XSW results of COMs on Ag(111) (continuation).

Molecule	Comment	Orbital	f_H	P_H	d_H (Å)
H2Pc [117]	0.7 ML, 300 K	C 1s	0.51(9)	0.289	3.04(7)
		N 1s	0.47(9)	0.190	2.81(7)
	0.8 ML, 300 K	C 1s	0.57(9)	0.300	3.07(7)
		N 1s	0.58(9)	0.195	2.82(7)
	0.93 ML, 300 K	C 1s	0.49(9)	0.303	3.07(7)
		N 1s	0.50(9)	0.230	2.90(7)
	0.7 ML, 183 K	C 1s	0.70(9)	0.299	3.06(7)
		N 1s	0.61(9)	0.196	2.82(7)
	0.8 ML, 183 K	C 1s	0.74(9)	0.283	3.03(7)
		N 1s	0.75(9)	0.242	2.93(7)
	0.93 ML, 183 K	C 1s	0.63(9)	0.305	3.08(7)
		N 1s	0.95(9)	0.282	3.02(7)
EC4T [145]		S	0.70		3.15(5)
PEN [91]	0.50 ML, 295 K	C 1s	0.77(5)	0.267(5)	2.99(1)
	0.50 ML, 145 K	C 1s	0.94(5)	0.295(4)	3.04(1)
	0.75 ML, 295 K	C 1s	0.64(5)	0.326(4)	3.13(1)
	0.75 ML, 145 K	C 1s	0.73(5)	0.330(5)	3.13(1)
PFP [98]		C 1s	0.25(3)	0.34	3.16(6)
		F 1s	0.27(3)	0.34	3.16(6)
P2O [84]		C 1s	0.23	0.39	3.32
		O 1s	0.22	0.40	3.35
P4O [84]		C 1s	0.28	0.12	2.69
		O 1s	0.37	0.02	2.43
PYT	0.6 ML	C 1s	0.29(6)	0.05(1)	2.47(3)
		O 1s	0.47(5)	0.96(2)	2.25(4)
NO2PYT	0.6 ML	C 1s	0.59(11)	0.20(1)	2.82(2)
		O 1s (carbonyl)	0.55(10)	0.95(2)	2.23(3)
		O 1s (nitryl)	0.42(9)	0.11(3)	2.61(7)

5.11.3 The Au(111) surface

Table 5.19: XSW results of organic π-conjugated molecules on Au(111).

Molecule	**Comment**	**Orbital**	f_H	P_H	d_H (Å)
HBC	0.3 ML, 294 K	C 1s	0.56(5)	0.35(1)	3.10(2)
	0.3 ML, 117 K	C 1s	0.57(5)	0.35(1)	3.09(2)
CuPc [86]	0.7 ML, 300 K	C 1s	0.5(1)	0.434(4)	3.31(7)
		N 1s	0.6(1)	0.414(8)	3.26(7)
		Cu 2$p_{3/2}$	1.0(1)	0.388(10)	3.20(7)
	1.0 ML, 300 K	C 1s	0.5(1)	0.437(3)	3.31(7)
		N 1s	0.4(1)	0.413(6)	3.26(7)
		Cu 2$p_{3/2}$	0.8(1)	0.411(7)	3.25(7)
	0.7 ML, 133 K	C 1s	0.4(1)	0.462(5)	3.37(7)
		N 1s	0.5(1)	0.408(9)	3.25(7)
		Cu 2$p_{3/2}$	0.8(1)	0.408(14)	3.25(7)
	1.0 ML, 133 K	C 1s	0.4(1)	0.423(2)	3.28(7)
		N 1s	0.45(4)	0.5(1)	3.27(7)
		Cu 2$p_{3/2}$	0.8(1)	0.427(10)	3.29(7)
F_{16}CuPc [116]		C 1s	0.499	0.382	3.25
		F 1s	0.472	0.386	3.26
DIP [61]	0.8 ML	C 1s	0.62	0.35	3.11
PTCDA [74]		C 1s	0.62	0.42	3.27
P4O [84]	1.0 ML	C 1s	0.61	0.42	3.27

Chapter 6

Summary and Outlook

In this thesis, XSW measurements were performed for a variety of COM on Cu(111), Ag(111), and/or Au(111), yielding the corresponding bonding distance and molecular adsorption geometry with high precision. In addition to these findings, some trends of adsorption behaviors and dependencies have been observed, which lead to a better understanding of the interaction mechanism between COMs and metal surfaces. Here, an overview of the observed trends will be given with focus on the results obtained in this work. Overall, of course, the context of the literature is also to be kept in mind [11–15, 19, 59, 63, 74, 76, 79, 86, 98, 112, 115–117, 140–146].

6.1 Influences on the bonding distance

6.1.1 Influence of the substrate: DIP and PEN-derivatives on Cu(111), Ag(111), and Au(111)

In this work the bonding distance of DIP was analyzed in a comparative study on the three coinage metal surfaces. It was found out that the bonding distance of DIP increases in the order Cu(111), Ag(111) and Au(111) [61], similarly to PTCDA. Yet, differences of around 0.15 Å were found, which can most likely be related to the oxygen atoms of PTCDA.

PEN-derivatives with two and four carbonyl (C=O) groups (P2O and P4O, respectively) were studied with the XSW technique on the same metal surfaces, except P2O on Au(111). Measurements on Au(111) were presented in this work. All XSW results can be found in Ref. [84]. While on Cu(111) (Au(111)) both molecules adsorb at a small (large) distance, which can be related to chemisorption (mainly physisorption), the situation is different on Ag(111). On that substrate, P4O is chemisorbed, while P2O is physisorbed.

6.1.2 Influence of side groups

In the following, molecular modifications will be summarized, which influence the bonding distance:

Molecules with carbonyl groups: P4O on Au(111), PYT on Cu(111) and Ag(111), COHON on Cu(111)

In this work a couple of COMs with carbonyl groups were presented. The PEN-derivative P4O adsorbs on Au(111) at a distance, which indicates weak molecule-substrate interaction. We found indications that also other COMs with carbonyl groups are subject to the mechanism of surface induced aromatic stabilization [84]: PYT, a disk-like COM with four carbonyl groups, adsorbs on Cu(111) and Ag(111) at a similar distance compared to P2O and P4O, both the carbon and the oxygen atoms. COHON (disk-like with six carbonyl groups) displays on Cu(111) similar bonding distance as PYT [147]. In all cases, the oxygen atoms bend toward the crystal and the molecules adsorb at distances that are typical for chemisorption. Hence, the shape of the organic compound has no significant influence on the bonding distance in this context.

Molecules with other side groups: PYT and NO2PYT on Ag(111)

PYT was investigated on Ag(111) with and without nitryl (NO_2) side groups, which is a significantly different group compared to the carbonyl group regarding size and chemical structure. The oxygen atoms of the carbonyl side groups adsorb at the same distance to the surface. The small distance is a clear indication for a covalent bond. In contrast, the carbon atoms of the two molecules adsorb at different distances, for NO2PYT ~ 0.35 Å higher than for PYT. The nitryl side groups adsorb at a bonding distance similar to the carbon backbone. The influence of the side groups on the carbon bonding distance in this case is the following: While the carbonyl groups lower the bonding distance of the carbon skeleton, the nitro groups lead to an upwards-lifted carbon skeleton, without affecting the carbonyl groups.

6.1.3 Influence of central metal ion: H2Pc, 2HTPP and CuTPP on Cu(111)

The influence of the central metal atom of Pcs was investigated by measuring the metal-free Pc (H2Pc) and comparing it to metalized Pcs. H2Pc on Cu(111) adsorbs at similar bonding distances than ZnPc, but lower than CuPc. Hence, the metal-free Pc has the smallest bonding distance.

For TPP on Cu(111), the carbon atoms exhibit on average only minor changes of the bonding distance after self-metalation. Yet, the porphyrin macrocycle changes from the saddle-shape to a flat geometry with phenyl groups, that are slightly bent upwards.

6.1.4 Influence of the coverage: PEN on Ag(111)

A rather strong influence of the coverage on the bonding distance was found for PEN on Ag(111) [91]. An increase of 0.1 Å was measured when increasing the coverage from 0.5 ML to 0.75 ML. The reason for a coverage-dependent bonding distance lies in the interaction

between neighbouring molecules that simultaneously competes with the molecule-substrate interaction. In general, this dependence can be especially important for the interpretation and comparison of XSW results.

6.1.5 Influence of the temperature: HBC on Au(111), PEN on Ag(111), 2HTPP and CuTPP on Cu(111)

Besides the XSW measurements at RT, some samples were also studied at temperatures in the range of 100–200 K in order to investigate the influence of temperature on the bonding distance. For HBC on Au(111), no temperature dependence is observed. The bonding distance of PEN on Ag(111) depends on the temperature for a lower coverage (0.5 ML) only mildly [91]. In this case the difference of the bonding distance between RT and 145 K is 0.05 Å. In contrast, a more denser molecular coverage (0.75 ML), no effect of the temperature is observed. For higher coverages the temperature effect can be neglected compared to intermolecular interactions.

2HTPP and CuTPP also displayed a weak temperature dependence. Mainly the carbon atoms show a difference beyond the error bars, namely $\Delta d = 0.05$ Å.

Overall we can conclude that the effect on the temperature on the bonding distance seems to be small, at least for the temperature range and for the compounds investigated here.

6.1.6 Organic-organic interface

XSW results of the organic-organic interface were presented in this work for a bilayer consisting of one ML PEN on Cu(111), where a submonolayer of PFP was deposited on the top. The influence of the PFP molecules is reflected, on one hand, in a slightly (by 0.08 Å) smaller bonding distance of PEN, compared to the bare monolayer, and, on the other hand, in a distortion of PFP. The carbon atoms adsorb 3.37 Å above the PEN molecule, which shows that the PFP molecule is rather physisorbed. The fluorine atoms of PFP are bent towards the PEN molecules, probably due to quadrupole interaction between PEN and PFP molecules.

In the literature exist two other organic-organic heterostructures that have been studied with the XSW technique, CuPc on PTCDA/Ag(111) and F_{16}CuPc on CuPc/Ag(111). In the first bilayer, the CuPc molecules that adsorbed on PTCDA/Ag(111) lead to a reduction of the carbon bonding distance of PTCDA from 2.86 Å to 2.81 Å, while the CuPc molecules remain almost flat at a distance of 3.22 Å above the PTCDA molecules [112]. For the latter bilayer, the distance between F_{16}CuPc and CuPc is 3.06 Å. There, no distortion of the perfluorinated molecule is observed.

6.2 Outlook

At the end of this work it becomes clear that during the last years many geometric properties of COM on metal surfaces have been analyzed using the XSW technique. One may ask, therefore, whether this technique can be used in future to obtain further insights in the adsorption behavior of COMs. This outlook can be used to present possible fields of interest, which are worth studying with the XSW technique:

- The obvious way to take is to analyze more and more COMs and to learn about interface properties by comparison between them. This can be achieved by systematically modifying molecules and comparing the XSW results with other structural or electronic properties, as was done so far in many cases. For instance, after PTCDA and DIP more perylene-derivatives and perylene itself on noble metal surfaces can be analyzed.

- At this point so far, the XSW technique was applied to COMs, which are adsorbed on noble metal surfaces Cu(111), Ag(111), Au(111), a few studies also involved other surfaces like Ag(110) and Ag(100) [148]. A new route to go would be to extend the substrates to other single crystals. The combination of COMs and ZnO as substrate depicts the interface between an organic and inorganic semiconductor, offering new possibilities for electronic devices [149].

- As part of fundamental research, the XSW technique was used to experimentally determine one non-dipole parameter, S_R, as described in Section 4.1.3. In addition, that section contains a description of how to experimentally determine the second independent non-dipole parameter Ψ, which was not done so far.

- As shown in this work, the XSW technique can be used to study organic-organic interfaces. For devices based on more than one organic compound it is pivotal to understand this interfaces in more detail, especially with regard to a possible charge transfer.

As shown in the past, especially the combination of the XSW technique with other experimental techniques or DFT calculations yields precious information about interface phenomena.

Appendix A

Appendix

A.1 In-house surface science UHV chamber

During this work, an in-house UHV chamber was set up for the following surface science experiments:

- XPS
- LEED
- TDS.

In the following, a description of the setup is given, a simplified illustration thereof can be found in Figure A.1. The whole UHV chamber contains three sections:

- The **load lock** is used to insert or exchange samples without breaking the vacuum in the preparation and analysis chamber, if the valve next to the preparation chamber is closed. The load lock is pumped with a turbo pump. To the left side of the load lock a Omicron transfer rod is installed, which is used to transfer the samples between the load lock and the preparation chamber, and between the preparation chamber and analysis chamber.
- The **preparation** chamber has an ion getter pump (Leybold IZ 80) to maintain a base pressure of 2×10^{-9} mbar. A home-built manipulator (see Figure A.2) is installed in the preparation chamber with integrated resistive heating. At its front side a mask for selective deposition of thin films is attached, and at its backside a QCM to monitor the growth rate. On a free flange with a plate valve attached a Knudsen cell can be swapped without breaking the vacuum. Additionally, a LEED (OCI Vacuum Microengineering) is installed on a CF-150 flange. A valve is placed between preparation chamber and analysis chamber for protection of the respective chambers.
- The **analysis chamber** is pumped by a turbo pump (Oerlikon TURBOVAC 361) and a titanium sublimation pump (TSP), enabling a base pressure of 2×10^{-10}

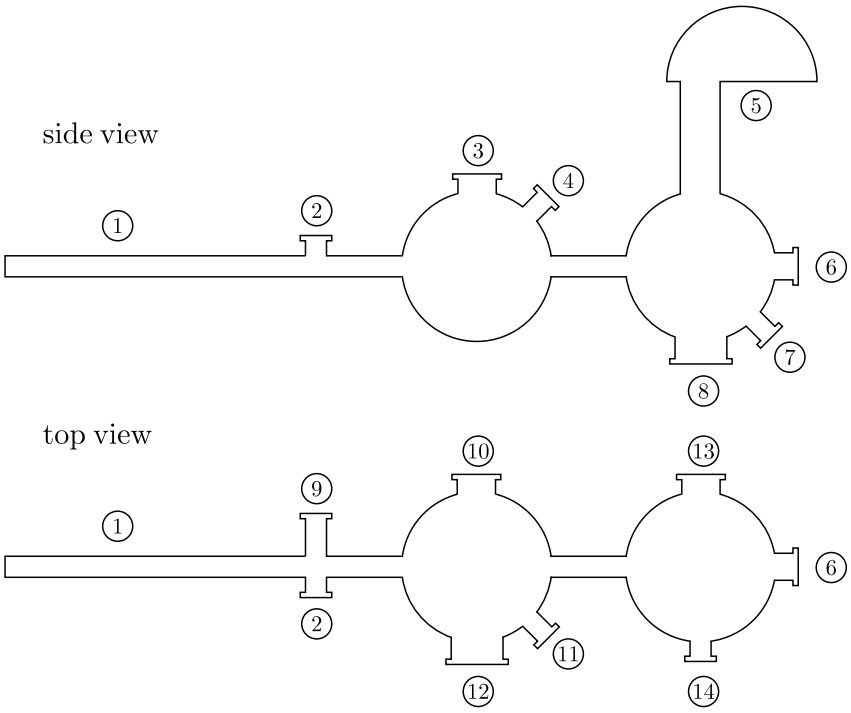

①	Transfer rod (load lock ↔ preparation chamber preparation chamber ↔ analysis chamber)	⑧	Pumping units (titanium sublimation pump, turbo pump 1) and pressure gauge 1
②	Load lock	⑨	Turbo pump 2, pressure gauge 2
③	Manipulator with electric feed through for sample heating and thermocouple	⑩	Ion getter pump
④	Electric connection for QCM	⑪	Knudsen cell
⑤	Hemispherical electron analyzer	⑫	LEED
⑥	Quadrupole mass spectrometer	⑬	Manipulator
⑦	Installation for Ar^+ sputtering	⑭	X-ray tube

Figure A.1: Schematic picture of the in-house surface science vacuum chamber in top view and side view. A detailed description of the individual components is given in the main text. Not shown are the valves between the load lock, preparation chamber, and analysis chamber.

mbar. The analysis chamber is equipped with installation for Ar^+ sputtering and a quadrupole mass spectrometer (QMS, Extrel MAX1000-LT). The QMS can detect masses in the range from 2 amu to 1000 amu. Thus, typical COMs can be analyzed. For XPS studies an OMICRON X-ray tube (DAR400 with Al/Mg dual anode) and electron analyzer (SPHERA U7) is available. The manipulator (see Figure A.3) can be heated resistively up to 1100 K. The temperature is monitored using a K-type thermocouple, which is in direct contact to the sample.

In the following, a description of the manipulators of the preparation and analysis chamber is given, which are especially important for TDS experiments.

A.1.1 Manipulator of the preparation chamber

A picture of the manipulator of the preparation chamber is shown in Figure A.2. The growth rate can be determined using the QCM at its backside. At the front side a mask is placed in front of the single crystal containing a hole with a diameter of 5 mm. The aim of

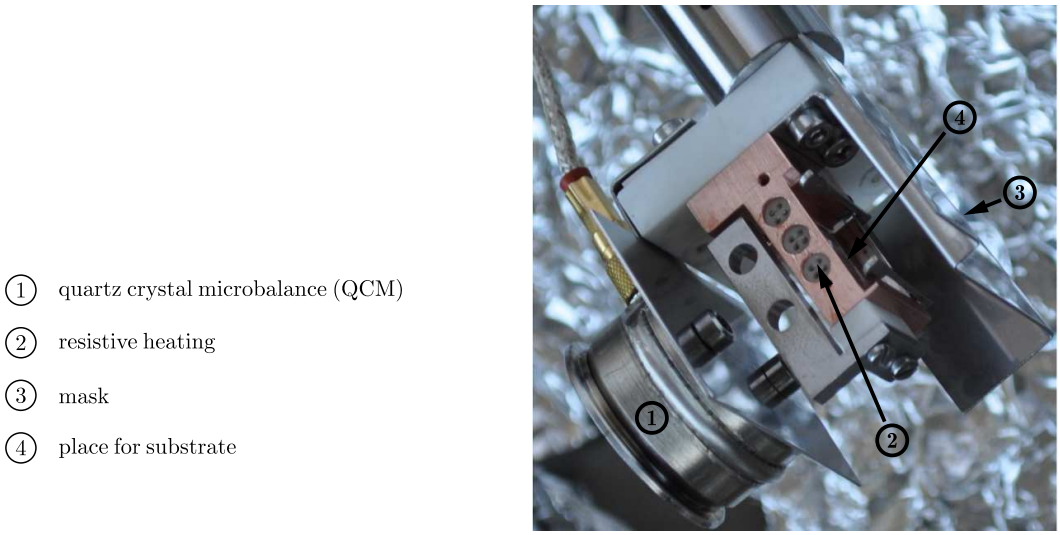

Figure A.2: Photograph of the manipulator of the preparation chamber, without sample. The mask consists of a metal shielding with a hole (diameter 5 mm) above the single crystal. The mask prevents evaporation onto parts beside the single crystal, which can later influence the TDS measurements.

the hole is to obtain a well-defined area on the single crystal that is covered with molecules. This is important since the angle of the molecular beam coming from the Knudsen cell (for detailed description of the Knudsen cell see Section 4.3) is large enough to deposit molecules on the whole manipulator. Therefore, by using the mask, contamination of the sample plate is avoided, which could later disturb the QMS signal, because molecules are desorbing from other parts than the substrate. At the other hand, this method requires later precise alignment of the QMS with respect to the covered spot on the sample in order to maximize the molecular flux into the QMS during TDS experiments.

The manipulator of the preparation chamber can be heated up to $\sim$ 600 K. The temperature of the manipulator can be measured via a K-type thermocouple, with is placed in vicinity to the sample.

A.1.2 Manipulator of the analysis chamber

Figure A.3 provides a picture of the manipulator of the analysis chamber. This manipulator is designed to enable XPS and TDS measurements. If a sample is transferred onto the manipulator, a thermocouple touches the flank of the single crystal. Thus, the temperature of the sample is measured. A Boralectric heating element is installed below

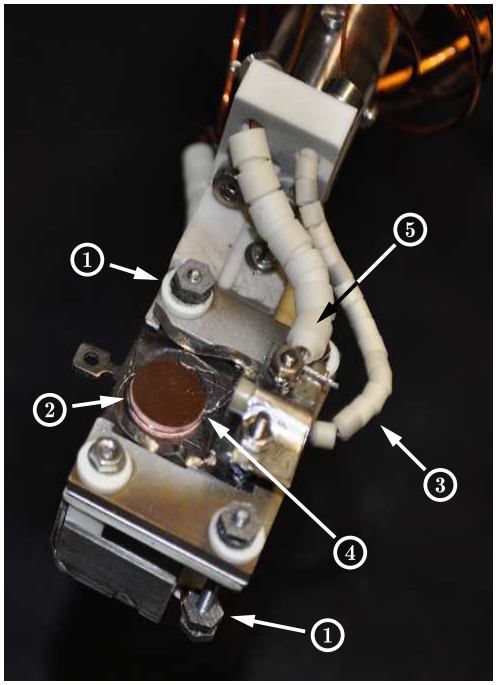

1. electric feed line for resistive heating
2. Cu(111) single crystal
3. thermocouple
4. tip of thermocouple (touching the side of the substrate)
5. electric feed line for drain current

Figure A.3: Picture of the manipulator of the preparation chamber, with a Cu(111) single crystal. The temperature is measured by a K-type thermocouple, which is guided via ceramics to touch the single crystals at the side.

the sample plate. With this setup is it possible to achieve $\sim$ 1100 K at the sample surface.

A.2 Thermal desorption spectroscopy

Thermal desorption spectroscopy (TDS, which is also called temperature-programmed desorption, TPD) experiments are performed by increasing in a controlled way, usually linearly, the temperature of a sample that is covered with an adsorbate (mostly: molecules). The desorbing molecules are detected using a QMS. The QMS signal related to the molecule

is plotted as a function of the temperature to compose a TD spectrum, see Figure A.6. This technique can be used to determine the desorption energy of molecules interacting with substrate surfaces (molecules in the first monolayer), and to measure the desorption energy of molecule from higher layers (second, third, etc.). One has to bear in mind that only for desorption without activation barrier the desorption energy is equal to the adsorption energy. Figure A.4 depicts the scenario, in which during the adsorption process an activation barrier has to be overcome.

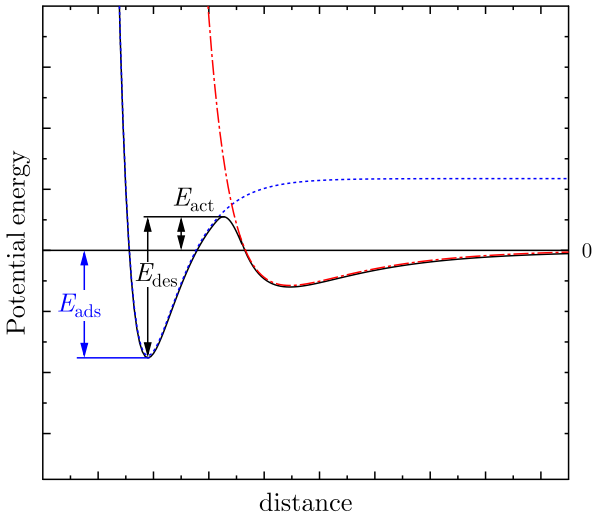

Figure A.4: Schematic slope of the potential energy as a function of distance between molecule and surface, for the case of a precursor-mediated activated chemisorption. The local minimum represents a loosely bound molecule, which can migrate around the surface (physisorption) until it becomes trapped by the formation of a strong bond to the surface (chemisorption). In the depicted case, $E_{act} > 0$, and the desorption energy is *larger* than the adsorption energy. Graph adapted from Ref. [150].

Molecules from the monolayer desorb from metal surfaces typically at higher temperatures than the multilayer (second layer and higher). This difference can be used to prepare well-defined monolayer films by annealing a multilayer film to a temperature above the desorption temperature of the multilayer but below the desorption temperature of the monolayer.

At the same time, experimentally determined adsorption energies are an important information of the particular interface. They can be used to cross-check theoretical models that are describing the interaction between COMs and metal single crystals. As presented earlier in this work, the experimentally determined bonding distance is available for some molecules on metal surfaces 5.11 and, therefore, are used to benchmark DFT calculations. Adsorption energies are an additional source to validate DFT calculations.

In the following a short overview on the theory is given and preliminary results are presented, which were obtained using the setup described above (Section A.1).

A.2.1 Theoretical overview

The description in this section is based on Ref. [150]. The starting point for TDS analysis is the Polanyi-Wigner equation that can be written in the form

$$r_{\mathrm{des}} = -\frac{\mathrm{d}\Theta}{\mathrm{d}T} = \frac{\nu_n(\Theta)\Theta^n}{\beta} \cdot \mathrm{e}^{-\frac{E_{\mathrm{des}}(\Theta)}{k_{\mathrm{B}}T}} \tag{A.1}$$

The desorption rate r_{des}, which can be considered as the signal of the QMS during the TDS experiment, depends in this equation on the coverage Θ, on the preexponential factor ν_n, on the desorption energy E_{des}, on the heating rate β, and on the temperature T. n is the order of desorption and commonly found values are $n = 0, 1, 2$. Note that the shape of the desorption rate is a peak, although the Polanyi-Wigner equation is proportional to the exponential function that increases steadily. However, with proceeding desorption of molecules, the coverage Θ becomes smaller an finally goes to zero.

To determine the peak position T_{peak} one can use for $n = 1$ the Redhead approximation, in which ν_1 and E_{des} does not depend on the coverage. Then, the desorption energy can be calculated via

$$E_{\mathrm{des}} = k_{\mathrm{B}}T_{\mathrm{peak}} \left(\ln \frac{\nu_1 T_{\mathrm{peak}}}{\beta} - 3.64 \right), \tag{A.2}$$

assuming the correct value for ν_1. For small molecules such as CO, the preexponential factor is chosen to be $\nu_1 = 10^{13}$ s^{-1}. For larger molecules as typical COMs, this value has to be larger, in the range from 10^{16} s^{-1} to 10^{21} s^{-1} [151, 152].

Figure A.5 visualizes the influence of the desorption order n on the shape of the desorption rate $r_{\mathrm{des}}(T)$. For $n = 0$, the desorption rate is proportional to the exponential

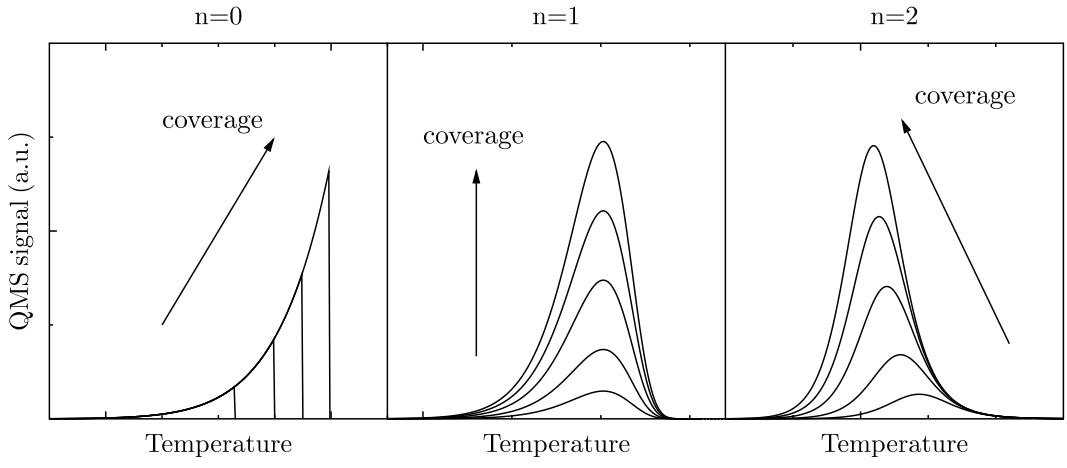

Figure A.5: Simulated TD spectra for desorption order $n = 0, 1, 2$ (left to right). For each desorption order spectra were calculated for different coverages. The following trends of the peak temperature can be observed, as indicated by the arrows: For $n = 0$ the peak temperature shifts with increasing coverage toward higher values. For $n = 1$, the peak temperature stays constant for varying coverages, and for $n = 2$ the peak temperature shifts with increasing coverage toward lower temperatures.

function, until no adsorbed molecules are left. Therefore, T_{peak} will shift for thicker films toward higher temperatures. For $n = 1$ the peak position does not depend on the coverage, while for $n = 2$ the peak shifts toward lower temperatures with increasing film thickness.

A.2.2 Results

In the following preliminary TDS results are presented of DIP on Au(111) and 2HTPP on Cu(111). For the data analysis a Gaussian smoothing routine was applied to the raw data. The result of the smoothing is displayed in Figure A.6. The solid line shows the raw data, the dashed line the smoothed data.

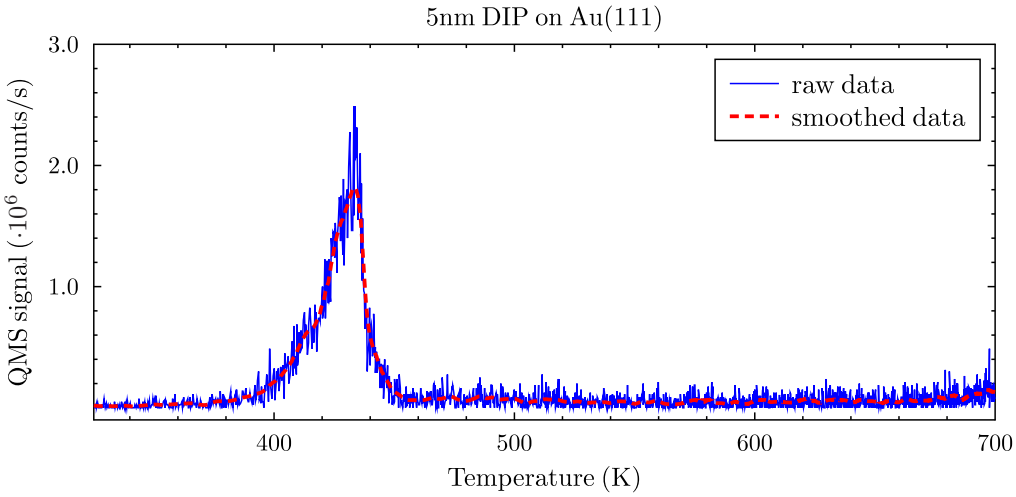

Figure A.6: TD spectrum without (solid line) and with smoothing (dashed line) due to a Gaussian smoothing routine.

DIP on Au(111)

The coverages displayed in the following were determined with the QCM. In the preparation chamber, there is a large difference of the distance between the Knudsen cell and the QCM on the one hand and between the Knudsen cell and the single crystal on the other hand. Assuming the validity of the inverse-square law for the molecular beam, the coverage on the crystals are significantly smaller than the values determined with the QCM, at least by a factor of 2. The numbers given here relate to the QCM values. In addition, the single crystals and the QCM have different sticking coefficients, giving rise to further deviations of the thickness on the substrate. Besides these uncertainties of the absolute thickness, we can trust the relative values of the coverages on a substrate. TD spectra of DIP on Au(111) are displayed in Figure A.7, both for multilayer and monolayer coverages. The shape of the curves for the 5 nm and 10 nm films indicates a desorption order $n = 0$ due to the abrupt decline of the QMS signal. This is a typical behavior for multilayer-coverage of COMs on various surfaces. It was shown that PEN on Au(111) [90] and PTCDA on Cu(111) [153] exhibit zeroth desorption order. As expected for $n = 0$, the peak temperature increases

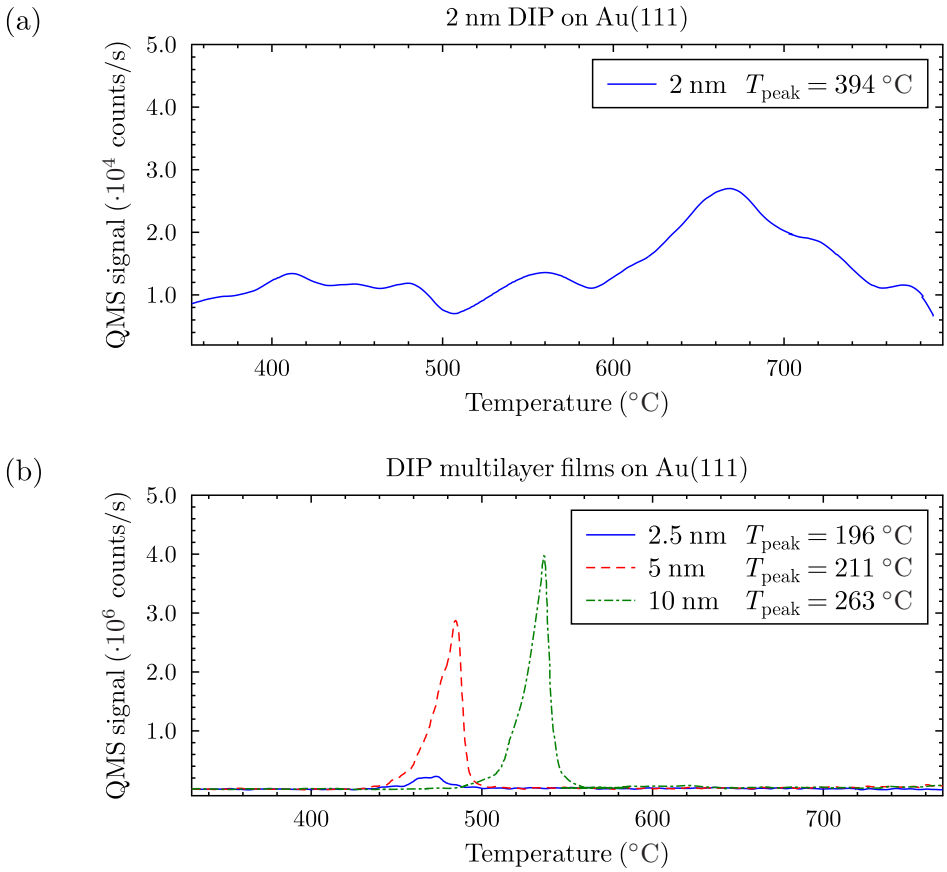

Figure A.7: TD spectra of DIP on Au(111) for different (a) monolayer films and (b) multilayer films. The heating ramp was 0.5 K/s for all spectra. Note that the nominal coverages, determined with the QCM, vary strongly compared to the real coverage due to different distances from sample and QCM to the Knudsen cell.

with thicker films. Yet, in contrast to the expected slope of the desorption order $n = 0$, the onset at the left side of the peak is not at a constant position but is shifted rather strongly toward higher temperatures for the sample with thickness 10 nm. A likely reason for a variation can be the temperature as the slope of the heating rate differed slightly for the three samples. Although the gradient was the same in average for all samples, the slope was fluctuating while desorbing the thickest film. A second uncertainty arises from the temperature measurement. When inserting the sample onto the manipulator of the analysis chamber, the side of the crystal touched the thermocouple. The precise position might vary after each transfer. A difference of ~ 30 K is, however, unlikely. Here, more experiments of this type have to be performed before one can decide, whether the observed variation of the onset temperature occurs due to missing reproducibility or due to effects at the interface.

Let us now turn to the monolayer spectrum, which was observed for a nominal thickness of 2 nm. The peak temperature is 667 K. Applying the Redhead equation (Equation A.2) and assuming a preexponential factor of 1.6×10^{19} s^{-1}, which was determined for PEN on Au(111) [90], we obtain a desorption energy of $E_{\mathrm{des}} = 263$ kJ/mol, or 2.73 eV. This value is significantly higher than PEN on Au(111), for which $E_{\mathrm{des}} = 2.10$ eV was determined [90]. DFT calculations of DIP on Au(111) yielded the adsorption energy 2.53 eV (see Table 5.2). Note that the desorption and adsorption energy equal only in case the adsorption occurs without crossing an activation barrier.

2HTPP on Cu(111)

First TDS measurements of 2HTPP on Cu(111) were performed. This molecule undergoes a thermally activated self-metalation when adsorbed on Cu(111). This transformation was analyzed with the XSW technique in great detail in Section 5.9. Here, the aim was to study the range of influence of the metalation process, whether this process occurs only in the first layer or also extends to higher layers. The molecule starts to metalate at ~ 420 K. As it was observed for DIP on Au(111) in the previous section, the multilayer of COMs can start to desorb at similar temperatures. If the metalation occurs up to higher layers, the metalation and desorption of molecules are two competing effects.

Figure A.8 displays TD spectra for two different coverages. In both spectra, a peak related to the metal-free (solid line) and one related to the metalated CuTPP (dashed line) is visible. In all four spectra, the onset of the peak is located at ~ 430 K. The peak maxima shift toward higher temperature. This finding in addition to the steep decline, being more pronounced for the 13 nm film, indicate a desorption order of $n = 0$. Within one sample, the peak temperatures related to 2HTPP and CuTPP are very similar, being 453 K for the 4 nm film and 475 K for the 13 nm film. The desorption characteristics, i.e. the peak temperature and desorption order, can be related to multilayer desorption. This means that the metalation process extends the monolayer up to higher layers. If we look closer we see that for the 4 nm film the intensity of the CuTPP peak is higher than the 2HTPP peak. In contrast, for the 13 nm film the situation is reversed. The higher intensity of the 2HTPP peak is a clear sign that the metalation does not happen to molecules in

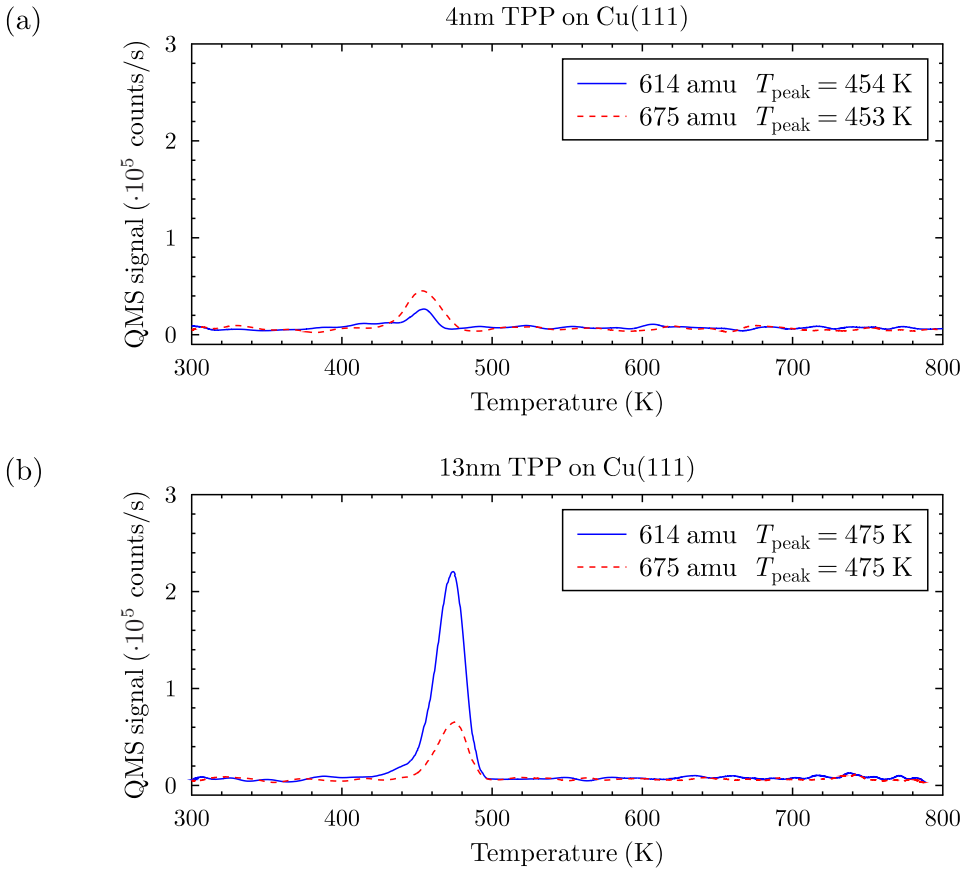

Figure A.8: TD spectra of TPP on Cu(111) for different multilayer films. Each figure contains a graph of the 2HTPP (614 amu) and the thermally induced self-metalated CuTPP (675 amu). The temperature ramp β was 0.44 K/s (0.51 K/s) for the 4 nm (13 nm) sample.

the upper layers before they desorb. Future work can investigate the desorption of TPP at various heating rates.

A.3 Molecular coverage of the samples

Table A.1 provides an overview of the coverages, which were prepared for the XSW analysis. The deposited molecular coverage was calculated using the method described in Section 2.3. If no data of the unit cell was available, the molecular size was estimated based on its dimension.

Table A.1: Parameters which were used to determine the molecular coverage. Intensity of a peak was measured after background subtraction. The size of the molecule refers either to the unit cell, if this information is available, or by estimations based on the molecular dimensions. Exemplary films are chosen in case that more than one film was prepared.

System	Orbitals	Intensity ratio	molecular size ($Å^2$)	Coverage (ML)
P4O/Au(111)	C $1s$/Au $4d_{5/2}$	0.011	144 [84]	1.0
HBC/Au(111)	C $1s$/Au $4d_{5/2}$	0.0049	185 [87]	0.3
PEN/Ag(111)	C $1s$/Ag $3d_{5/2}$	0.011	138 [154]	0.5
PEN/Cu(111)	C $1s$/Cu $3p_{3/2}$	0.047	140 [14]	1.0
DIP/Cu(111)	C $1s$/Cu $3p_{3/2}$	0.035	152 [71]	0.6
DIP/Ag(111)	C $1s$/Ag $3d_{5/2}$	0.013	173 [72]	0.5
DIP/Au(111)	C $1s$/Au $4d_{5/2}$	0.0082	197 [73]	0.8
H2Pc/Cu(111)	C $1s$/Cu $3p_{3/2}$	0.026	240	0.7
VOPc/Cu(111)	C $1s$/Cu $3p_{3/2}$	0.023	240	0.6
PYT/Cu(111)	C $1s$/Cu $3p_{3/2}$	0.052	80	0.9
PYT/Ag(111)	C $1s$/Ag $4d_{5/2}$	0.016	80	0.6
NO2PYT/Ag(111)	C $1s$/Ag $4d_{5/2}$	0.011	96	0.6
COHON/Cu(111)	C $1s$/Cu $3p_{3/2}$	0.027	100	0.4
TPP/Cu(111)	C $1s$/Cu $3p_{3/2}$	0.042	240	0.8

Acronyms

Molecules

2HTTP	Tetraphenylporphyrin	$C_{44}H_{30}N_4$
AB	Trans-Azobenzene	$C_{12}H_{10}N_2$
COHON	Coronene-hexaone	$C_{24}H_6O_6$
CuPc	Copper(II)-phthalocyanine	$CuC_{32}H_{16}N_8$
CuTPP	Copper(II)-tetraphenylporphyrin	$CuC_{44}H_{28}N_4$
DIP	Diindenoperylene	$C_{32}H_{16}$
EC4T	End-capped quaterthiophene	$C_{24}H_{22}S_4$
F4-TCNQ	2,3,5,6-Tetrafluoro-7,7,8,8-tetracyanoquinodimethane	$C_{12}F_4N_4$
F_{16}CuPc	Copper(II)-phthalocyanine	$CuC_{32}F_{16}N_8$
F_{16}ZnPc	Copper(II)-phthalocyanine	$ZnC_{32}F_{16}N_8$
GaClPc	Chlorogallium-phthalocyanine	$GaClC_{32}H_{16}N_8$
HBC	Hexa-*peri*-hexabenzocoronene	$C_{42}H_{18}$
H2Pc	29H,31H-Phthalocyanine	$C_{32}H_{18}N_8$
NO2PYT	2,7-Dinitropyrene-4,5,9,10-tetraone	$C_{16}H_4N_2O_8$
NTCDA	1,4,5,8-Naphthalene-tetracarboxylicacid-dianhydride	$C_{14}H_4O_6$
P2O	6,13-Pentacenedione	$C_{22}H_{12}O_2$
P4O	Pentacene-5,7,12,14-tetraone	$C_{22}H_{10}O_4$
PEN	Pentacene	$C_{22}H_{14}$
PFP	Perfluoropentacene	$C_{22}F_{14}$
PTCDA	3,4,9,10-Perylene-tetracarboxylic-dianhydride	$C_{32}H_8O_6$
PYT	Pyrene-4,5,9,10-tetraone	$C_{16}H_8O_4$
SnPc	Tin-phthalocyanine	$SnC_{32}H_{16}N_8$
TBA	3,3',5,5'-Tetra-tert-butyl-azobenzene	$C_{28}H_{42}N_2$
VOPc	Vanadium(IV) oxide phthalocyanine	$C_{32}H_{16}N_8VO$
ZnPc	Copper(II)-phthalocyanine	$ZnC_{32}H_{16}N_8$

Analysis techniques

AFM	atomic force microscopy
LEED	low-energy electron diffraction
NEXAFS	near edge X-ray absorption fine structure
PES	photoelectron spectroscopy
STM	scanning tunneling microscopy
TDS	thermal desorption spectroscopy
TPD	temperature programmed desorption
UPS	UV photoelectron spectroscopy
XPS	X-ray photoelectron spectroscopy
XSW	X-ray standing wave

Miscellaneous

COM	conjugated organic molecule
CTC	charge transfer complex
DFT	density functional theory
EA	electron affinity
EDC	energy distribution curve
ELA	energy level alignment
E_{B}	binding energy
E_{Bragg}	Bragg energy
E_{F}	Fermi energy, Fermi level, Fermi edge
E_{kin}	kinetic energy
E_{Vac}	vacuum energy
f_H	coherent fraction
HIB	hole injection barrier
HOMO	highest occupied molecular orbital
IE	ionization energy
ID	interface dipole
LUMO	lowest unoccupied molecular orbital
ML	monolayer
ϕ	work function
P_H	coherent position
QMS	quadrupole mass spectrometer
QCM	quartz crystal microbalance
SECO	Secondary electron cut-off
TDD	Theory of dynamical diffraction
vdW	van der Waals

Bibliography

[1] J. H. Burroughes, D. D. C. Bradley, A. R. Brown, R. N. Marks, K. Mackay, R. H. Friend, P. L. Burns, and A. B. Holmes, Light-emitting diodes based on conjugated polymers, *Nature* **347**, 539, doi:10.1038/347539a0 (1990). 1

[2] M. A. Baldo, D. F. O'Brien, Y. You, A. Shoustikov, S. Sibley, M. E. Thompson, and S. R. Forrest, Highly efficient phosphorescent emission from organic electroluminescent devices, *Nature* **395**, 151, doi:10.1038/25954 (1998).

[3] T. W. Kelley, P. F. Baude, C. Gerlach, D. E. Ender, D. Muyres, M. A. Haase, D. E. Vogel, and S. D. Theiss, Recent progress in organic electronics: Materials, devices, and processes, *Chem. Mater.* **16**, 4413, doi:10.1021/cm049614j (2004). 1

[4] C. D. Dimitrakopoulos and P. R. L. Malenfant, Organic Thin Film Transistors for Large Area Electronics, *Adv. Mater.* **14**, 99, doi:10.1002/1521-4095(20020116)14:2<99::AID-ADMA99>3.0.CO;2-9 (2002). 1

[5] M. Granström, K. Petritsch, A. C. Arias, A. Lux, M. R. Andersson, and R. H. Friend, Laminated fabrication of polymeric photovoltaic diodes, *Nature* **395**, 257, doi:10.1038/26183 (1998). 1

[6] P. Peumans, S. Uchida, and S. R. Forrest, Efficient bulk heterojunction photovoltaic cells using small-molecular-weight organic thin films, *Nature* **425**(6954), 158, doi:10.1038/nature01949 (2003). 1

[7] L. P. Ma, J. Liu, and Y. Yang, Organic electrical bistable devices and rewritable memory cells, *Appl. Phys. Lett.* **80**(16), 2997, doi:10.1063/1.1473234 (2002). 1

[8] M. J. Kang, I. Doi, H. Mori, E. Miyazaki, K. Takimiya, M. Ikeda, and H. Kuwabara, Alkylated Dinaphtho[2,3-*b*:2',3'-*f*]Thieno[3,2-b]Thiophenes (C_n-DNTTs): Organic Semiconductors for High-Performance Thin-Film Transistors, *Adv. Mater.* **23**(10), 1222, doi:10.1002/adma.201001283 (2011). 1

[9] D. Feili, M. Schuettler, T. Doerge, S. Kammer, and T. Stieglitz, Encapsulation of organic field effect transistors for flexible biomedical microimplants, *Sensors Actuators A: Physical* **120**(1), 101, doi:10.1016/j.sna.2004.11.021 (2005). 1

[10] K. Siegbahn, Electron spectroscopy for atoms, molecules, and condensed matter, *Rev. Mod. Phys.* **54**(3), 709, doi:10.1103/RevModPhys.54.709 (1982). 2, 9, 14

[11] A. Gerlach, F. Schreiber, S. Sellner, H. Dosch, I. A. Vartanyants, B. C. C. Cowie, T.-L. Lee, and J. Zegenhagen, Adsorption-Induced Distortion of F_{16}CuPc on Cu(111) and Ag(111): An X-ray Standing Wave Study, *Phys. Rev. B* **71**(20), 205425, doi:10.1103/PhysRevB.71.205425 (2005). 2, 78, 99, 102, 105

[12] A. Hauschild, K. Karki, B. C. C. Cowie, M. Rohlfing, F. S. Tautz, and M. Sokolowski, Molecular Distortions and Chemical Bonding of a Large π-Conjugated Molecule on a Metal Surface, *Phys. Rev. Lett.* **94**(3), 036106, doi:10.1103/PhysRevLett.94.036106 (2005). 46, 82, 101

[13] A. Gerlach, S. Sellner, F. Schreiber, N. Koch, and J. Zegenhagen, Substrate dependent bonding distances of PTCDA - A comparative X-ray standing wave study on Cu(111) and Ag(111), *Phys. Rev. B* **75**(4), 045401, doi:10.1103/PhysRevB.75.045401 (2007). 2, 36, 37, 46, 98, 101

[14] N. Koch, A. Gerlach, S. Duhm, H. Glowatzki, G. Heimel, A. Vollmer, Y. Sakamoto, T. Suzuki, J. Zegenhagen, J. P. Rabe, and F. Schreiber., Adsorption induced intramolecular dipole: Correlating molecular conformation and interface electronic structure, *J. Am. Chem. Soc.* **130**(23), 7300, doi:10.1021/ja800286k (2008). 2, 4, 5, 61, 62, 65, 66, 68, 99, 119

[15] S. Duhm, A. Gerlach, I. Salzmann, B. Bröcker, R. Johnson, F. Schreiber, and N. Koch, PTCDA on Au(111), Ag(111) and Cu(111): Correlating bonding distance and interfacial charge transfer, *Org. Electron.* **9**(1), 111, doi:10.1016/j.orgel.2007.10.004 (2008). 2, 3, 5, 46, 57, 82, 105

[16] J. E. Lennard-Jones, Processes of adsorption and diffusion on solid surfaces, *Trans. Faraday Soc.* **28**, 333, doi:10.1039/TF9322800333 (1932). 2

[17] I. Markov and A. Milchev, Theory of epitaxy in a Frank-van der Merwe model with anharmonic interactions, *Thin Solid Films* **126**(1–2), 83, doi:http://dx.doi.org/10.1016/0040-6090(85)90179-8 (1985). 2

[18] A. Bondi, van der Waals Volumes and Radii, *J. Phys. Chem. C* **68**(3), 441, doi:10.1021/j100785a001 (1964). 3, 80

[19] I. Kröger, B. Stadtmüller, C. Stadler, J. Ziroff, M. Kochler, A. Stahl, F. Pollinger, T.-L. Lee, J. Zegenhagen, F. Reinert, and C. Kumpf, Submonolayer growth of copper-phthalocyanine on Ag(111), *New J. Phys.* **12**, 083038, doi:10.1088/1367-2630/12/8/083038 (2010). 3, 64, 80, 102, 105

[20] N. Koch, A. Kahn, J. Ghijsen, J.-J. Pireaux, J. Schwartz, R. L. Johnson, and A. Elschner, Conjugated organic molecules on metal versus polymer electrodes: Demonstration of a key energy level alignment mechanism, *Appl. Phys. Lett.* **82**(1), 70, doi:10.1063/1.1532102 (2003). 3

[21] W. Kohn and L. J. Sham, Self-Consistent Equations Including Exchange and Correlation Effects, *Phys. Rev.* **140**, A1133, doi:10.1103/PhysRev.140.A1133 (1965). 6

[22] P. Hohenberg and W. Kohn, Inhomogeneous Electron Gas, *Phys. Rev.* **136**(3B), B864, doi:10.1103/PhysRev.136.B864 (1964). 6

[23] A. Tkatchenko, L. Romaner, O. T. Hofmann, E. Zojer, C. Ambrosch-Draxl, and M. Scheffler, Van der Waals Interactions Between Organic Adsorbates and at Organic/Inorganic Interfaces, *MRS Bulletin* **35**(06), 435, doi:10.1557/mrs2010.581 (2010). 6, 46

[24] M. Dion, H. Rydberg, E. Schröder, D. C. Langreth, and B. I. Lundqvist, Van der Waals Density Functional for General Geometries, *Phys. Rev. Lett.* **92**, 246401, doi:10.1103/PhysRevLett.92.246401 (2004). 6

[25] O. A. von Lilienfeld, I. Tavernelli, U. Rothlisberger, and D. Sebastiani, Optimization of Effective Atom Centered Potentials for London Dispersion Forces in Density Functional Theory, *Phys. Rev. Lett.* **93**, 153004, doi:10.1103/PhysRevLett.93.153004 (2004).

[26] S. Grimme, Semiempirical GGA-type density functional constructed with a long-range dispersion correction, *J. Comput. Chem.* **27**(15), 1787, doi:10.1002/jcc.20495 (2006). 6

[27] A. Tkatchenko and M. Scheffler, Accurate Molecular Van Der Waals Interactions from Ground-State Electron Density and Free-Atom Reference Data, *Phys. Rev. Lett.* **102**(7), 073005, doi:10.1103/PhysRevLett.102.073005 (2009). 6

[28] V. Ruiz, W. Liu, E. Zojer, M. Scheffler, and A. Tkatchenko, Density-Functional Theory with Screened van der Waals Interactions for the Modeling of Hybrid Inorganic-Organic Systems, *Phys. Rev. Lett.* **108**(14), 146103, doi:10.1103/PhysRevLett.108.146103 (2012). 6, 46, 52

[29] H. Hertz, Über einen Einfluss des ultravioletten Lichtes auf die electrische Entladung, *Ann. Phys.* **267**(8), 983, doi:10.1002/andp.18872670827 (1887). 9

[30] A. Einstein, Über einen die Erzeugung und Verwandlung des Lichtes betreffenden heuristischen Gesichtspunkt, *Ann. Phys.* **322**(6), 132, doi:10.1002/andp.19053220607 (1905). 9

[31] C. S. Fadley, S. T. Manson, and D. Dill, Electron Spectroscopy: Theory, Techniques and Applications, volume 2 (Academic Press, 1978). 9

[32] J. A. Knapp, F. J. Himpsel, and D. E. Eastman, Experimental energy band dispersions and lifetimes for valence and conduction bands of copper using angle-resolved photoemission, *Phys. Rev. B* **19**, 4952, doi:10.1103/PhysRevB.19.4952 (1979). 10

[33] F. Himpsel, Angle-resolved measurements of the photoemission of electrons in the study of solids, *Adv. Phys.* **32**(1), 1, doi:10.1080/00018738300101521 (1983). 10

[34] M. Born and R. Oppenheimer, Zur Quantentheorie der Molekeln, *Ann. Phys.* **389**(20), 457, doi:10.1002/andp.19273892002 (1927). 10

[35] F. Schreiber, A. Gerlach, N. Koch, E. Zojer, M. Sokolowski, F. S. Tautz, M. Rohlfing, and E. Umbach, Comment on 'Electron core-hole interaction and its induced ionic structural relaxation in molecular systems under x-ray irradiation', *Phys. Rev. Lett.* **99**, 059601, doi:10.1103/PhysRevLett.99.059601 (2007). 10

[36] A. Authier, Dynamical Theory of X-ray Diffraction (Oxford University Press, Oxford, 2003). 14

[37] B. W. Batterman and H. Cole, Dynamical Diffraction of X Rays by Perfect Crystals, *Rev. Mod. Phys.* **36**, 681, doi:10.1103/RevModPhys.36.681 (1964). 14

[38] D. P. Woodruff, D. L. Seymour, C. F. McConville, C. E. Riley, M. D. Crapper, N. Prince, and R. G. Jones, A simple X-ray standing wave technique for surface structure determination - theory and an application, *Surf. Sci.* **195**(1–2), 237, doi:10.1016/0039-6028(88)90794-7 (1988). 14, 82

[39] J. Zegenhagen, Surface-Structure Determination With X-Ray Standing Waves, *Surf. Sci. Rep.* **18**(7–8), 199, doi:10.1016/0167-5729(93)90025-K (1993). 19, 47, 82

[40] D. P. Woodruff, B. C. C. Cowie, and A. R. H. F. Ettema, Surface structure determination using X-ray standing waves: a simple view, *J. Phys.: Condens. Matter* **6**(49), 10633, doi:10.1088/0953-8984/6/49/007 (1994).

[41] M. J. Bedzyk, Encyclopedia of Condensed Matter Physics, volume 6, chapter Scattering: X-ray standing wave techniques, pages 330–341 (Elsevier, 2005). 14

[42] L. Cheng, P. Fenter, M. J. Bedzyk, and N. C. Sturchio, Fourier-Expansion Solution of Atom Distributions in a Crystal Using X-Ray Standing Waves, *Phys. Rev. Lett.* **90**(25), 255503, doi:10.1103/PhysRevLett.90.255503 (2003). 22, 82

[43] S. Thiess, T. L. Lee, C. T. Lin, L. X. Cao, C. Aruta, S. Warren, B. C. C. Cowie, and J. Zegenhagen, X-ray standing wave photoemission study of a $YBa_2Cu_3O_{7-\delta}$ single crystal, *Phys. Status Solidi B* **233**(3), R5, doi:10.1002/1521-3951(200210)233:33.0.CO;2-U (2002). 22

[44] J. Zegenhagen, B. Detlefs, T.-L. Lee, S. Thiess, H. Isern, L. Petit, L. André, J. Roy, Y. Mi, and I. Joumard, X-ray standing waves and hard X-ray photoelectron spectroscopy at the insertion device beamline ID32, *J. Electron Spectrosc. Relat. Phenom.* **178–179**(0), 258, doi:10.1016/j.elspec.2009.09.008 (2010). 22, 37

[45] I. Vartanyants, T.-L. Lee, S. Thiess, and J. Zegenhagen, Non-dipole effects in X-ray standing wave photoelectron spectroscopy experiments, *Nucl. Instrum. Methods Phys. Res., Sect. A* **547**(1), 196, doi:10.1016/j.nima.2005.05.025 (2005). 24

[46] C. Brouder, Angular dependence of X-ray absorption spectra, *J. Phys.: Condens. Matter* **2**(3), 701, doi:10.1088/0953-8984/2/3/018 (1990). 24

[47] J. W. Cooper, Multipole corrections to the angular distribution of photoelectrons at low energies, *Phys. Rev. A* **42**(11), 6942, doi:10.1103/PhysRevA.42.6942 (1990). 25

[48] T. E. Madey, J. T. Yates Jr., and N. E. Erickson, ESCA study of fractional monolayer quantities of chemisorbed gases on tungsten, *Chem. Phys. Lett.* **19**(4), 487, doi:10.1016/0009-2614(73)85132-2 (1973). 27

[49] A. F. Carley and M. W. Roberts, An X-Ray Photoelectron Spectroscopic Study of the Interaction of Oxygen and Nitric Oxide with Aluminium, *Proc. R. Soc. Lond. A* **363**(1714), 403, doi:10.1098/rspa.1978.0175 (1978). 27

[50] J. N. O'Shea, X-ray photoelectron spectroscopy and reactivity of alkali-doped Ni(110)-O surfaces, Ph.D. thesis, University of Wales, Cardiff, UK (1998). 27

[51] M. B. Trzhaskovskaya, V. I. Nefedov, and V. G. Yarzhemsky, Photoelectron angular distribution parameters for elements Z=1 to Z=54 in the photoelectron energy range 100-5000 eV, *Atom. Data Nucl. Data* **77**(1), 97, doi:10.1006/adnd.2000.0849 (2001). 27

[52] J. J. Lee, C. J. Fischer, D. P. Woodruff, M. G. Roper, R. G. Jones, and B. C. C. Cowie, Non-dipole Effect in Photoelectron-Monitored X-ray Standing Wave Experiments: Characterization and Calibration, *Surf. Sci.* **494**(3), 166, doi:10.1016/S0039-6028(01)01481-9 (2001). 27, 35, 37

[53] M. B. Trzhaskovskaya, V. I. Nefedov, and V. G. Yarzhemsky, Photoelectron angular distribution parameters for elements Z=55 to Z=100 in the photoelectron energy range 100-5000 eV, *Atom. Data Nucl. Data* **82**(2), 257, doi:10.1006/adnd.2002.0886 (2002). 27

[54] D. R. Penn, Quantitative chemical analysis by ESCA, *J. Electron Spectrosc. Relat. Phenom.* **9**(1), 29, doi:10.1016/0368-2048(76)85004-9 (1976). 28

[55] C. Wöll, S. Chiang, R. J. Wilson, and P. H. Lippel, Determination of atom positions at stacking-fault dislocations on Au(111) by scanning tunneling microscopy, *Phys. Rev. B* **39**, 7988, doi:10.1103/PhysRevB.39.7988 (1989). 31

[56] A. R. Sandy, S. G. J. Mochrie, D. M. Zehner, K. G. Huang, and D. Gibbs, Structure and phases of the Au(111) surface: X-ray-scattering measurements, *Phys. Rev. B* **43**, 4667, doi:10.1103/PhysRevB.43.4667 (1991). 31

[57] F. Comin, R. de Martino, K. Fezzaa, V. Formoso, L. Ortega, and R. Signorato, ESRF ID32, SEXAFS and Standing Waves Beamline: An Open Architecture Setup for Surface Studies, *J. Phys. IV France* **7**(C2), 343, doi:10.1051/jp4/1997013 (1997). 35

[58] F. Schreiber, K. A. Ritley, I. A. Vartanyants, H. Dosch, J. Zegenhagen, and B. C. C. Cowie, Non-dipolar contributions in XPS detection of X-ray standing waves, *Surf. Sci.* **486**(3), L519, doi:10.1016/S0039-6028(01)00993-1 (2001). 35, 37

[59] C. Stadler, S. Hansen, A. Schöll, T.-L. Lee, J. Zegenhagen, C. Kumpf, and E. Umbach, Molecular distortion of NTCDA upon adsorption on Ag(111): A normal incidence x-ray standing wave study, *New J. Phys.* **9**(3), 50, doi:10.1088/1367-2630/9/3/050 (2007). 37, 101, 105

[60] A. Bechler and R. H. Pratt, Higher retardation and multipole corrections to the dipole angular momentum of 1s photoelectrons at low energies, *Phys. Rev. A* **39**, 1774, doi:10.1103/PhysRevA.39.1774 (1989). 37

[61] C. Bürker, N. Ferri, A. Tkatchenko, A. Gerlach, J. Niederhausen, T. Hosokai, S. Duhm, J. Zegenhagen, N. Koch, and F. Schreiber, Exploring the bonding of large hydrocarbons on noble metals: Diindoperylene on Cu(111), Ag(111), and Au(111), *Phys. Rev. B* **87**(16), 165443, doi:10.1103/PhysRevB.87.165443 (2013). 46, 82, 98, 101, 104, 105

[62] N. Atodiresei, V. Caciuc, P. Lazić, and S. Blügel, Chemical versus van der Waals Interaction: The Role of the Heteroatom in the Flat Absorption of Aromatic Molecules C_6H_6, C_5NH_5, and $C_4N_2H_4$ on the Cu(110) Surface, *Phys. Rev. Lett.* **102**, 136809, doi:10.1103/PhysRevLett.102.136809 (2009). 46

[63] G. Mercurio, E. R. McNellis, I. Martin, S. Hagen, F. Leyssner, S. Soubatch, J. Meyer, M. Wolf, P. Tegeder, F. S. Tautz, and K. Reuter, Structure and Energetics of Azobenzene on Ag(111): Benchmarking Semiempirical Dispersion Correction Approaches, *Phys. Rev. Lett.* **104**(3), 036102, doi:10.1103/PhysRevLett.104.036102 (2010). 46, 101, 105

[64] D. Stradi, S. Barja, C. Díaz, M. Garnica, B. Borca, J. J. Hinarejos, D. Sánchez-Portal, M. Alcamí, A. Arnau, A. L. Vázquez de Parga, R. Miranda, and F. Martín, Role of Dispersion Forces in the Structure of Graphene Monolayers on Ru Surfaces, *Phys. Rev. Lett.* **106**, 186102, doi:10.1103/PhysRevLett.106.186102 (2011).

[65] T. Olsen, J. Yan, J. J. Mortensen, and K. S. Thygesen, Dispersive and Covalent Interactions between Graphene and Metal Surfaces from the Random Phase Approximation, *Phys. Rev. Lett.* **107**, 156401, doi:10.1103/PhysRevLett.107.156401 (2011).

[66] E. McNellis, Ph.D. thesis, Fritz-Haber-Institut der Max-Planck-Gesellschaft (2010). 46

[67] A. C. Dürr, F. Schreiber, K. A. Ritley, V. Kruppa, J. Krug, H. Dosch, and B. Struth, Rapid Roughening in Thin Film Growth of an Organic Semiconductor (Diindenoperylene), *Phys. Rev. Lett.* **90**(1), 016104, doi:10.1103/PhysRevLett.90.016104 (2003). 46

[68] S. Kowarik, A. Gerlach, S. Sellner, F. Schreiber, L. Cavalcanti, and O. Konovalov, Real-Time Observation of Structural and Orientational Transitions during Growth of Organic Thin Films, *Phys. Rev. Lett.* **96**(12), 125504, doi:10.1103/PhysRevLett.96.125504 (2006).

[69] U. Heinemeyer, K. Broch, A. Hinderhofer, M. Kytka, R. Scholz, A. Gerlach, and F. Schreiber, Real-Time Changes in the Optical Spectrum of Organic Semiconducting Films and Their Thickness Regimes during Growth, *Phys. Rev. Lett.* **104**(25), 257401, doi:10.1103/PhysRevLett.104.257401 (2010).

[70] J. Wagner, M. Gruber, A. Hinderhofer, A. Wilke, B. Bröker, J. Frisch, P. Amsalem, A. Vollmer, A. Opitz, N. Koch, F. Schreiber, and W. Brütting, High Fill Factor and Open Circuit Voltage in Organic Photovoltaic Cells with Diindenoperylene as Donor Material, *Adv. Funct. Mater.* **20**(24), 4295, doi:10.1002/adfm.201001028 (2010). 46

[71] D. G. de Oteyza, E. Barrena, H. Dosch, and Y. Wakayama, Nanoconfinement effects in the self-assembly of diindenoperylene (DIP) on Cu(111) surfaces, *Phys. Chem. Chem. Phys.* **11**(39), 8741, doi:10.1039/b903116b (2009). 46, 119

[72] H. Huang, J.-T. Sun, Y. P. Feng, W. Chen, and A. T. S. Wee, Epitaxial growth of diindenoperylene ultrathin films on Ag(111) investigated by LT-STM and LEED, *Phys. Chem. Chem. Phys.* **13**(47), 20933, doi:10.1039/c1cp22769f (2011). 51, 119

[73] D. de Oteyza, E. Barrena, M. Ruiz-Osés, I. Silanes, B. Doyle, J. Ortega, A. Arnau, H. Dosch, and Y. Wakayama, Crystallographic and Electronic Structure of Self-Assembled DIP Monolayers on Au(111) Substrates, *J. Phys. Chem. C* **112**(18), 7168, doi:10.1021/jp800631p (2008). 46, 119

[74] S. K. M. Henze, O. Bauer, T.-L. Lee, M. Sokolowski, and F. S. Tautz, Vertical bonding distances of PTCDA on Au(111) and Ag(111): Relation to the bonding type, *Surf. Sci.* **601**(6), 1566, doi:10.1016/j.susc.2007.01.020 (2007). 46, 47, 54, 55, 60, 82, 101, 104, 105

[75] J. Ziroff, F. Forster, A. Schöll, P. Puschnig, and F. Reinert, Hybridization of Organic Molecular Orbitals with Substrate States at Interfaces: PTCDA on Silver, *Phys. Rev. Lett.* **104**(23), 233004, doi:10.1103/PhysRevLett.104.233004 (2010). 46

[76] L. Kilian, A. Hauschild, R. Temirov, S. Soubatch, A. Schöll, A. Bendounan, F. Reinert, T.-L. Lee, F. S. Tautz, M. Sokolowski, and E. Umbach, Role of Intermolecular Interactions on the Electronic and Geometric Structure of a Large π-Conjugated Molecule Adsorbed on a Metal Surface, *Phys. Rev. Lett.* **100**(13), 136103, doi:10.1103/PhysRevLett.100.136103 (2008). 46, 82, 101, 105

[77] S. Krause, Determination of the transport levels in thin films of organic semiconductors, Ph.D. thesis, Universität Würzburg (2009). 46

[78] S. Krause, A. Schöll, and E. Umbach, Interplay of geometric and electronic structure in thin films of diindenoperylene on Ag(111), *Org. Electron.* **14**(2), 584, doi:10.1016/j.orgel.2012.11.023 (2013). 46

[79] A. Gerlach, T. Hosokai, S. Duhm, S. Kera, O. T. Hofmann, E. Zojer, J. Zegenhagen, and F. Schreiber, Orientational Ordering of Nonplanar Phthalocyanines on Cu(111): Strength and Orientation of the Electric Dipole Moment, *Phys. Rev. Lett.* **106**(15), 156102, doi:10.1103/PhysRevLett.106.156102 (2011). 50, 78, 82, 92, 98, 105

[80] L. W. Bruch, R. D. Diehl, and J. A. Venables, Progress in the measurement and modeling of physisorbed layers, *Rev. Mod. Phys.* **79**, 1381, doi:10.1103/RevModPhys.79.1381 (2007). 52

[81] L. W. Bruch, M. W. Cole, and E. Zaremba, Physical Adsorption: Forces and Phenomena (Dover, New Yorkd, 2009). 52

[82] E. M. Lifshitz, The Theory of Molecular Attractive Forces between Solids, *Soviet Physics JETP* **2**, 73 (1956). 52

[83] E. Zaremba and W. Kohn, Van der Waals interaction between an atom and a solid surface, *Phys. Rev. B* **13**, 2270 (1976). 52

[84] G. Heimel, S. Duhm, I. Salzmann, A. Gerlach, A. Strozecka, J. Niederhausen, C. Bürker, T. Hosokai, I. Fernandez-Torrente, G. Schulze, S. Winkler, A. Wilke, R. Schlesinger, J. Frisch, B. Bröker, A. Vollmer, B. Detlefs, J. Pflaum, S. Kera, K. J. Franke, N. Ueno, J. I. Pascual, F. Schreiber, and N. Koch, Charged and metallic molecular monolayers through surface-induced aromatic stabilization, *Nature Chem.* **5**(3), 187, doi:10.1038/nchem.1572 (2013). 53, 71, 73, 77, 99, 103, 104, 105, 106, 119

[85] B. Stadtmüller, I. Kröger, F. Reinert, and C. Kumpf, Submonolayer growth of CuPc on noble metal surfaces, *Phys. Rev. B* **83**(8), 085416, doi:10.1103/PhysRevB.83.085416 (2011). 55, 80, 82

[86] I. Kröger, B. Stadtmüller, C. Kleimann, P. Rajput, and C. Kumpf, Normal-incidence x-ray standing-wave study of copper phthalocyanine submonolayers on Cu(111) and Au(111), *Phys. Rev. B* **83**(19), 195414, doi:10.1103/PhysRevB.83.195414 (2011). 57, 60, 64, 78, 80, 90, 99, 104, 105

[87] C. Wagner, D. Kasemann, C. Golnik, R. Forker, M. Esslinger, K. Müllen, and T. Fritz, Repulsion between Molecules on a Metal: Monolayers and Submonolayers of Hexa-*peri*-hexabenzocoronene on Au(111), *Phys. Rev. B* **81**(3), 035423, doi:10.1103/PhysRevB.81.035423 (2010). 57, 119

[88] G. White and J. Collins, Thermal expansion of copper, silver, and gold at low temperatures, *J. Low Temp. Phys.* **7**(1–2), 43, doi:10.1007/BF00629120 (1972). 58

[89] Y. S. Touloukian, R. K. Kirby, R. E. Taylor, and P. D. Desai, Thermophysical Properties of Matter. Vol. 12: Thermal Expansion - Metallic Elements and Alloys (IFI Plenum, NewYork-Washington, 1975). 58

[90] D. Käfer, C. Wöll, and G. Witte, Thermally activated dewetting of organic thin films: The case of pentacene on SiO_2 and gold, *Appl. Phys. A* **95**(1), 273, doi:10.1007/s00339-008-5011-3 (2009). 60, 115, 117

[91] S. Duhm, C. Bürker, J. Niederhausen, I. Salzmann, T. Hosokai, J. Duvernay, S. Kera, F. Schreiber, N. Koch, N. Ueno, and A. Gerlach, Pentacene on Ag(111): Correlation of Bonding Distance with Intermolecular Interaction and Order, *ACS Appl. Mater. Interfaces* **5**(19), 9377, doi:10.1021/am402778u (2013). 61, 64, 89, 103, 106, 107

[92] D. Käfer and G. Witte, Evolution of pentacene films on Ag(111): Growth beyond the first monolayer, *Chem. Phys. Lett.* **442**(4-6), 376, doi:10.1016/j.cplett.2007.06.006 (2007). 61

[93] N. Koch, I. Salzmann, R. Johnson, J. Pflaum, R. Friedlein, and J. Rabe, Molecular orientation dependent energy levels at interfaces with pentacene and pentacenequinone, *Org. Electron.* **7**(6), 537, doi:10.1016/j.orgel.2006.07.010 (2006). 61

[94] E. Mete, I. Demiroğlu, M. F. Fatih Danışman, and c. Ellialtıoğlu, Pentacene Multilayers on Ag(111) Surface, *J. Phys. Chem. C* **114**(6), 2724, doi:10.1021/jp910703n (2010). 61, 62

[95] M. Eremtchenko, R. Temirov, D. Bauer, J. Schaefer, and F. Tautz, Formation of molecular order on a disordered interface layer: Pentacene/Ag(111), *Phys. Rev. B* **72**(11), 115430, doi:10.1103/PhysRevB.72.115430 (2005). 61

[96] D. B. Dougherty, W. Jin, W. G. Cullen, J. E. Reutt-Robey, and S. W. Robey, Variable Temperature Scanning Tunneling Microscopy of Pentacene Monolayer and Bilayer Phases on Ag(111), *J. Phys. Chem. C* **112**(51), 20334, doi:10.1021/jp804682v (2008). 61

[97] M. F. Danışman, L. Casalis, and G. Scoles, Supersonic molecular beam deposition of pentacene thin films on two Ag(111) surfaces with different step densities, *Phys. Rev. B* **72**(8), 085404, doi:10.1103/PhysRevB.72.085404 (2005). 61

[98] S. Duhm, S. Hosoumi, I. Salzmann, A. Gerlach, M. Oehzelt, B. Wedl, T.-L. Lee, F. Schreiber, N. Koch, N. Ueno, and S. Kera, Influence of intramolecular polar bonds on interface energetics in perfluoro-pentacene on Ag(111), *Phys. Rev. B* **81**(4), 045418, doi:10.1103/PhysRevB.81.045418 (2010). 65, 103, 105

[99] I. Salzmann, S. Duhm, G. Heimel, M. Oehzelt, R. Kniprath, R. L. Johnson, J. P. Rabe, and N. Koch, Tuning the Ionization Energy of Organic Semiconductor Films: The Role of Intramolecular Polar Bonds, *J. Am. Chem. Soc.* **130**(39), 12870, doi:10.1021/ja804793a (2008). 65

[100] A. Hinderhofer, U. Heinemeyer, A. Gerlach, S. Kowarik, R. M. J. Jacobs, Y. Sakamoto, T. Suzuki, and F. Schreiber, Optical properties of pentacene and perfluoropentacene thin films, *J. Chem. Phys.* **127**, 194705, doi:10.1063/1.2786992 (2007).

[101] C. Frank, J. Novák, A. Gerlach, G. Ligorio, K. Broch, A. Hinderhofer, A. Aufderheide, R. Banerjee, R. Nervo, and F. Schreiber, Real-time X-ray scattering studies on temperature dependence of perfluoropentacene thin film growth, *J. Appl. Phys.* **114**(4), 043515, doi:10.1063/1.4816320 (2013). 65

[102] K. Broch, U. Heinemeyer, A. Hinderhofer, F. Anger, R. Scholz, A. Gerlach, and F. Schreiber, Optical evidence for intermolecular coupling in mixed films of pentacene and perfluoropentacene, *Phys. Rev. B* **83**, 245307, doi:10.1103/PhysRevB.83.245307 (2011). 65

[103] A. Hinderhofer, C. Frank, T. Hosokai, A. Resta, A. Gerlach, and F. Schreiber, Structure and morphology of coevaporated pentacene-perfluoropentacene thin films, *J. Chem. Phys.* **134**(10), 104702, doi:10.1063/1.3557476 (2011).

[104] S. Duhm, I. Salzmann, G. Heimel, M. Oehzelt, A. Haase, R. L. Johnson, J. P. Rabe, and N. Koch, Controlling energy level offsets in organic/organic heterostructures using intramolecular polar bonds, *Appl. Phys. Lett.* **94**(3), 033304, doi:10.1063/1.3073046 (2009).

[105] I. Salzmann, S. Duhm, G. Heimel, J. P. Rabe, N. Koch, M. Oehzelt, Y. Sakamoto, and T. Suzuki, Structural Order in Perfluoropentacene Thin Films and Heterostructures with Pentacene, *Langmuir* **24**(14), 7294, doi:10.1021/la800606h (2008).

[106] A. Hinderhofer, A. Gerlach, S. Kowarik, F. Zontone, J. Krug, and F. Schreiber, Smoothing and coherent structure formation in organic-organic heterostructure growth, *EPL* **91**, 56002, doi:10.1209/0295-5075/91/56002 (2010).

[107] S. Kowarik, K. Broch, A. Hinderhofer, A. Schwartzberg, J. O. Ossó, D. Kilcoyne, F. Schreiber, and S. R. Leone, Crystal grain orientation in organic homo- and heteroepitaxy of pentacene and perfluoropentacene studied with X-ray spectromicroscopy, *J. Phys. Chem. C* **114**, 13061, doi:10.1021/jp103713z (2010). 65

[108] S. Söhnchen, S. Lukas, and G. Witte, Epitaxial growth of pentacene films on Cu(110), *J. Chem. Phys.* **121**(1), 525, doi:10.1063/1.1760076 (2004). 65

[109] H. Glowatzki, G. Heimel, A. Vollmer, S. L. Wong, H. Huang, W. Chen, A. T. S. Wee, J. P. Rabe, and N. Koch, Impact of Fluorination on Initial Growth and Stability of Pentacene on Cu(111), *J. Phys. Chem. C* **116**(14), 7726, doi:10.1021/jp208582z (2012). 66, 67

[110] J. Götzen, C. H. Schwalb, C. Schmidt, G. Mette, M. Marks, U. Höfer, and G. Witte, Structural Evolution of Perfluoro-Pentacene Films on Ag(111): Transition from 2D to 3D Growth, *Langmuir* **27**(3), 993, doi:10.1021/la1022664 (2011). 66, 67

[111] J. C. Collings, K. P. Roscoe, R. L. Thomas, A. S. Batsanov, L. M. Stimson, J. A. K. Howard, and T. B. Marder, Arene-perfluoroarene interactions in crystal engineering. Part 3. Single-crystal structures of 1:1 complexes of octafluoronaphthalene with fused-ring polyaromatic hydrocarbons, *New J. Chem.* **25**, 1410, doi:10.1039/B105502J (2001). 70

[112] B. Stadtmüller, T. Sueyoshi, G. Kichin, I. Kröger, S. Soubatch, R. Temirov, F. S. Tautz, and C. Kumpf, Commensurate Registry and Chemisorption at a Hetero-organic Interface, *Phys. Rev. Lett.* **108**, 106103, doi:10.1103/PhysRevLett.108.106103 (2012). 70, 105, 107

[113] J. Blochwitz, M. Pfeiffer, T. Fritz, and K. Leo, Low voltage organic light emitting diodes featuring doped phthalocyanine as hole transport material, *Appl. Phys. Lett.* **73**(6), 729, doi:10.1063/1.121982 (1998). 78

[114] P. Peumans and S. R. Forrest, Very-high-efficiency double-heterostructure copper phthalocyanine/C_{60} photovoltaic cells, *Appl. Phys. Lett.* **79**(1), 126, doi:10.1063/1.1384001 (2001). 78

[115] H. Yamane, A. Gerlach, S. Duhm, Y. Tanaka, T. Hosokai, Y. Y. Mi, J. Zegenhagen, N. Koch, K. Seki, and F. Schreiber, Site-Specific Geometric and Electronic Relaxations at Organic-Metal Interfaces, *Phys. Rev. Lett.* **105**(4), 046103, doi:10.1103/PhysRevLett.105.046103 (2010). 78, 98, 105

[116] D. G. de Oteyza, A. El-Sayed, J. M. Garcia-Lastra, E. Goiri, T. N. Krauss, A. Turak, E. Barrena, H. Dosch, J. Zegenhagen, A. Rubio, Y. Wakayama, and J. E. Ortega, Copper-phthalocyanine based metal–organic interfaces: The effect of fluorination, the substrate, and its symmetry, *J. Chem. Phys.* **133**(21), 214703, doi:10.1063/1.3509394 (2010). 78, 99, 104

[117] I. Kröger, P. Bayersdorfer, B. Stadtmüller, C. Kleimann, G. Mercurio, F. Reinert, and C. Kumpf, Submonolayer growth of H_2-phthalocyanine on Ag(111), *Phys. Rev. B* **86**(19), 195412, doi:10.1103/PhysRevB.86.195412 (2012). 78, 80, 89, 103, 105

[118] B. Cordero, V. Gómez, A. E. Platero-Prats, M. Revés, J. Echeverría, E. Cremades, F. Barragán, and S. Alvarez, Covalent radii revisited, *Dalton Trans.* (21), 2832, doi:10.1039/B801115J (2008). 80

[119] Y. Yamagishi, S. Nakashima, K. Oiso, and T. K. Yamada, Recovery of nanomolecular electronic states from tunneling spectroscopy: LDOS of low-dimensional phthalocyanine molecular structures on Cu(111), *Nanotechnology* **24**(39), 395704, doi:10.1088/0957-4484/24/39/395704 (2013). 80

[120] C. Bürker, A. Franco-Cañellas, K. Broch, T.-L. Lee, A. Gerlach, and F. Schreiber, Self-Metalation of 2*H*-Tetraphenylporphyrin on Cu(111) Studied with XSW: Influence of the Central Metal Atom on the Adsorption Distance, *J. Phys. Chem. C* **118**(25), 13659, doi:10.1021/jp503046w (2014). 81

[121] J. M. Gottfried, K. Flechtner, A. Kretschmann, T. Lukasczyk, and H.-P. Steinrück, Direct Synthesis of a Metalloporphyrin Complex on a Surface, *J. Am. Chem. Soc.* **128**(17), 5644, doi:10.1021/ja0610333 (2006). 81

[122] T. E. Shubina, H. Marbach, K. Flechtner, A. Kretschmann, N. Jux, F. Buchner, H.-P. Steinrück, T. Clark, and J. M. Gottfried, Principle and Mechanism of Direct Porphyrin Metalation: Joint Experimental and Theoretical Investigation, *J. Am. Chem. Soc.* **129**(30), 9476, doi:10.1021/ja072360t (2007). 81, 82, 89

[123] F. Buchner, V. Schwald, K. Comanici, H.-P. Steinrück, and H. Marbach, Microscopic Evidence of the Metalation of a Free-Base Porphyrin Monolayer with Iron, *ChemPhysChem* **8**(2), 241, doi:10.1002/cphc.200600698 (2007). 81

[124] R. González-Moreno, C. Sánchez-Sánchez, M. Trelka, R. Otero, A. Cossaro, A. Verdini, L. Floreano, M. Ruiz-Bermejo, A. García-Lekue, J. Á. Martín-Gago, and C. Rogero, Following the Metalation Process of Protoporphyrin IX with Metal Substrate Atoms at Room Temperature, *J. Phys. Chem. C* **115**(14), 6849, doi:10.1021/jp200533a (2011). 81

[125] A. Goldoni, C. A. Pignedoli, G. Di Santo, C. Castellarin-Cudia, E. Magnano, F. Bondino, A. Verdini, and D. Passerone, Room Temperature Metalation of 2H-TPP Monolayer on Iron and Nickel Surfaces by Picking up Substrate Metal Atoms, *ACS Nano* **6**(12), 10800, doi:10.1021/nn304134q (2012). 81

[126] K. Diller, F. Klappenberger, M. Marschall, K. Hermann, A. Nefedov, C. Wöll, and J. V. Barth, Self-metalation of 2H-tetraphenylporphyrin on Cu(111): An x-ray spectroscopy study, *J. Chem. Phys.* **136**(1), 014705, doi:10.1063/1.3674165 (2012). 81, 82, 84, 89, 90

[127] J. Xiao, S. Ditze, M. Chen, F. Buchner, M. Stark, M. Drost, H.-P. Steinrück, J. M. Gottfried, and H. Marbach, Temperature-Dependent Chemical and Structural Transformations from 2*H*-tetraphenylporphyrin to Copper(II)-Tetraphenylporphyrin on Cu(111), *J. Phys. Chem. C* **116**(22), 12275, doi:10.1021/jp301757h (2012). 81, 82

[128] F. Buchner, J. Xiao, E. Zillner, M. Chen, M. Röckert, S. Ditze, M. Stark, H.-P. Steinrück, J. M. Gottfried, and H. Marbach, Diffusion, Rotation, and Surface Chemical Bond of Individual 2*H*-Tetraphenylporphyrin Molecules on Cu(111), *J. Phys. Chem. C* **115**(49), 24172, doi:10.1021/jp206675u (2011). 81, 82

[129] A. Gerlach, C. Bürker, T. Hosokai, and F. Schreiber, X-Ray Standing Waves and Surfaces X-Ray Scattering Studies of Molecule–Metal Interfaces, in: The Molecule-Metal Interface (WILEY-VCH Verlag, 2013). 82

[130] F. Buchner, E. Zillner, M. Röckert, S. Gläßel, H.-P. Steinrück, and H. Marbach, Substrate-Mediated Phase Separation of Two Porphyrin Derivatives on Cu(111), *Chem. Eur. J.* **17**(37), 10226, doi:10.1002/chem.201100462 (2011). 89

[131] D. A. Duncan, W. Unterberger, K. A. Hogan, T. J. Lerotholi, C. L. A. Lamont, and D. P. Woodruff, A photoelectron diffraction investigation of vanadyl phthalocyanine on Au(111), *Surf. Sci.* **604**, 47, doi:10.1016/j.susc.2009.10.018 (2010). 92

[132] T. Cambridge Crystallographic Data Center doi:http://www.ccdc.cam.ac.uk/pages/Home.aspx. 95

[133] T. Niu, M. Zhou, J. Zhang, Y. Feng, and W. Chen, Dipole Orientation Dependent Symmetry Reduction of Chloroaluminum Phthalocyanine on Cu(111), *J. Phys. Chem. C* **117**(2), 1013, doi:10.1021/jp310196k (2013). 96

[134] S.-H. Chang, S. Kuck, J. Brede, L. Lichtenstein, G. Hoffmann, and R. Wiesendanger, Symmetry reduction of metal phthalocyanines on metals, *Phys. Rev. B* **78**, 233409, doi:10.1103/PhysRevB.78.233409 (2008). 96

[135] R. Cuadrado, J. I. Cerdá, Y. Wang, G. Xin, R. Berndt, and H. Tang, CoPc adsorption on Cu(111): Origin of the C4 to C2 symmetry reduction, *J. Chem. Phys.* **133**(15), 154701, doi:10.1063/1.3502682 (2010). 96

[136] J. Haase and H.-J. Kuhr, Reconstruction and relaxation of the oxygen-covered Cu(111) surface: A sexafs study, *Surf. Sci.* **203**(3), L695, doi:10.1016/0039-6028(88)90084-2 (1988). 97

[137] B. Luo and J. Urban, Structure determination of oxygen adsorbates on Cu surfaces by means of the SEELFS technique, *J. Phys.: Condens. Matter* **3**(17), 2873, doi:10.1088/0953-8984/3/17/005 (1991). 97

[138] S. M. Johnston, A. Mulligan, V. Dhanak, and M. Kadodwala, The Structure of Methanol and Methoxy on Cu(111), *Surf. Sci.* **530**, 111, doi:10.1016/S0039-6028(03)00385-6 (2003). 97

[139] P. Hofmann, K.-M. Schindler, S. Bao, V. Fritzsche, D. Ricken, A. Bradshaw, and D. Woodruff, The geometric structure of the surface methoxy species on Cu(111), *Surf. Sci.* **304**(1–2), 74, doi:10.1016/0039-6028(94)90754-4 (1994). 97

[140] L. Romaner, G. Heimel, J. L. Bredas, A. Gerlach, F. Schreiber, R. L. Johnson, J. Zegenhagen, S. Duhm, N. Koch, and E. Zojer, Impact of bidirectional charge transfer and molecular distortions on the electronic structure of a metal-organic interface, *Phys. Rev. Lett.* **99**, 256801, doi:10.1103/PhysRevLett.99.256801 (2007). 100, 105

[141] A. Hauschild, R. Temirov, S. Soubatch, O. Bauer, A. Schöll, B. C. C. Cowie, T.-L. Lee, F. S. Tautz, and M. Sokolowski, Normal-incidence x-ray standing-wave determination of the adsorption geometry of PTCDA on Ag(111): Comparison of the ordered room-temperature and disordered low-temperature phases, *Phys. Rev. B* **81**(12), 125432, doi:10.1103/PhysRevB.81.125432 (2010). 101

[142] J. Stanzel, W. Weigand, L. Kilian, H. L. Meyerheim, C. Kumpf, and E. Umbach, Chemisorption of NTCDA on Ag(111): a NIXSW study including non-dipolar and electron-stimulated effects, *Surf. Sci.* **571**(1-3), L311, doi:10.1016/j.susc.2004.07.048 (2004). 101

[143] E. R. McNellis, G. Mercurio, S. Hagen, F. Leyssner, J. Meyer, S. Soubatch, M. Wolf, K. Reuter, P. Tegeder, and F. S. Tautz, Bulky spacer groups – A valid strategy to control the coupling of functional molecules to surfaces?, *Chem. Phys. Lett.* **499**(4–6), 247, doi:10.1016/j.cplett.2010.09.051 (2010). 101

[144] C. Stadler, S. Hansen, F. Pollinger, C. Kumpf, E. Umbach, T.-L. Lee, and J. Zegenhagen, Structural investigation of the adsorption of SnPc on Ag(111) using normal-incidence x-ray standing waves, *Phys. Rev. B* **74**(3), 035404, doi:10.1103/PhysRevB.74.035404 (2006). 102

[145] L. Kilian, W. Weigang, , E. Umbach, A. Langner, M. Sokolowski, H. L. Meyerheim, H. Maltor, B. C. C. Cowie, T. Lee, and P. Bäuerle, Adsorption Site Determination of a Large π-conjugated Molecule by Normal Incidence X-ray Standing Waves: End-capped Quaterthiophene on Ag(111), *Phys. Rev. B* **66**(7), 075412, doi:10.1103/PhysRevB.66.075412 (2002). 103

[146] C. Kleimann, B. Stadtmüller, S. Schröder, and C. Kumpf, Electrostatic Interaction and Commensurate Registry at the Heteromolecular F_{16}CuPc-CuPc Interface, *J. Phys. Chem. C* **118**(3), 1652, doi:10.1021/jp411289j (2014). 105

[147] S. Duhm, A. Gerlach, O. T. Hofmann, B. Bröker, C. Bürker, J. Niederhausen, I. Salzmann, T. Hosokai, J. Zegenhagen, A. Vollmer, R. Rieger, S. Kera, K. Müllen, F. Schreiber, E. Zojer, and N. Koch, Surface-induced aromatic stabilization of disc-like conjugated molecules, *in preparation* . 106

[148] O. Bauer, G. Mercurio, M. Willenbockel, W. Reckien, C. Heinrich Schmitz, B. Fiedler, S. Soubatch, T. Bredow, F. S. Tautz, and M. Sokolowski, Role of functional groups in surface bonding of planar π-conjugated molecules, *Phys. Rev. B* **86**, 235431, doi:10.1103/PhysRevB.86.235431 (2012). 108

[149] S. Blumstengel, N. Koch, S. Sadofev, P. Schäfer, H. Glowatzki, R. L. Johnson, J. P. Rabe, and F. Henneberger, Interface formation and electronic structure of α-sexithiophene on ZnO, *Appl. Phys. Lett.* **92**(19), 193303, doi:10.1063/1.2918089 (2008). 108

[150] K. Oura, V. Lifshits, A. Saranin, A. Zotov, and M. Katayama, Surface Science: An Introduction (Springer, 2003). 113, 114

[151] K. A. Fichthorn and R. A. Miron, Thermal Desorption of Large Molecules from Solid Surfaces, *Phys. Rev. Lett.* **89**, 196103, doi:10.1103/PhysRevLett.89.196103 (2002). 114

[152] K. R. Paserba and A. J. Gellman, Kinetics and Energetics of Oligomer Desorption from Surfaces, *Phys. Rev. Lett.* **86**, 4338, doi:10.1103/PhysRevLett.86.4338 (2001). 114

[153] T. Wagner, H. Karacuban, A. Bannani, C. Bobisch, and R. Möller, Thermal Desorption of PTCDA on Cu(111), *J. Phys.: Conf. Ser.* **100**(5), 052068, doi:10.1088/1742-6596/100/5/052068 (2008). 115

[154] S. L. Wong, H. Huang, Y. L. Huang, Y. Z. Wang, X. Y. Gao, T. Suzuki, W. Chen, and A. T. S. Wee, Effect of Fluorination on the Molecular Packing of Perfluoropentacene and Pentacene Ultrathin Films on Ag (111), *J. Phys. Chem. C* **114**(20), 9356, doi:10.1021/jp910581b (2010). 119

List of Publications

1. C. Bürker, A. Franco-Cañellas, K. Broch, T.-L. Lee, A. Gerlach, and F. Schreiber, Self-metalation of 2H-tetraphenylporphyrin on Cu(111) Studied with XSW: Influence of the Central Metal Atom on the Adsorption Distance, *J. Phys. Chem. C* **118**(25), 13659 doi:10.1021/jp503046w (2014).

2. S. Duhm, A. Gerlach, O. T. Hofmann, B. Bröker, C. Bürker, J. Niederhausen, I. Salzmann, T. Hosokai, J. Zegenhagen, A. Vollmer, R. Rieger, S. Kera, K. Müllen, F. Schreiber, E. Zojer, and N. Koch, Surface-induced aromatic stabilization of disc-like conjugated molecules, *in preparation* .

3. H. Glowatzki, B. Bröker, S. Duhm, G. Ranger, J. Niederhausen, C. Bürker, T. Hosokai, R. Blum, R. Rieger, A. Vollmer, P. Rajput, A. Gerlach, S. Kera, F. Schreiber, K. Müllen, J. P. Rabe, E. Zojer, and N. Koch, High molecular weight organic electron acceptor molecules, *in preparation* .

4. J. Niederhausen, S. Duhm, G. Heimel, C. Bürker, Q. Xin, A. Wilke, A. Vollmer, F. Schreiber, S. Kera, J. P. Rabe, N. Ueno, and N. Koch, Seleno groups control the energy-level alignment between conjugated organic molecules and metals, *J. Chem. Phys.* **140**(1), 014705, doi:http://dx.doi.org/10.1063/1.4858856 (2014).

5. K. Broch, C. Bürker, J. Dieterle, S. Krause, A. Gerlach, and F. Schreiber, Impact of molecular tilt angle on the absorption spectra of pentacene:perfluoropentacene blends, *Phys. Status Solidi RRL* **7**(12), 1084, doi:10.1002/pssr.201308085 (2013).

6. S. Duhm, C. Bürker, J. Niederhausen, I. Salzmann, T. Hosokai, J. Duvernay, S. Kera, F. Schreiber, N. Koch, N. Ueno, and A. Gerlach, Pentacene on Ag(111): Correlation of Bonding Distance with Intermolecular Interaction and Order, *ACS Appl. Mater. Interfaces* **5**(19), 9377, doi:10.1021/am402778u (2013).

7. A. Gerlach, C. Bürker, T. Hosokai, and F. Schreiber, X-Ray Standing Waves and Surfaces X-Ray Scattering Studies of Molecule–Metal Interfaces, in N. Koch, N. Ueno, and A. Wee (Editors), The Molecule-Metal Interface (WILEY-VCH Verlag, 2013).

8. C. Bürker, N. Ferri, A. Tkatchenko, A. Gerlach, J. Niederhausen, T. Hosokai, S. Duhm, J. Zegenhagen, N. Koch, and F. Schreiber, Exploring the bonding of large hydrocarbons on noble metals: Diindoperylene on Cu(111), Ag(111), and Au(111), *Phys. Rev. B* **87**(16), 165443, doi:10.1103/PhysRevB.87.165443 (2013).

9. G. Heimel, S. Duhm, I. Salzmann, A. Gerlach, A. Strozecka, J. Niederhausen, C. Bürker, T. Hosokai, I. Fernandez-Torrente, G. Schulze, S. Winkler, A. Wilke, R. Schlesinger, J. Frisch, B. Bröker, A. Vollmer, B. Detlefs, J. Pflaum, S. Kera, K. J. Franke, N. Ueno, J. I. Pascual, F. Schreiber, and N. Koch, Charged and metallic molecular monolayers through surface-induced aromatic stabilization, *Nature Chem.* **5**(3), 187, doi:10.1038/nchem.1572 (2013).

Danksagung

Ich möchte mich bei folgenden Personen bedanken, die mich während dieser Arbeit begleitet haben:

- Im Besonderen möchte ich mich bei meinem Doktorvater Frank Schreiber bedanken. Dafür, dass er diese Arbeit ermöglicht hat und mich während der Arbeit mit fachlichen Diskussionen begleitet hat.
- Reinhold Fink möchte ich für seine Bereitschaft danken, diese Arbeit fachlich zu begutachten.
- Sehr verdient gemacht hat sich Alexander Gerlach als Ansprechpartner, Ratgeber und Diskussionspartner.
- Mein herzlicher Dank gilt dem XSW Team, das – in wechselnder Besetzung – bei den zahlreichen Messungen bei der ESRF und DLS dabei waren und die Durchführung dieser Experimente erst ermöglicht hat: Alexander Gerlach, Jens Niederhausen, Takuya Hosokai, Steffen Duhm, Antoni Franco Cañellas, Katharina Broch.
- Sören Claas möchte ich danken für seine unermüdlichen Einsatz im Labor, zahlreichen Diskussionen und den dadurch gewonnenen Erkenntnissen.
- Herzlichen Dank allen KorrektureleserInnen dieser Arbeit!
- Jochen Neumaier möchte ich für Diskussionen rund um die "chemischen" Fragestellungen danken.
- Allen Mitgliedern der AG Schreiber gilt mein Dank für ihre Zeit, die sie mit mir bei fachlichen und außerfachlichen Diskussionen verbracht haben.
- Ich danke allen Sekretärinnen, die mir in diversen Situationen den Rücken von Verwaltungsangelegenheiten freigehalten haben.
- Eine sehr große Hilfe im Labor waren Bernhard Degel und Bernd Hofferberth aufgrund ihrer weitreichendenden technischen Kenntnisse. Vielen Dank dafür.
- Und ich möchte ich mich bei den Mitarbeitern der Elektronikwerkstatt und der feinmechanischen Werkstatt bedanken.

Diese Liste könnte ich weiterführen, um an dieser Stelle Menschen zu danken, die jenseits der Doktorarbeit für mein Wohlbefinden gesorgt haben und mein Leben in den letzten Jahren geprägt haben. Diese Liste wäre lang, und die Gefahr, jemanden dabei zu vergessen, ist groß. Deshalb verzichte ich hier darauf, weitere Namen zu nennen. Bei all diesen Personen will ich mich mit einer Zeile aus Violetta Parras berühmtesten Lied bedanken, das sie 1966 veröffentlicht hat:

> Gracias a la vida, que me ha dado tanto.
> (Ich danke dem Leben, das mir so viel gegeben hat.)